ANALYSIS OF TOTAL SOLAR EFFICIENCY OF BIOMASS, SOLAR THERMAL, AND PHOTOVOLTAIC TECHNOLOGIES AND EVALUATION OF POTENTIAL IMPROVEMENTS VIA COMBINATION OF THE TECHNOLOGIES

by

Konstantin N. Tourkov

M.S. in Mechanical Engineering, University of Pittsburgh, 2013

B.S. in Mechanical Engineering, University of Pittsburgh, 2011

Submitted to the Graduate Faculty of

the Swanson School of Engineering in partial fulfillment

of the requirements for the degree of

Ph.D. in Mechanical Engineering

University of Pittsburgh

2016

UNIVERSITY OF PITTSBURGH

SWANSON SCHOOL OF ENGINEERING

This dissertation was presented

by

Konstantin N. Tourkov

It was defended on

March 28, 2016

and approved by

Laura A. Schaefer, Ph.D., Chair,

Department of Mechanical Engineering

Minking Chyu, Ph.D., Dean,

Department of Mechanical Engineering and Materials Science

Sung Kwon Cho, Ph.D., Associate Professor,

Department of Mechanical Engineering and Materials Science

Vikas Khanna, Ph.D., Assistant Professor,

Department of Civil and Environmental Engineering

Dissertation Director: Laura A. Schaefer, Ph.D., Chair,

Department of Mechanical Engineering

ANALYSIS OF TOTAL SOLAR EFFICIENCY OF BIOMASS, SOLAR THERMAL, AND PHOTOVOLTAIC TECHNOLOGIES AND EVALUATION OF POTENTIAL IMPROVEMENTS VIA COMBINATION OF THE TECHNOLOGIES

Konstantin N. Tourkov, PhD

University of Pittsburgh, 2016

This work examines several renewable energy resources on the basis of total solar energy efficiency and a detailed thermodynamic analysis of potential hybrid operation of several renewable energy technologies. The first part of the investigation focuses on creating a comparison between biomass, photovoltaic, and solar thermal renewable energy technologies alongside coal from the perspective of the energy pathway that originates from the energy received from the sun. This method accounts for the total energy pathway from the sun to electricity, as well as the energy investment required over the lifetime of a power plant.

The second step in the investigation is an analysis of a combination of photovoltaic technology and solar thermal technology via the use of concentrated photovoltaic cells and an organic Rankine cycle. The organic Rankine cycle is optimized by examining several configurations and working fluids with the goal of achieving highest performance for a constant temperature operating range. The behavior of the combined system is then analyzed for potential improvements.

A similar combination is then sought in the use of biomass gasification and solar thermal technology. A solar gasifier is proposed as the method of such a combination. A numerical investigation is carried out to more thoroughly examine the behavior of the solar gasifier. A CFD model is developed, utilizing a two-fluid approximation with reaction modeling for devolatilization, heterogeneous, and homogeneous chemical reactions. The results of the

composition of product synthesis gas are compared to experimental work done by other groups.

The final section of the investigation is focused on utilizing results from the aforementioned numerical investigation to examine a potential molten salt solar gasification plant that produces electricity via a solid oxide fuel combined with a microturbine. A second law analysis of the system is carried out and several configurations for the fuel cell/micro-turbine system are examined for improvements in performance under various operating pressures. An overall system exergy efficiency is established and potential improvements are identified.

TABLE OF CONTENTS

LIST OF TABLES

LIST OF FIGURES

NOMENCLATURE

W	work done
Q	heat
E	energy
h	enthalpy
s	entropy
P/p	pressure
T	temperature
x	vapor quality
y	bleed fraction
$\dot{m}$	mass flow rate
$\vec{q}$	heat flux
y	bleed ratio
ϵ	exchanger effectiveness
$\dot{V}$	volumetric flow rate
$\dot{V}_2/\dot{V}_2$	volume ratio
$\vec{v}$	velocity vector
$\vec{F}$	force vector
S	source term
Re	Reynold's number
Eo	Eotovos number
C_D	drag coefficient

C_L	lift coefficient
g	gravity
Y	mass fraction of species
$G_{k,m}$	production of turbulent kinetic energy
A_r	Arrhenius pre-exponential term
E_r	activation energy
R	universal gas constant
E_N	Nernst potential
$\Delta\bar{g}_f^o(T_{SOFC})$	Gibbs energy of formation at T_{SOFC}
F	Faraday's constant
j	current density
$\bar{y}_i$	average concentration of species i
U_f	utilization factor
V_{cell}	fuel cell voltage
$\dot{n}_i$	molar flow rate of species i
D_i, eff	diffusion coefficient
LHV	lower heating value
C_p	heat capacity coefficient

Greek

η	efficiency or polarization
$\Phi/\dot{\Phi}$	total exergy/total exergy flow rate $[J/s]$
ϕ	specific exergy $[J/kg]$ or $[J/mol]$
γ	pre-exponential factor
α	volume fraction
ρ	density
σ	surface tension
μ	dynamic viscosity

β_r	Arrhenius temperature exponent
δ	thickness
ϵ	exchanger effectiveness

Subscripts

ex	exergetic
out	out of control volume
in	into control volume
th	thermal
act	activation
e	electron
an	anode
cat	cathode
el	electrolyte
int	interconnect

Abbreviations

PV	photovoltaic
LCA	life cycle assessment
PTC	parabolic trough collector
DSG	direct steam generator
ORC	Organic Rankine cycle
CFD	computational fluid dynamics
LCEC	life cycle energy cost
LCEA	life cycle energy analysis/assessment
EROI	energy returned on investment
EPT/EPBT	energy payback time

CED	cumulative energy demand
NER	net energy ratio
CHP	combined heat and power
CPV	concentrated photovoltaics
ODP	ozone depletion potential
GWP	global warming potential
RNG	renormalization group theory
SOFC	solid oxide fuel cell
LSM	lanthanum strontium manganite
MGT	micro gas turbine
Si	silicon
GaAs	gallium arsenide
InP	indium phosphide
CdS	cadmium sulfide
InGaP	indium gallium phosphide
InGaAs	indium gallium arsenide
Ge	germanium
CdTe	cadmium telluride
IHE	internal heat exchanger
OFOH	open feed organic fluid heater
CFOH	closed feed organic fluid heater

Names

EPRI	Electric Power Research Institute
NREL	National Renewable Energy Laboratory
40 CFR 82	Code of Federal Regulations Title 40- Protection of Environment, Part 82
FAR IPCC	Fourth Assessment Report of the Intergovernmental Panel on Climate Change

WMO	World Meteorological Organization
SROC	IPCC Special Report on Safeguarding the Ozone Layer and the Global Climate System: Issues related to Hydrofluorocarbons and Perfluorocarbons
TAR	Third Assessment Report of the Intergovernmental Panel on Climate Change

1.0 INTRODUCTION

The demand for energy across the planet is increasing, and while our current supply can match this demand, predictions say the price of energy will continue to go up as it becomes harder to find fossil fuels. When this is taken into consideration with the proven research on climate change, there is clear indication of a need for increased use of renewable energy resources. The EIA estimates about 21% of the world electricity generation was from renewable energy in 2011, which is projected to increase to 25% in 2040 [1, 2]. The largest source of renewable energy is currently hydro power plants [1]. However, there is very little potential for expanding on this source as most potential sites for dams have been already been constructed. Thus, there is a need to investigate other renewable energy resources to expand our use of the abundant renewable energy available to us. The work proposed here aims to increase our understanding of the potential of the renewable energy resources available to us, and investigate more effective ways to use this by combining technologies that are typically used separately.

1.1 PHOTOVOLTAICS (PV)

One renewable energy technology that has been receiving a lot of attention is photovoltaic electricity generation. This technology functions on the concept of semiconduction. Photons from solar energy impact one layer, exciting electrons and causing them to migrate over a junction to the other layer. This creates an electric charge. Currently, a large variety of materials exist that can be turned into light sensitive semi-conductors, the most famous being silicon. While a common material, it has several drawbacks such as degradation above

room temperature. There are other materials, however, that perform well under harsher conditions. It has additionally been proven that combining several materials together to form two or more junctions can improve efficiency by making better use of the incoming spectrum.

Photovoltaic cells have some drawbacks. They are limited in efficiency due to how they capture solar energy. It has been proven that perfect conversion cannot occur [3]. Additionally, the process of making these cells is expensive and requires a significant amount of energy. The energy input aspect is further discussed in this work.

1.2 SOLAR THERMAL

Solar energy impacts the Earth at a black body temperature of $5778K$ [4]. In some places, solar radiation during the day can exceed $1000W/m^2$, with averages for those areas reaching $9kWh/m^2/day$ [5]. Concentration techniques, as discussed below, are typically used to capture this thermal energy at a high temperature to operate various thermal cycles.

1.2.1 Parabolic Trough

As the name describes, this design features a long trough that focuses light using mirrors onto a tube that absorbs the energy and transmits it to a circulating fluid, typically a thermal oil. In the standard design, the fluid evaporates steam via a heat exchanger, which drives a steam turbine. Several alternate configurations of this design have been proposed and studied, one utilizing molten salt as the circulating fluid, and another evaporating the water directly within the absorbing line.

1.2.2 Solar Tower

Similar in concept to the parabolic trough, the solar tower configuration is also based on focusing solar energy using mirrors. In this configuration, a field of mirrors reflects solar energy onto a single focal point. Due to the focal surface area being much smaller, higher

temperatures can be reached and several configurations have been proposed and implemented to efficiently use this high temperature energy.

1.2.3 Fresnel Lens

This technology can be closely compared to the parabolic trough concept. A row of prisms is used to reflect light onto a line of focus, the location of which is occupied by a tube circulating thermal fluid.

1.2.4 Drawbacks of solar thermal power

While there is great potential for solar thermal energy, there are technological hurdles that must be overcome that are currently preventing it from becoming commercialized. One of these is the inconsistency of solar energy due to daily variation and cloud cover. Thermal storage and backup gas turbines have been used to mitigate the problem, but have a high cost, either upfront or during operation. A second drawback is low solar efficiency, due to relatively low operating temperatures. While solar towers can achieve higher temperatures, there are larger thermal losses at the focal point.

1.3 BIOMASS

Biomass energy is often associated with providing fuels for the transportation sector. There is, however, a significant potential for its use in electricity production. This can be in simple methods, such as direct combustion in a boiler of a biomass power plant, co-firing with coal in a traditional coal plant, or via gasification into H_2 and CO for high temperature combustion in a Brayton cycle gas turbine.

One of the goals of renewable enegy research is to implement it into the market at a larger share. With this goal in mind, direct combustion and co-firing of biomass have a lot of potential, as they mostly depend on existing infrastructure, mainly coal power plants. The process of gasification is more complex than simple combustion and involves technology that

is less established than traditional coal combustion. There is currently much work being done on improving gasification efficiency and utilizing the product gases more effectively. One aspect of this is the requirement of external heat in the gasification process, typically achieved by allowing oxygen into the reactor to allow an exothermal reaction to produce the required energy.

1.4 MOTIVATION

As has been stated above, the major source of renewable energy is currently hydro power acquired from dams, arguably a somewhat controversial technology itself. While there is significant work that has been done on many renewable energy resources, particularly the ones mentioned above, none of them have a significant share in the market. This signifies that there is need for further research in improving these technologies to achieve a level competitive with currently dominating energy sources. One aspect of this is identifying the potential that each technology has using a metric that equally compares them. Additionally, since each technology has drawbacks, there is a need to explore novel ideas that may bypass these drawbacks or alleviate them. The goals of this work, described below, address some of these needs and attempt to provide a framework for improving existing technologies that may prove capable of competing in the global market.

1.5 GOALS OF THIS WORK

The technologies discussed above each have potential in increasing the overall share of renewable energy used globally. As stated, each has challenges to overcome, before it can become more widespread. While significant research has been carried out on improving the energy efficiency of each technology and the environmental impacts over the life cycle of each technology, there is a need to measure the maximum potential of each energy from a perspective of solar efficiency. Since all energy on Earth began as solar energy, with the exception of nu-

clear and geothermal, it is important to evaluate how efficiently we are utilizing this energy. The first portion of this work will examine the total solar efficiency over a plant life cycle for photovoltaic, solar thermal, biomass, and coal power production technologies. Since each technology has its individual limitations, some have proposed novel combinations that may together more efficiently produce energy. One such combination is the use of photovoltaic cells along with a bottoming organic Rankine cycle that utilizes waste heat. This work will examine the potential of this combination by testing various working fluids and cycle configurations, and evaluating how they behave in relation to varying types of photovoltaic cells. A second combination that has been proposed is utilizing solar energy to provide external energy to drive gasification of biomass. This work will examine a CFD model, based on findings of biomass gasification in molten salt, a potential medium for gasification that can be combined with solar thermal energy capture and storage. The model will evaluate several reaction mechanism models to identify which matches experimental results of other groups. The final portion of this work will examine the resulting parameters of the CFD model when used in a solar thermal gasification solid oxide fuel cell (SOFC) power plant, a configuration with the potential for operating at very high overall efficiencies.

2.0 QUANTIFYING TOTAL SOLAR EFFICIENCIES OF COAL, BIOMASS, SOLAR THERMAL, AND PHOTOVOLTAIC POWER GENERATION TECHNOLOGIES

Before we can quantify the effects of combining a variety of renewable energy methods, we must first define how we evaluate the individual technologies. This chapter will discuss the current state of our knowledge and research challenges in PV, solar thermal, and biomass conversion; the thermodynamics of the overall power plants in which these systems may be implemented (as well as in existing fossil fuel-based plants); and energy and environmental metrics that are used in the power generation community and beyond.

2.1 OVERVIEW OF EXISTING TECHNOLOGIES

2.1.1 Photovoltaics

Several materials can be doped to create a current when encountering sunlight. Early PV cells were much less efficient than the ones being designed today. Efficiency is of great importance in the research of PV materials. Several labs across the world have been working on creating the highest efficiency cells. A comprehensive list of these has been compiled by NREL, summarizing the best research cell efficiencies achieved [6]. Simultaneously, there is a sustainability-related focus associated with this technology in the form of life cycle assessment (LCA), tailored to evaluate the energy and materials requirements of these various cells. Several groups have evaluated these demands, often presenting them in form of cost, energy pay-back time, and CO_2 emission rate [7–9].

2.1.1.1 Multi-junction high temperature cells

There has recently been increased attention on multi-junction cells. Several types of these cells dominate with the highest efficiencies. This is due to the property of the multiple materials used together to individually absorb varying spectrums of light. This combination allows for a combined curve that spans across a much larger portion of the incoming spectrum. An additional benefit of these cells is their behavior under concentration. Studied by groups such as Nishioka et al., these cells have shown higher efficiencies at room temperatures under concentration, as well as the ability to maintain high efficiency at increasing temperatures [10]. It is this behavior, proven by several groups [10–12], that has led some groups to investigate the potential use of concentrated photovoltaics (CPV) with thermal applications, discussed in further detail later in this work [13–17].

2.1.2 Solar Thermal

As discussed above, there are several configurations for utilizing solar thermal technology. The two that are discussed in this work are more common and have established prototype and commercial plants [18]. However, while mature, the technology has room for improvement. All solar technologies are subject to changing levels of input solar energy, and while some are inherently more capable of handling the variations, there is a great deal of effort going towards finding efficient and cost effective ways of managing the changing inputs. Optics, thermodynamics, and heat transfer are also major areas of research, since energy focus and transfer are key aspects in solar thermal technology.

2.1.2.1 Parabolic trough plants

There are several areas of focus for research on parabolic trough power generation. The first deals with improving performance, reliability, and cost effectiveness of the solar field, which includes the collectors, receivers, and the transfer fluid that absorbs the incoming solar energy. Several groups have investigated improving the concentrator structure in an effort to improve reliability and reduce material costs [19–21]. Mirrors have additionally received attention, as their performance directly affects the amount of sunlight that reaches the receiver [22, 23]. Cost is a large factor due to

the large mirror area required for larger power plant projects. Efficient and reliable receivers are equally important in parabolic trough concentrating (PTC) plants. A popular design that minimizes heat loss is a system of two long tubes, one that absorbs the sunlight and transfers it to the circulating fluid, and the other a glass tube with low reflectance that forms a vacuum seal between the inner tube and the ambient air [24, 25].

To cope with the variation of the incoming solar energy, thermal energy storage is typically used in solar thermal plants. Several designs have been studied and optimized for the parabolic trough configuration. A two-tank configuration that directly stores the heat transfer fluid is a popular choice and both have been used for older systems and can be used in molten salt operating systems [26]. A similar system that stores the heat indirectly by using a secondary storage fluid has also been studied [26].

An innovative and cost efficient alternative to the two systems is a single-tank thermocline that operates on a thermal gradient with hot fluid on the top and cold fluid on the bottom [27]. Solid thermal storage is an alternative to using tanks to store liquid. High temperature concrete is one possible medium that several groups are investigating [28]. This has the advantage of being very low cost. Phase-change materials can also be utilized to create a half solid, half liquid storage medium that can store a large amount of energy in relatively small volumes [29].

A highly efficient solar field that transfers energy to an inefficient power block will result in poor overall performance. Thus, a great deal of attention has been paid to optimizing the electricity generating systems that operate with the solar fields. Traditional steam Rankine cycles have been used in combination with solar fields and have produced good results [30]. However, unlike coal power plants, PTC plants operate at lower temperatures and thus suffer from some loss in efficiency.

Organic Rankine cycles (ORCs) have been examined as alternative that presents some simplifications and possible improvements, since, as discussed further in the next chapter, they perform better than steam based cycles as operating temperatures decrease [31, 32]. To compensate for the lower operating temperatures of PTC fields, a gas turbine can be combined with the solar power plant to produce energy and exhaust gas that can superheat steam to a temperature higher than what the solar field can achieve [33]. Direct steam

generation (DSG) is a further alternative to the existing systems where steam is directly generated in the solar field [34]. Temperature control is a challenge for these systems that some creative designs have been proposed to tackle [35, 36].

2.1.2.2 Solar Towers Solar towers inherently have an advantage over PTC plants in achieving higher concentration ratios. However, there are some challenges, similar to those for PTC designs, that solar towers must overcome. The heliostat mirror field is one of the areas that has been studied. The heliostat mirrors can be flat or curved, but must be steered on two-axes to track the sun and at certain solar angles can cause shading, reducing efficiency. The height of the receiver tower must be carefully considered as well, since larger fields focused on one spot will experience more shading with a lower tower [37, 38].

The design of the receiver greatly affects the overall performance of the solar tower plant. There are several types of receivers that can be used in solar towers. Volumetric receivers are constructed using porous wires that promote heat exchange to the heat transfer fluid [39]. Heat transfer and temperature distribution have been the focus of studies with these types of receivers. Cavity receivers are simpler in design, where sunlight enters through a window and is absorbed by the walls of the cavity [40]. Effective heat transfer and highly absorbent materials are important in the design of these receivers. A lesser known type of receiver, called a particle receiver, utilizes solid particles that directly absorb the incident solar energy and transfer it to a working fluid in a fluidized bed-type heat exchanger [41].

The power block in solar tower plants can vary drastically in design. A hybrid system where a Brayton cycle gas turbine is combined with a solar field has been examined with promising results for efficiency [42]. An improvement on this system is the idea of combining the solar tower as the air preheater for a Brayton cycle that uses exhaust heat to power a steam generator [43]. A more fossil-fuel independent design that uses a Rankine cycle has also been examined [44]. In this design, hot air from the central tower evaporates and heats high pressure steam. This design operates at similar temperatures to traditional coal power cycles.

2.1.3 Biomass

The oxidation reaction, shown below for cellulose, is a simple exothermal reaction that produces carbon dioxide and water. Several studies examined plant designs and the life cycle performance of biomass combustion [45, 46].

$$C_6H_{10}O_{5,s} + 6O_2 \rightarrow 6CO_{2,g} + 5H_2O_g \tag{2.1}$$

While combustion is an exothermic reaction that requires oxygen, gasification is endothermic where the biomass reacts with either steam or carbon dioxide, and thus requires a heat source. Autothermal gasifiers acquire this energy from partially combusting/oxidizing the incoming biomass by allowing some oxygen into the reactor. Allothermal reactors combust a portion of the exiting gases in a separate reactor, and transfer the thermal energy to the gasifier [47]. Finally, if an external heat source exists, the entirety of the gasifier products are used in the downstream components.

The process itself consists of two reactions, the first being a pyrolysis reaction to break the cellulose into carbon and gases, as shown:

$$C_6H_{10}O_{5,s} \rightarrow C_s + 5(H_{2,g} + CO_g) \tag{2.2}$$

This reaction occurs relatively quickly and produces a portion of the desired product gases. The second reaction is the gasification reaction where the carbon reacts with steam or carbon dioxide (equation below shown for steam), to create hydrogen and carbon monoxide:

$$C_s + H_2O_g \rightarrow H_{2,g} + CO_g \tag{2.3}$$

As further discussed below, some of the advantages of gasification are the high energy value of the product gases and their utility, as they undergo further reaction to create useful chemicals or fuels [48]. The product gases themselves can be combusted at a high temperature in a Brayton cycle to achieve higher efficiency than a typical steam cycle, or even reacted in a fuel cell to directly generate electricity [48].

There are several ways to introduce the biomass and the reacting gases into a reaction chamber, leading to different types of gasifiers. Fixed bed gasifiers can be broken down into

either updraft, where the biomass enters through the top while the input gases enter through the bottom, or downdraft, where the biomass and the input gases enter from the top [48]. In a fluidized bed gasifier, both the biomass and the input gases enter through the bottom, where the input gases fluidize the solid particles within the reactor, enhancing heat transfer [48]. Each type of gasifier has advantages and disadvantages to their performance. A novel type of gasifier has been proposed by Hathaway et al. that utilizes a molten salt medium within which the biomass and the gases are mixed [49, 50]. This is discussed in further detail later in the proposal.

The use of biomass for electricity production is only one branch of a larger body of research. Additionally, the branches are non-exclusive, as gasification and Fischer-Tropsch research are closely related, as products of the first directly influence the second [48]. Thus, the focus of the below review has been limited to the progress in the use of biomass in producing electricity via direct-firing, co-firing, and gasification.

2.1.3.1 Direct-firing and co-firing One advantage of biomass is its adaptability to current technologies. This can be best seen in the use of biomass and coal co-firing. Several studies have examined the effect various ratios of biomass to coal have on output of energy and emissions [45, 46]. This has additionally been expanded to life cycle studies over plant lifetime. Direct firing of biomass does not require any novel technologies and thus is an attractive alternative, as well [45]. However, as discussed below, the conventional process of combustion is not as energy efficient as other alternatives, mainly gasification.

2.1.3.2 Gasification The process of gasification is complex and has been studied analytically, numerically, and experimentally in great detail. The process itself consists of two reactions: a relatively quick pyrolysis of cellulose into pure carbon and several gases and a slower gasification reaction where pure carbon mixes either with CO_2 or steam to create CO and H_2 gases. The complexity of the pyrolysis and gasification reactions presents itself even in analytical investigations. It has been found that several factors influence the theoretical efficiencies achievable by gasification reactors. Moisture content has been shown to be one of the most significant aspects [51]. Computational modeling of pyrolysis and gasification is

very demanding due to the inherent nature of the processes: typically two or three states interacting physically, chemically, and thermally, with reactions absorbing heat, or in the case of autothermal gasification, both absorbing and producing heat. Several studies have been focused on one or two aspects of this behavior to simplify the problem [52–55]. The CFD models used are discussed in further detail in Chapter 4. In addition to CFD modeling, a significant amount of experimental work has been carried out on various types of gasifiers, the biomass being used, and factors influencing performance [55–57].

2.2 THERMODYNAMICS IN POWER PLANTS

All of the above technologies can be used in the context of a larger power plant. This section discusses how such plants should be evaluated.

2.2.1 First Law of Thermodynamics and Efficiency

The concept of energy conservation is vital to the analysis of power systems. In this framework, an analysis of efficiency can be carried out by analyzing the ratio of work produced to the heat added, as shown in the well-known equation below:

$$\eta_{PowerCycle} = \frac{W_{out}}{Q_{in}} \tag{2.4}$$

where W_{out} is the output work and Q_{in} is the input heat. While many thermodynamic cycles can be used to produce electrical work from an input of heat, the most widely used today are the Rankine cycle based on steam, and the Brayton cycle based on air. A combination can sometimes be used where a Rankine cycle is powered by exhaust air from a Brayton cycle.

2.2.2 Exergy

The concept of exergy is based on the ability of a certain amount of energy in one form to transform into another. Often used to quantify losses in thermal power plants, exergy is based on the Carnot efficiency and the concept of a dead state (the temperature of the

surrounding environment). When evaluating the potential of heat at a certain temperature to do work, the following equation is used:

$$\Phi = Q(1 - \frac{T_o}{T_{source}}) \tag{2.5}$$

where Φ is the maximum possible energy that the source Q can provide, if the source is at T_{source} and the surrounding environment is at T_o, both measured in absolute temperature. From this, the exergetic efficiency can be defined as follows:

$$\eta_{ex} = \frac{W_{out}}{\Phi_{in} - \Phi_{out}} \tag{2.6}$$

This concept can be extended to stored chemical energy, such as combustible fuels, or a difference in concentration, such as that between seawater and fresh water (osmotic power). In power plant cycles, such as the Rankine and Brayton cycles discussed above, an exergy analysis can be carried out to identify losses in energy quality. In this study, these concepts are used to measure the exergetic efficiency of converting solar energy through various paths to produce electricity.

2.3 LIFE CYCLE ENERGY ANALYSIS

It is also important to quantify the environmental impacts of energy producing technologies, including the production of the materials necessary to build an electric plant, the generation of emissions during the plant's lifetime, and the resources consumed during the plant's decommissioning and disposal. This is typically known as life cycle assessment (LCA). This study implements the ratio of energy required to the energy produced, also known as life cycle energy cost (LCEC), in the analysis of the total efficiency of a technology. Analyses that focus on the life cycle energy consumption of systems are typically known as life cycle energy analyses (LCEA).

Since several technologies are evaluated in this work, a variety of measures are used to describe the LCEC, such as the energy returned on investment (EROI), energy payback time (EPT/EPBT), cumulative energy demand (CED), and net energy ratio (NER). All of these

metrics ultimately can be converted into LCEC values, as described below. EROI is the inverse of LCEC, and provides a factor of how many times a plant will pay for itself in terms of energy:

$$EROI = \frac{1}{LCEC} \tag{2.7}$$

Energy payback time, as the name suggests, is a measure of how long a plant needs to operate before its net energy consumption is zero, meaning the plant has produced as much energy as was put into it over the lifetime. This measure can used along with the lifetime of a plant to produce the LCEC, as shown:

$$LCEC = \frac{EPT \times E_{output}}{Lifetime \times E_{output}} = \frac{E_{input,total}}{E_{output,total}} = \frac{EPT}{Lifetime} \tag{2.8}$$

where E_{input} and E_{output} are the energy consumed and produced, and are in units of energy/time.

The total energy a system requires to operate, which in the case of an electricity producing plant is the energy for construction, use, and deconstruction/disposal, is typically referred to as the cumulative energy demand (CED). This value can be related to the LCEC by the total energy production, as follows:

$$LCEC = \frac{CED}{E_{output,total}} \tag{2.9}$$

When evaluating biomass systems, the electric energy produced can be compared to the fossil fuel energy consumed, resulting in the net energy ratio (NER). When the NER takes into account plant energy demand for construction, use, and teardown, the NER is equivalent to the EROI and can be similarly related to the LCEC.

2.4 LIFE CYCLE ANALYSIS OF SOLAR ENERGY

Many approaches to energy and exergy assessment focus on the power plant itself, considering the incoming fuel as the initial source of the energy. As an example, incoming solar energy to a photovoltaic cell is considered the first step, similar to light from the sun coming into contact with a reflector in a solar thermal plant. The application of this frame of analysis can then be somewhat skewed when considering something like biomass energy, since the first step is technically sunlight hitting the crop that is being grown, but most analyses begin the biomass already harvested and entering the power plant. Additionally, most energy or exergy efficiency studies do not consider a life cycle assessment of the energy and material requirements over the plant lifetime. Life cycle assessment can be a useful tool in comparing technologies that can be vastly different. An example of this ability is the work by NREL to assess the CO_2 emissions of various types of renewable and non-renewable energy [58]. A complete view of the energy pathway, then, is a crucial goal in understanding how energy is delivered to the grid. Hu et al. investigated this by considering the conversion path of solar energy towards becoming coal, being mined, converted to electricity, and subsequently used to drive a traditional vapor-compression air conditioning unit [59]. They, then, compared this to the path of solar energy being used to drive an absorption cycle, where the thermal demand is met with the solar energy. Based on their findings, the solar efficiency of a solar thermal absorption unit of was several orders of magnitude higher than that of the coal power plant pathway.

2.5 EVALUATING TOTAL SOLAR LIFE CYCLE EFFICIENCY BY CONSIDERING PLANT PERFORMANCE AND LIFE CYCLE ENERGY DEMAND

The technologies discussed above are drastically different in how they convert energy into electricity. The most important factor to consider in this process is that all energy that is being converted initially began as solar energy, and either underwent a natural conversion

process, or was converted using some direct or indirect human input. This work expands on this concept by evaluating photovoltaic, solar thermal, biomass, and coal power production technologies over the total process that initial solar energy undergoes to be transformed to electricity. Additionally, to truly measure the efficiency that a technology achieves, the energy demand over the life cycle of the plant is considered in each case, and combined with the solar efficiency. Such an examination provides a full view of exactly how efficiently each technology, as it currently exists, uses solar energy.

2.6 ENERGY FLOW ANALYSIS FOR ELECTRICITY PRODUCTION

When analyzing several significantly varying technologies, it is important to obtain generalizable metrics that apply to all of the technologies being investigated. Thus, the technologies being examined in this study will be evaluated based on their energetic and exergetic efficiencies. The energy conversion process will be assessed from the initial energy input from solar insolation to the conversion of the energy to electricity. It is important to note that all technologies evaluated in this work use solar energy as the initial energy source.

2.6.1 Coal

Coal can be thought of as stored solar energy in chemical bonds [60], and as such, can be analyzed alongside other solar energy resources. There are several steps in the process, shown in Figure 2.1. In this framework, the energy cycle for coal begins with solar energy being converted to chemical energy via photosynthesis with an efficiency of 3.5% [61]. There have been numerous studies on the conversion efficiency of sunlight to biomass energy via photosynthesis. These have been measured experimentally [62–65], as well as predicted theoretically [3, 61]. Actual efficiency values vary between 0.2% and 4.3% [61, 64], while the theoretical maximum has been calculated to be 4.6% for C3 plants (plants that undergo photosynthesis using the Calvin cycle) and 6.0% for C4 plants (plants that undergo photosynthesis using Hatch and Slack cycle), [3, 61]. The value above that is used in this study is

based on experimental results for C3 plants, a more common source of biomass. An exergy study of photosynthesis by Petela produced an overall exergy efficiency of 2.74%, a value similar to the energy efficiencies above [66]. The ancient biomass then dies and is stored in

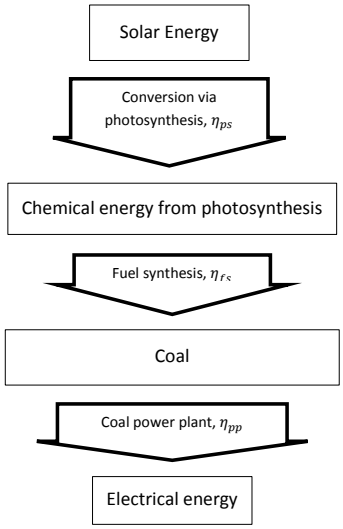

Figure 2.1: Coal Energy Flow

the ground, while undergoing a slow process of conversion to coal. Hu et al. evaluated several sources to derive the efficiency of this process, and arrived at a value of 8% (for both the energy and exergy efficiency) that combines the process of fuel synthesis and mining [59, 60]. The coal is then burned in a power plant with an energy efficiency of 34.6% [67]. There have been several studies concerning the comparison of the energy and exergy efficiency of coal thermal power plants. Rosen found the overall energy and exergy efficiencies of a coal plant were 37% and 36%, respectively [68]. Several other studies have shown similar values for the two measures [69–71]. The overall cycle efficiency is the combination of all steps in the process of conversion, achieving a conversion energy efficiency of 0.107% and exergy efficiency of 0.088%.

2.6.2 Biomass

The total efficiency of converting solar energy to electrical energy via biomass is calculated by considering the efficiency of photosynthesis along with the efficiency of converting stored biomass energy to electrical energy. This process is similar to the one above, but is simplified, due to the absence of the coal conversion step. Since there are several paths for converting biomass energy to electrical energy, two were considered below, as shown in Figure 2.2. The two most popular technologies for using biomass for electric generation are direct-firing and bio-gas conversion. While the process for direct-firing is simpler and can be implemented along with coal combustion (co-firing), it is significantly less efficient compared to bio-gas. [45, 72].

The boiler plays a key role in the direct-firing process, converting chemical energy to thermal energy. A study done by EPRI identifies a thermal efficiency of 0.717 for a boiler without an upstream dryer and an efficiency of 0.845 for a boiler with an upstream dryer [45]. The total energy efficiency of direct-firing has been estimated by EPRI to be 27.7% [45]. Using these figures, the total conversion efficiency of solar energy to electrical energy can be estimated at 0.97% for the energy efficiency and 0.898% for the exergy efficiency. This figure does not take into consideration life cycle energy investments, which are discussed below.

Higher efficiencies can be expected if the chemical energy in biomass is extracted at higher temperatures. With this goal, gasification is used to convert energy stored into a combustible gas that can used in a Brayton cycle with a bottoming Rankine cycle [45, 73, 74]. The process of gasification drives the design of power plants to be far different from the direct-fired counterpart. Studies have estimated gasification energy efficiencies of $74-84\%$ and exergy efficiencies of $68-83\%$, depending on the fuel [51, 75, 76]. There are several estimates for the efficiency of gasification power plants. These vary between 27% and 37.2%.

Additional evaluations of both energy and exergy efficiencies of biomass gasification have shown similar values (35.1%-46.8% for energy and 43.2%-45.9% for exergy [73]). It is important to note that the process of gasification allows for capture of CO_2, which affects the overall performance of the plant from both a life cycle and an energy perspective. The energy impact of CO_2 capture was studied by Minguez et al., showing that for various

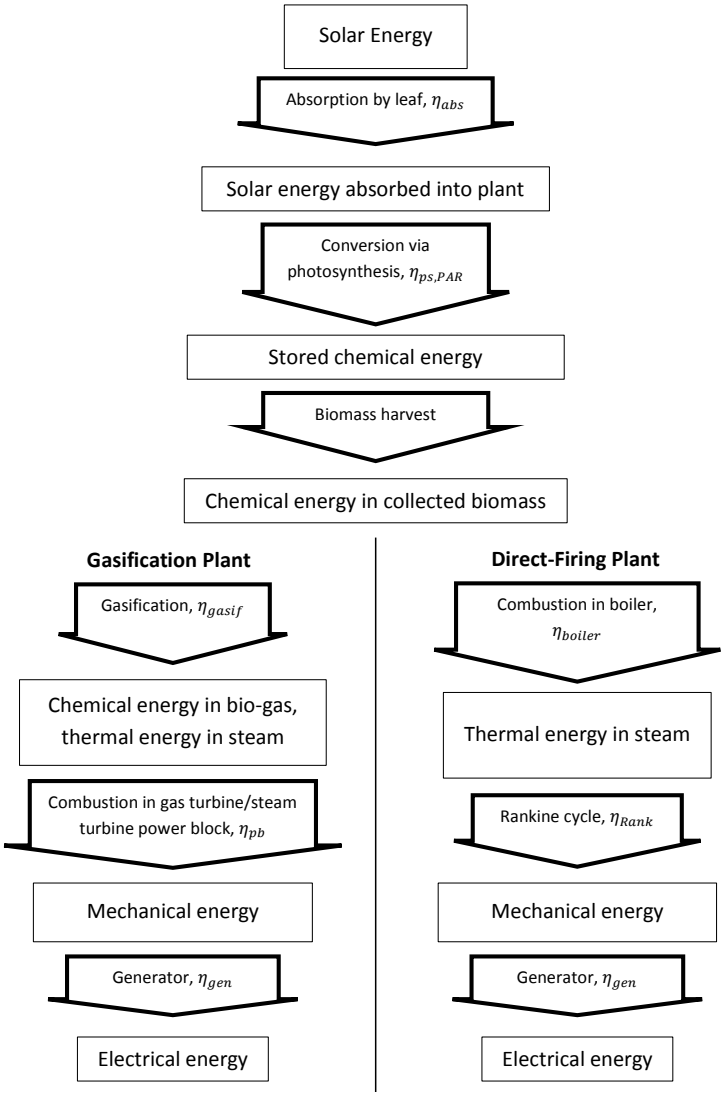

Figure 2.2: Biomass Energy Flow

sources of biomass, capturing pre-combustion CO_2 has a noticeably negative effect on total energy efficiency [73]. The overall efficiency of the conversion of solar energy to electricity via biomass using the the bio-gas process can be calculated using the data for the photosynthesis efficiency and the data above in a similar manner to direct-fired technology. The energy and exergy efficiencies of the overall process therefore range between 0.95% and 1.30%.

2.6.3 Solar Thermal

The conversion of solar energy via the solar thermal pathway is significantly simpler, compared to the above technologies. A fundamentally two-step process, the solar energy is captured as heat, and then converted into mechanical energy. There are several technologies that are currently being researched in the field of solar thermal power production. The two oldest and most well-developed of these are the parabolic trough collector and central receiver/heliostat field plants, as shown in Figure 2.3. Fresnel lens technology has also been receiving attention, and will additionally be considered in this study.

There has been significant research done on parabolic trough collector and receiver technology to improve the efficiency of conversion from solar energy into thermal energy. Several of these evaluated the performance based on both energy and exergy [77, 78]. Reddy et al. performed such an evaluation with overall performance of 24% for the energy and 25.8% for the exergy [79]. Their group found that the largest source of exergy loss is in the collector-receiver assembly. It should be noted that the unusual behavior of exergy efficiency values exceeding energy efficiency values is a result of the state of the input solar energy. The energy is received at a prescribed temperature with a lower exergetic than energetic value, while the electricity output energy value matches the exergy value, resulting in higher exergy than energy efficiency. Studies aimed at energy efficiency and LCA evaluations have evaluated proposed and active plants with efficiencies varying between 9.0% and 16.7% [67, 80–82].

The energy conversion process in solar tower plants begins with reflection of sunlight onto a single focal point via mirrors in a heliostat field. The overall efficiency can be expected to be somewhat higher for these plants, compared to PTC plants, due to higher operating temperatures at the focal point [83]. An evaluation of the energy and exergy performance by

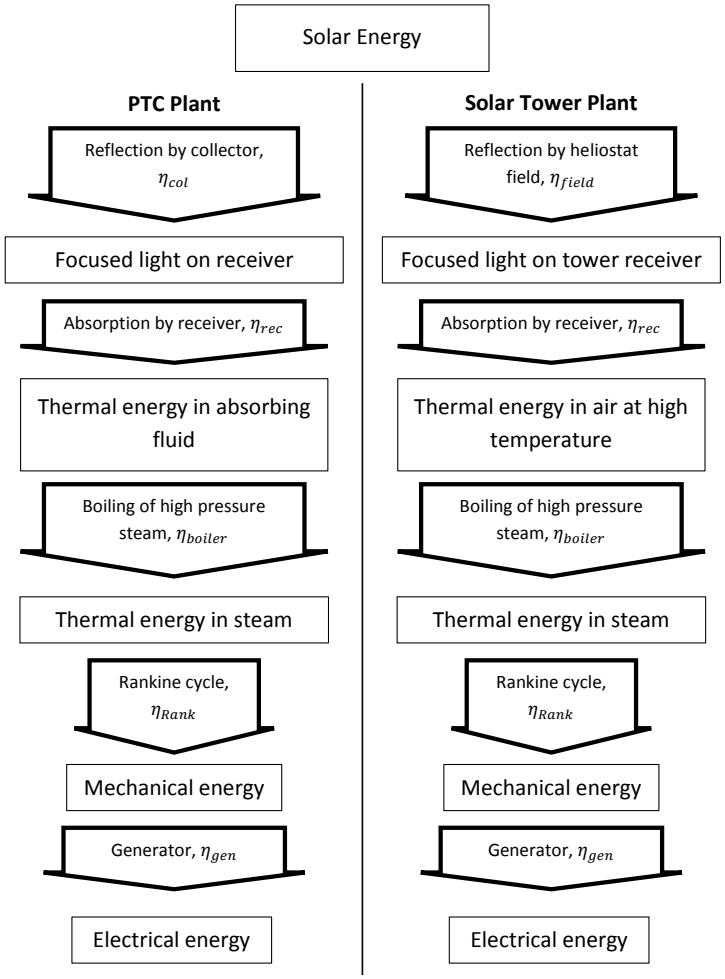

Figure 2.3: Solar Thermal Energy Flow

Reddy et al. produced values of 27% and 29.2%, respectively [84]. Their group found that the solar tower behaves somewhat similar to a PTC plant in that the main exergetic losses are in the collector-receiver system. Studies that evaluated central tower plants on the basis of efficiency and LCA demonstrate efficiencies of 14.6% and 16.7%.

2.6.4 Photovoltaic Cells

Photovoltaic cells convert incoming solar energy directly to an electric charge, as shown in Figure 2.4. There are various types of solar cells that are currently on the market. Several types of cells were investigated in this study to obtain a measure of the variability in photovoltaic electricity generation: multi-crystalline Silicon, amorphous Silicon, ribbon Silicon, copper indium gallium selenide (CIS), cadmium telluride (CdTe), indium gallium phosphide (InGaP), and gallium arsenide (GaAs), as well as some combinations. The energy efficiency of these cells varies from 4.95% to 28.5% [7–9, 67, 85]. The direct conversion of solar energy to electrical energy implies an exergetically perfect process, meaning that the exergetic efficiency of a solar cell equals the energy efficiency.

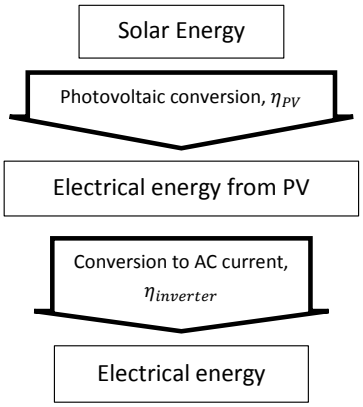

Figure 2.4: PV Energy Flow

2.7 LIFE CYCLE ENERGY ASSESSMENT AND EROI

Energy and exergy efficiency assessments are useful in identifying the performance of an electricity producing technology. However, these measurements of performance are not the only way to compare such technologies. It is important to consider the energy input over the lifetime. The assessment below discusses this criterion for each technology considered in the study. The various metrics used to evaluate each technology can then be converted to the LCEC. The values provided by the sources below are shown in Figure 2.5 for the EROI and Figure 2.6 for the LCEC.

2.7.1 Coal

In their examination of the EROI of several renewable and non-renewable energy resources, Weissbach et al. included an analysis of hard and brown coal [67, 86]. They found that the majority of the energy input consists of the coal extraction process, with energy ratio (EROI) values of 29 for hard coal and 31 for brown coal. Of the energy demand for the underground mined hard coal, approximately 8% was required for plant construction, less than 1% for decomissioning, 31% for maintenance and operation, and 60% for coal extraction. The energy input for open pit mined brown coal consisted of approximately 11% for plant construction, less than 1% for decommissioning, 17% for maintenance and operation, and 71% for coal extraction. The overall values, however, were found to be significantly lower than any renewable energy resource. Other groups have examined the EROI of coal with a larger range of results. Raugei et al. compared the EROI of several PV materials to an estimate of the lower and upper values estimated values for coal at 12.2 and 24.6 [87]. Another group evaluated the variation of EROI in China for coal power plants and have found that it has decreased from 35 to 27 [88].

2.7.2 Biomass

An approach to life cycle analysis of biomass power using efficiency can be useful in considering the inputs and outputs of the system. Since there can be significant energy requirements

for the production of biomass (land preparation, maintenance, fuel, etc.), one group proposed a way to examine system efficiency by accounting for these upstream inputs [89]:

$$\eta_{LifeCycle} = \frac{E_{grid} - E_{consumed}}{E_{biomass}} \tag{2.10}$$

where E_{grid} is the electric energy produced by the plant, $E_{consumed}$ is the energy consumed in upstream processes, and $E_{biomass}$ is the energy in the biomass fed to the power plant. Rafaschieri et al. performed such an analysis on a poplar-based gasification plant [89]. Similarly, Mann and Spath conducted an extensive study examining biomass gasification via a life cycle assessment [90]. The largest contributor to energy consumption of the inputs was found to be the feedstock production step of the process, consuming 0.77 of the total energy consumption. Heller et al. examined the use of willow as a source of biomass via an LCA [91]. Their group identified two values for gasification: 0.372, provided by NREL [90]; and 0.36, provided by EPRI [45]. Additionally, they identified a value of 0.277, provided by EPRI [45], for direct-fired conversion.

Several other studies have been conducted in addition to the ones discussed above [92–95]. The resulting values for the energy ratio found in these studies, along with the conversion efficiencies of the plants, can provide a total solar life cycle efficiency, when accounting for the photosynthesis efficiency results discussed above.

2.7.3 Solar Thermal

There has been significant LCA research on various solar thermal power stations, both in operation and proposed for construction. A life cycle analysis performed by Lechon et al. focused on solar thermal power plants in Spain, examining parabolic trough and solar tower configurations [81]. Both configurations operated in hybrid mode with natural gas. An examination of the cumulative energy demand over the life cycle showed that the majority of the demand consists of the operation stage due to the natural gas and electricity consumption. Zhang et al. examined the embodied energy of a 1.5MW Chinese Dahan solar tower plant [96]. The plant was found to have an energy output/input ratio of 6.85. Viebahn examined three solar thermal technologies using LCA: a parabolic trough operating using thermal

oil, a Fresnel collector, and direct steam generation [82]. The National Energy Technology Laboratory (NETL) also performed an LCA and cost analysis to evaluate the potential of solar thermal power in the U.S. [80]. The analysis provided an EROI of 8.2 and showed that a large portion of the greenhouse gas emissions over the lifetime of the plant come from the fuel combustion during the operation phase.

2.7.4 Photovoltaic Cells

The energy requirement over the lifetime of a technology is an important indicator of the performance of that technology. For photovoltaic cells, the reduction of this energy input can increase incentives for their use. Several groups have examined the input over the lifetime of photovoltaic cells for various types. Mohr et al. examined the life cycle of thin-film GaAs and GaInP/GaAs solar modules and compared them with the performance of multi-Si modules [8]. Using the energy payback time as a measure of performance, their group identified multi-Si modules to perform best with a payback time of 4.2 years, compared to 5.0 for GaAs and 4.6 for GaInP/GaAs. The metal-organic vapor phase epitaxy (MOVPE) process was found to be the largest energy consuming step in the production of the GaAs and GaInP/GaAs modules, accounting for 66% of the entire primary energy demand. In an earlier work, their group also examined the life cycle of mc-Si, InGaP and InGaP/mc-Si modules [9]. Ito et al. examined the life cycle of a 100MW scale plant operating using m-Si, a-Si, CdTe, and CIS [7]. A different group also examined several types of silicon cells, CIS, and CdTe cells [85]. A review based on EROI has also been conducted by Weissbach et al. [67].

2.8 PERFORMANCE COMPARISON OF TECHNOLOGIES

2.8.1 Life Cycle Energy Cost

As discussed above, several studies have examined the LCEC in various ways, typically depending on the technology being examined. Figure 2.5 shows the values displayed in the

Table 2.1: Summary of the conversion efficiencies for several steps in the conversion process of solar energy to electrical energy, divided by technology.

	Plant efficiency (%)	LCEC	Photo-synthesis (%)	Conversion to Coal (%)	Total Efficiency (%)
Hard Coal, underground mine	34.58 [67]	0.034 [67]	3.5	8.8	0.103
Brown coal, open pit mine	34.58 [67]	0.032 [67]	3.5	8.8	0.103
Willow, EPRI direct-fired	27.7 [45, 91]	0.101 [91]	3.5		0.872
Willow, co-firing	37.5 [94, 97]	0.250 [97]	3.5		0.984
Willow, NREL gasifier	37.2 [90, 91]	0.075 [91]	3.5		1.204
Willow, EPRI gasifier	36 [45, 91]	0.078 [91]	3.5		1.162
Willow, gasification	27.5 [95, 97]	0.125 [97]	3.5		0.842
Willow, gasification	30 [92, 97]	0.091 [97]	3.5		0.955
Poplar, biogas	32.1 [89]	0.627 [89]	3.5		0.419
Poplar, NREL gasification	37.2 [90]	0.064 [90]	3.5		1.219
Poplar, gasification	27 [93, 97]	0.333 [97]	3.5		0.630
Maize, biogas	37.2 [67]	0.286 [67]	3.5		0.930
PTC, SEGS, 80 MW	13.2 [67]	0.048 [67]			12.571
PTC model plant, 250 MW	14.3 [80]	0.122 [80]			12.558
PTC, 50 MW	15.7 [81]	0.042 [81]			15.046
PTC, SEGS, 80 MW	13.2 [82]	0.013 [82]			13.035
PTC, DSG, 80 MW	15.1 [82]	0.008 [82]			14.987
Central tower, 17 MW	16.7 [81]	0.041 [81]			16.021
Central tower, 1.5 MW	14.6 [96]	0.146 [96]			12.434
Fresnel, 80 MW	9.0 [67]	0.059 [67]			8.471
Fresnel, 80 MW	9.0 [82]	0.019 [82]			8.833
mc-Si, Poly-Si, roof	9.9 [67]	0.250 [67]			7.425
mc-Si, Poly-Si, field	9.9 [67]	0.263 [67]			7.295
mc-Si, 100 MW (multi-crystalline)	12.8 [7]	0.063 [7]			11.989
mc-Si, 100 MW, high efficiency	15.8 [7]	0.050 [7]			12.160
mc-Si, 1 kW	14.5 [9]	0.117 [9]			12.808
mc-Si, 3 kW	13.2 [85]	0.120 [85]			11.616
mc-Si, 10 MW	14.8 [8]	0.140 [8]			12.728
a-Si, roof (amorphous)	4.95 [67]	0.435 [67]			2.798
a-Si, field	4.95 [67]	0.476 [67]			2.593
a-Si, 100 MW	6.9 [7]	0.083 [7]			6.325
a-Si, 3 kW	6.5 [85]	0.100 [85]			5.850
sc-Si, 3 kW (single-crystalline)	14 [85]	0.138 [85]			12.063
ribbon-Si, 3 kW	12 [85]	0.090 [85]			10.920
CIS, 3 kW	10.7 [85]	0.093 [85]			9.701
CdTe, 100 MW	9.03 [7]	0.063 [7]			8.458
CdTe, 3 kW	7.1 [85]	0.090 [85]			6.461
InGaP,thin-film, module 1 KW	15.5 [9]	0.210 [9]			12.245
GaAs, thin- film, 0.1 MW	23.3 [8]	0.167 [8]			19.417
GaInP/GaAs, thin-film, 0.1 MW	28.5 [8]	0.153 [8]			24.130
InGaP/mc-Si module, 1 kW	25 [9]	0.177 [9]			20.583

form of EROI. Here, higher values of EROI imply greater energy return, and thus are desired. All of these methodologies can, of course, be converted into explicit LCEC values. Figure 2.6 shows the results for the LCEC for each of the four technologies examined for studies of specific plants. When using this as a measure of comparison, the lowest value is desired, as it implies that the energy input requirement is much less than the potential output.

Several observations can be made from the results shown in Figure 2.6. There is a large variation in values for each renewable technology. This is partially due to the fact that various sub-types of each technology were examined. Another reason for this is that these technologies have not achieved maturity, causing some values to be based on studies of prototypes. This is evident in the smaller variation of the values for solar thermal power production, a technology that has been around for several decades. It is also worth noting that while there are some significantly high LCEC values for PV and biomass power production, the average for each is 0.16 and 0.20, respectively. This translates to each technology producing five or more times more energy than it consumes, an acceptable ratio.

2.8.2 Life Cycle Solar Efficiency Based on Solar Input

The goal of this study is to obtain an equivalent energy metric for the various technologies that were examined. The LCEC values, various power plant efficiency values, and other conversion steps can all be combined in the following way:

$$\eta_{overall} = \begin{cases} \text{PV} \rightarrow & \eta_{PVmodule} \\ \text{Solar Thermal} \rightarrow & \eta_{\eta_{SolarPlant}} \\ \text{Biomass} \rightarrow & \eta_{photosynthesis} \times \eta_{BiomassPlant} \\ \text{Coal} \rightarrow & \eta_{photosynthesis} \times \eta_{ConversionToCoal} \times \eta_{CoalPlant} \end{cases}$$

$$\eta_{LifeCycleSolarEfficiency} = \eta_{overall} \times (1 - LCEC) \tag{2.11}$$

The range of values for this metric is shown in Table 2.1 and plotted in Figure 2.7. Unlike the measure of LCEC, the overall solar efficiency measures the ratio of energy delivered by the sun to electricity produced, and thus a higher value is desired. It is immediately

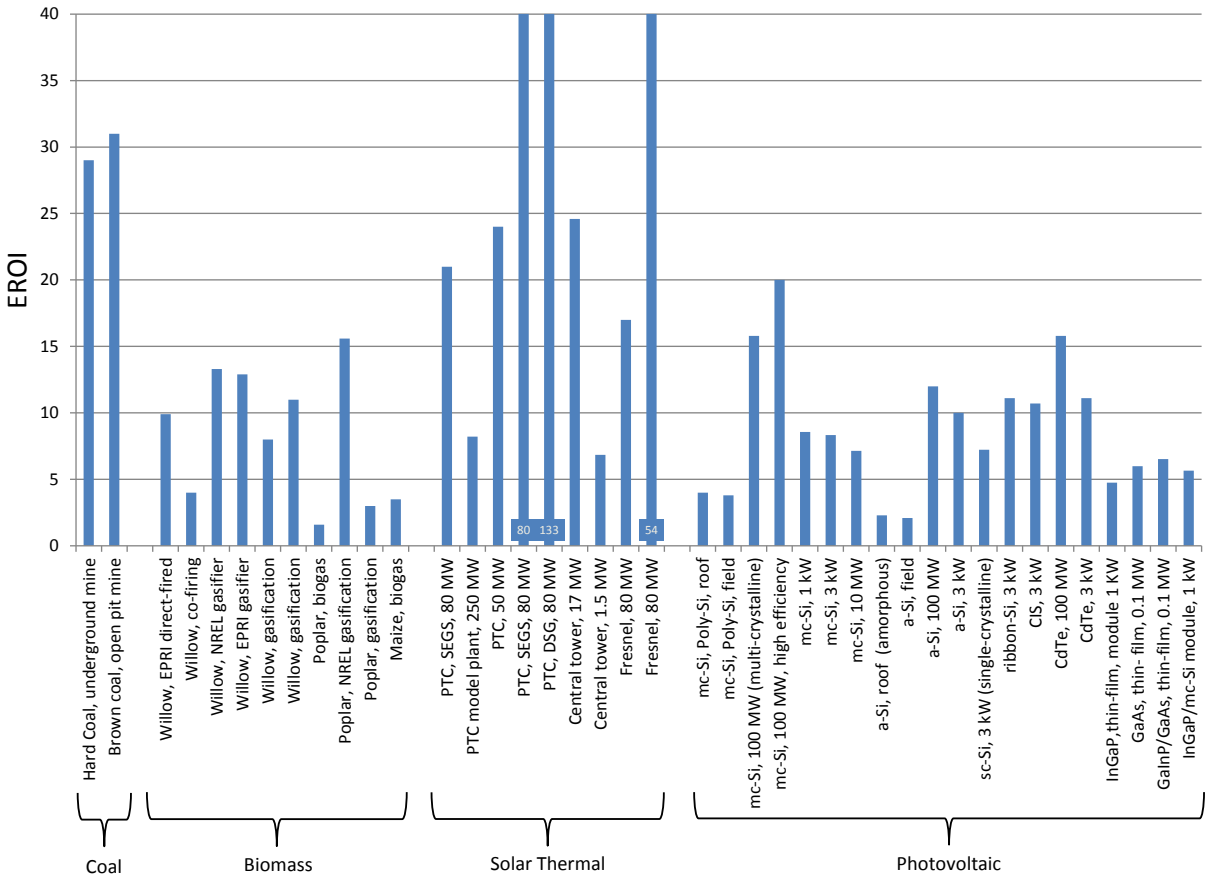

Figure 2.5: EROI values for the power generating technologies analyzed in this work.

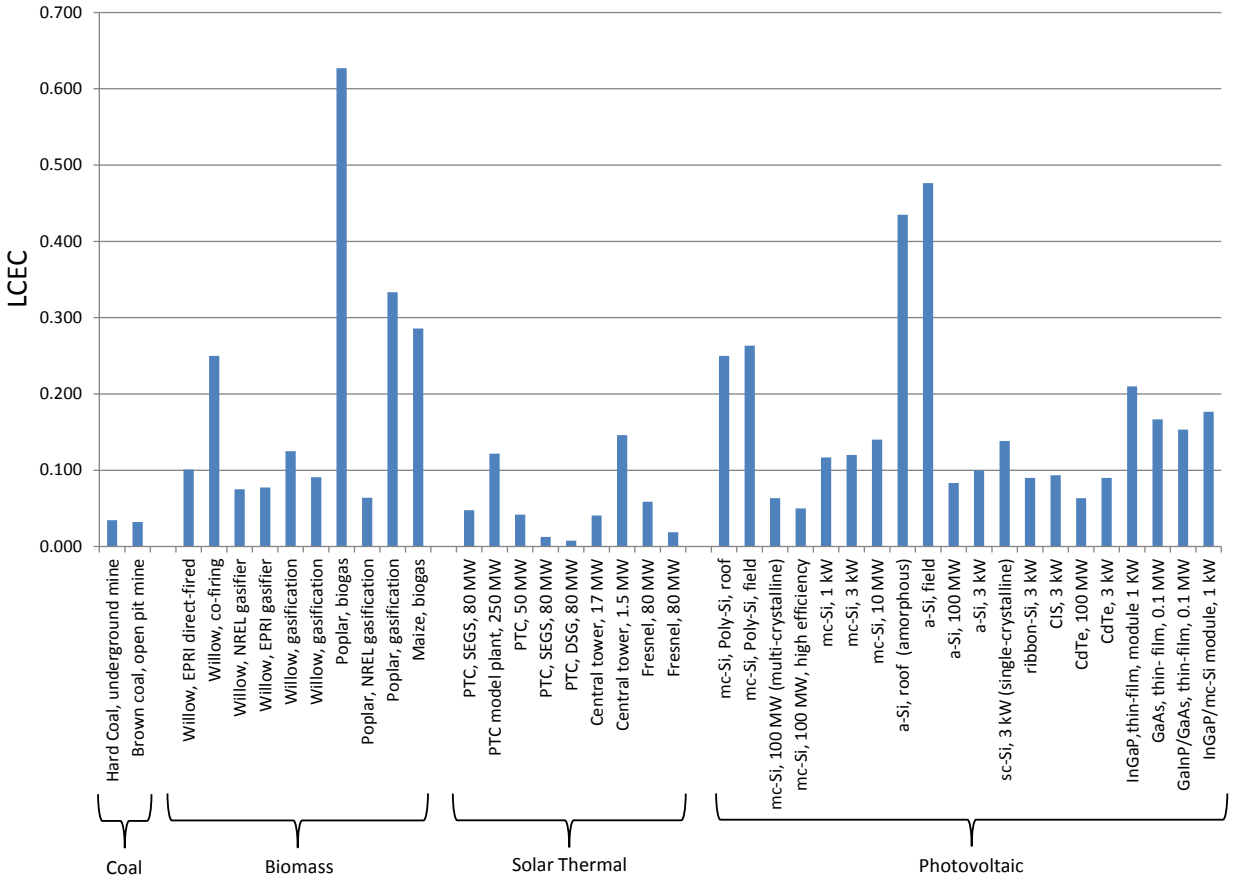

Figure 2.6: LCEC values for the power generating technologies analyzed in this work.

apparent that while photovoltaic and solar thermal technologies have lower plant efficiency values, they have significantly higher total efficiency values than biomass and coal. This is emphasized in Figure 2.7, where the total values for coal are so small as to be nearly imperceptible. This is due to the inefficiency of photosynthesis and extraction of energy stored in plant material. It is worth noting that while the solar efficiency of coal power is lower than that of biomass, there is less than an order of magnitude difference between the two technologies, implying that the largest impact on efficiency is in the conversion of solar energy into stored energy in biomass. It is additionally important to evaluate the validity of the values used in this study. While the evaluation is based on energy and LCEC values acquired for specific plants, exergy analyses have shown that the types of plants evaluated in this study have similar values for the energy and exergy. Exergy is an important metric in evaluating overall performance, and, based on the above, an exergy study is expected to produce similar results.

The results for solar thermal and PV technologies show a large amount of variation. While the results for the LCEC implied that solar thermal technology requires a smaller energy investment, the difference proves to be small, when combining that result with the efficiency of the plant for both technologies. The variation of the performance efficiencies has a large impact on the overall solar efficiency. The performance of PV materials varies from 2.5% to somewhat less than 25%. The best performing technologies were PV plants utilizing GaInP/GaAs, InGaP/mc-Si, and GaAs. The LCEC can be seen to have a large impact on the performance, reducing the highest efficiency technology from an initial efficiency of 28.5% to a total efficiency of 24%.

2.9 CONCLUSIONS

Several electricity production sources were examined for the efficiency of converting solar energy to electrical energy over their lifetime. The energy requirement over the lifetime for each technology was additionally examined and then accounted for in the overall efficiency analysis. It can be seen that the photovoltaic and solar thermal power production is the most

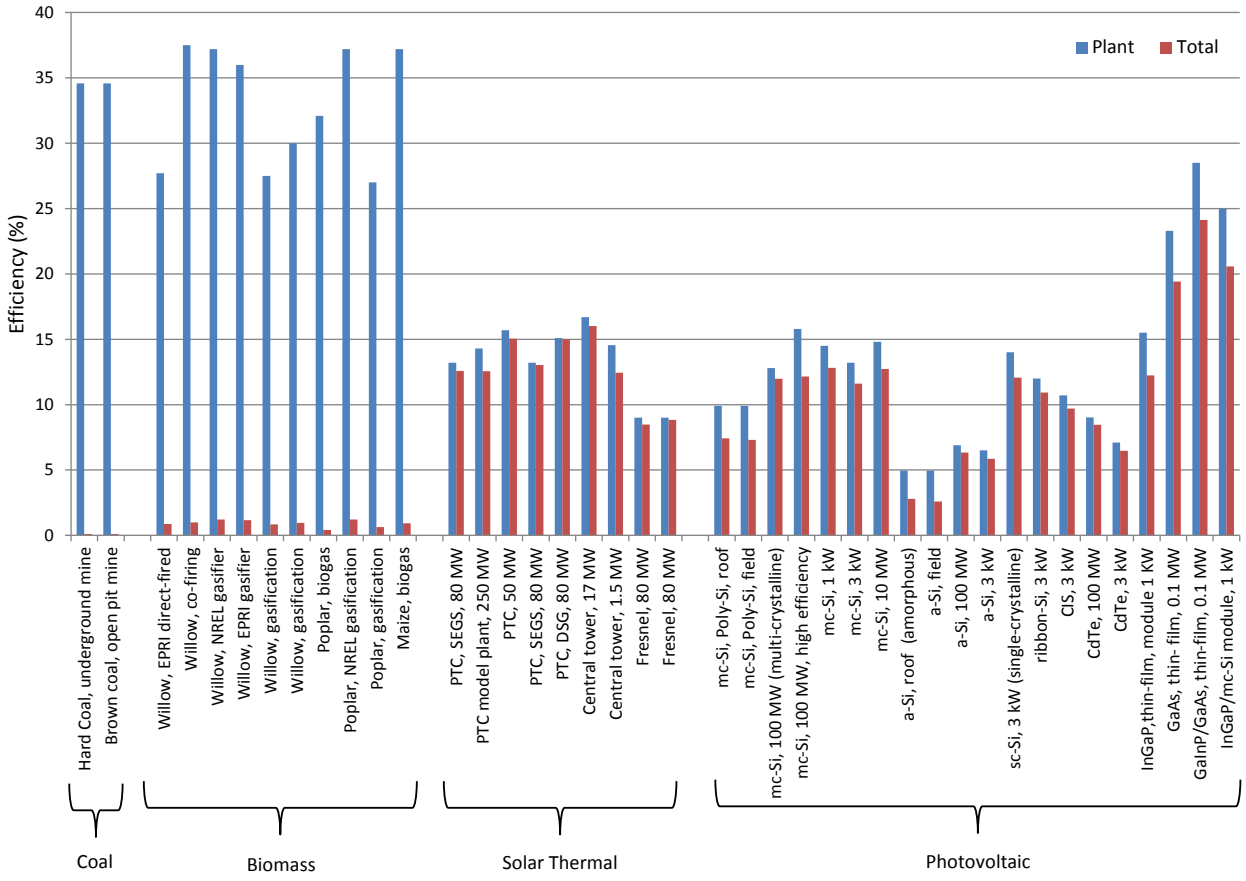

Figure 2.7: Overall life cycle solar efficiency of the technologies analyzed.

efficient in converting solar energy to electrical energy. It was found that photosynthetic conversion of solar energy to biomass is inefficient and is a large bottleneck for biomass-utilizing technologies. This bottleneck reduces the overall efficiency for biomass and coal. As a result, larger amounts of area are required for capturing an equivalent amount of sunlight for biomass, as compared to solar thermal and photovoltaic technologies. This becomes an ever increasing issue due to the impacts of deforestation and the shrinking amount of harvestable land. Use of rotating crops, such as maize, willow, and poplar, can reduce these effects, when they are not in competition with other potential uses for the land.

When considering the implications for coal, the above results imply that the process of storing large amounts of carbon underground naturally was inefficient, leading to the conclusion that our use of this stored biomass is inherently undesirable from the perspective of carbon balance. The use of coal thus releases large amounts of CO_2 without allowing for an ability to balance this output.

3.0 PERFORMANCE EVALUATION OF A PVT/ORC (PHOTOVOLTAIC THERMAL/ORGANIC RANKINE CYCLE) SYSTEM WITH OPTIMIZATION OF THE ORC AND EVALUATION OF SEVERAL PV (PHOTOVOLTAIC) MATERIALS

The work above shows the potential of both photovoltaic and solar thermal technologies as efficient pathways to capturing and converting solar energy to electricity. It is logical to consider if combining the two technologies together would produce even better results. Several groups have previously evaluated ways of combining photovoltaic cells with bottoming thermal applications, but there is limited research on the combination with an ORC. Thus, the goal of this part of the study is evaluate several working fluids and ORC configurations to identify an optimum combination and evaluate how this pairs with a PV cell. Since there are many types of cells that behave drastically differently at higher temperatures, five types of cells were examined to identify which would have the most benefit of being combined with an ORC.

3.1 LOW TEMPERATURE RANKINE CYCLE DESIGNS FOR RENEWABLE ENERGY APPLICATIONS

A standard Rankine cycle is typically operated with steam, the standard fluid found in turbines generating electricity in coal power plants. The diagram of a simple Rankine cycle is shown in Figure 3.1 with the temperature and entropy behavior for the cycle displayed in Figure 3.2. The cycle generates energy by using high pressure and temperature steam produced from evaporating water at high pressure in the boiler. The steam is subsequently

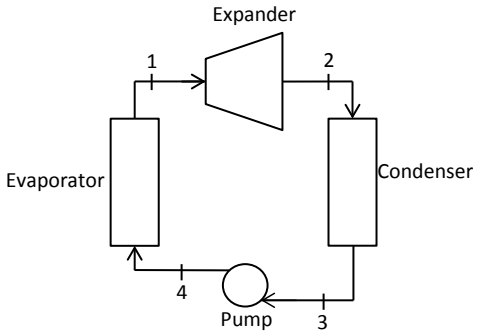

Figure 3.1: Simple steam cycle diagram.

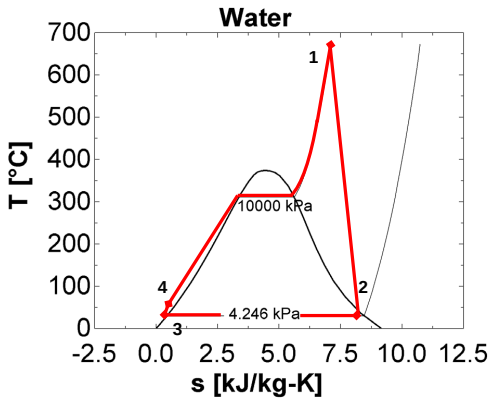

Figure 3.2: T-s diagram for a steam Rankine cycle.

condensed into water and pumped up to a high pressure using a pump, the latter requiring little work since water is nearly incompressible.

The vapor dome for water in Figure 3.2 can be seen to be nearly symmetric. This, however, is not always the case. Fluids can be assigned to three categories: dry fluids (n-Pentane), wet fluids (Ammonia), and isentropic fluids (R11). The categories are based on the slope of the vapor saturation curve, with dry fluids having a positive slope, wet fluids having a negative slope, and isentropic fluids having a nearly vertical slope, as shown in Figures 3.3, 3.4, and 3.5. Dry fluids are often used in low-temperature ORCs, since the outlet of the turbine is guaranteed to be in the superheated vapor region, and liquid condensation is not a threat to the expanders. Additionally, internal heat exchangers can be utilized to recover low temperature heat from the turbine outlet for preheating, often proving to be quite effective in raising the overall efficiency of the system.

The behavior of organic fluids makes them excellent candidates for low temperature applications. There are numerous studies of ORC optimization, such as the saturated vapor [14, 98–100], superheated vapor [101–105], supercritical [106–109], transcritical [110, 111], and closely related flash [107, 112, 113] and Kalina cycles [114]. One area of focus for low temperature ORCs has been in identifying the behavior of various fluids in achieving best

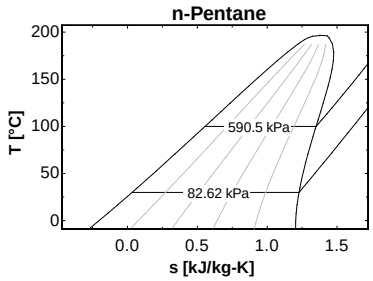

Figure 3.3: Dry Fluid.

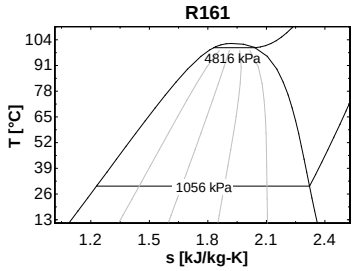

Figure 3.4: Wet Fluid.

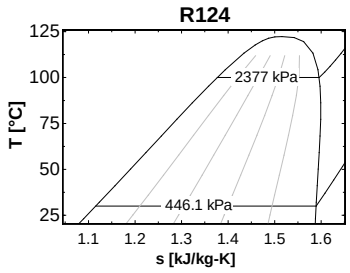

Figure 3.5: Isentropic Fluid.

performance for given applications. Saleh et al. performed such a study on 31 working fluids for a geothermal application with a high temperature of 100^oC and a low temperature of 30^oC [108]. Their group studied a simple design and compared it to the performance of the cycle with an internal heat exchanger. A similar study performed by Wang et al. examined the behavior of one fluid in several cycle configurations, some of which are more typical for steam cycles [101]. An interesting variation of the standard Rankine cycle is a design where the evaporation takes place above the vapor dome. This cycle is called a transcritical cycle and typically operates using CO_2 for low to medium temperature applications. This configuration can be altered to have the entire cycle operate above the critical point and is typically referred to as a supercritical cycle. A different approach can be taken with a Rankine cycle to operate only partially in the superheated vapor region. The organic flash cycle (OFC) is an example of this. Studied thoroughly by Ho et al., this cycle has the advantage of almost entirely eliminating pinch points, allowing for better heat transfer from a high temperature fluid stream to the working fluid [113].

There are a wide variety of applications for ORCs and other low temperature cycles. While they are often associated with geothermal power generation [98], there are several studies that have examined other applications of ORCs. A study by Freeman et al. examined a solar-powered ORC combined with a hot water tank [115]. An application for waste heat utilization was examined by Le et al. where many potential waste heat sources from industrial

processes are paired with an ORC utilizing configurations of pure and zeotropic mixtures [116]. The concept of using Rankine cycles as bottoming cycles in power production has been thoroughly applied to traditional gas turbine power plants, and has been examined in more novel Brayton cycle concepts, such as the study by Akbari and Mahmoudi of a supercritical CO2 recompression Brayton/organic Rankine cycle (SCRB/ORC) [117]. A different group examined potential use of biomass in CHP with an ORC, with the system providing a source of power and drying heat for a sawmill [118]. While many focus on using complex cycles to maximize efficiency and performance, others have focused on novel combinations. One such combination was proposed and studied by Buonomano et al. where a low-temperature thermal well at 95^oC is combined with a solar collector operating at up to 130^oC [119].

3.2 PREVIOUS STUDIES ON PV COMBINED WITH BOTTOMING CYCLES

Several studies have examined combinations of PV and bottoming cycle applications. A low temperature application ($60 - 80^oC$) was examined by Al-Alili, et al. that utilized a CPVT system with a desiccant wheel cycle [120]. Calise et al. studied a novel trigeneration system using PVT and operating at 80^oC to produce electricity, space heating and cooling, and domestic hot water [121]. They found that the system can be technically and economically viable, provided that there are government incentives for solar energy systems. Mittelman et al. examined a combination of a PV system and an absorption chiller operating at temperatures between 65^oC and 120^oC [16]. They have found that the thermal efficiency increases with increasing temperature. Additionally, a cost analysis showed that the system could be economically feasible. Their group later examined a concentrating photovoltaic/thermal (CPVT) desalination system [17], showing that the system could be economically competitive with existing desalination technologies.

While other applications of PV/T and CPVT have been more thoroughly studied, there is limited research on the optimization of a combined PV/ORC system. Kosmadakis et al. previously examined the combination of silicon cells and an ORC operating with R-

245fa at an evaporation temperature of 90^oC and 130^oC [14]. The initial design called for a combination of a CPV system that operates at 100^oC, and an ORC with a high temperature of 90^oC, allowing a 10^oC temperature drop between the CPV and ORC system due to heat transfer. This system produced a combined efficiency of 9.81%, which was an improvement over the 6.35% achieved solely by the CPV system. They then improved the design by raising the CPV operating temperature to 140^oC and the the evaporation temperature to 130^oC. This resulted in a total efficiency boost up to 11.83%. Their group followed the thermodynamic analysis with an economic comparison of the combined CPV-ORC system and the CPV system operating alone and showed that the combined system had a better return on investment.

3.3 COMBINING ORC DESIGN, WORKING FLUID SELECTION, AND PV CELL TYPE AND OPERATION

The work proposed herein examines the use of several types of cells in a system that produces electricity using PV, and utilizes the waste heat from the cells to drive an ORC. The cell types being examined are silicon (Si), gallium arsenide (GaAs), indium phosphide (InP), cadmium sulfide (CdS), and triple-junction indium gallium phosphide (InGaP)/indium gallium arsenide (InGaAs)/germanium (Ge) at various concentrations. The efficiency of each type at 110^oC is predicted using the data provided in Table 3.1, acquired from previous studies on PV cell behavior at various temperatures [10, 122]. This work expands further on previous research by analyzing several ways to increase performance (in terms of efficiency) of such a system, with the goal of identifying a combination of PV and ORC parameters that make the best case for combining the two technologies. Finally, the optimum configuration is examined for varying operating temperatures to identify the possible optimum operating temperature within a reasonable PV cell operating range.

Table 3.1: PV cell efficiency and temperature characteristics

					InGaP/InGaAs/Ge triple-junction (TJ)		
Type/Solar Concentration	Si	GaAs	InP	CdS	1x	17x	200x
Efficiency (η)[%] at 25^oC	26.0	28.1	28.2	14.3	29.5	34.4	37.0
Slope $d\eta/dT$ [%/100^oC]	-8.47	-6.51	-7.01	-.83	-7.30	-4.86	-3.63

3.4 THERMODYNAMIC CYCLE ANALYSIS

The simplest ORC consists of an evaporator, expander, condenser, and pump, as shown in Figure 3.6. The cycle operates by utilizing work from high pressure saturated vapor via an expander. The vapor exiting the expander (state 2) is at a low pressure and is moved through a condenser until it reaches a liquid state (state 3), after which it is pumped up to a high pressure (state 4), and heated at high pressure until it reaches a saturated vapor state (state 1), completing the cycle. The steps for this cycle are shown in Figure 3.7 on a T-s diagram for n-Pentane. An internal heat exchanger (IHE) can be used for dry fluids to recover lost heat from the low pressure vapor (state 2), as shown in Figures 3.8 and 3.9. An alternate modification can be utilized in the form of a medium pressure bleed into an open feed organic fluid heater (OFOH, with the entrance at state 3), shown in Figures 3.10 and 3.11.

A more complex version of this can be seen in Figures 3.12 and 3.13, where the heater operates as a closed feed organic fluid heater (CFOH) and mixes after preheating (states 3 to 7) the fluid in the main line (states 5 to 6). The internal heat exchanger can be combined with the closed feed organic fluid heater (CFOH-IHE), as shown in Figures 3.14 and 3.15. This final configuration has the potential for high efficiency when used for dry fluids and a high bleed temperature. It is important to note that Figures 3.7, 3.9, 3.11, 3.13, and 3.15 show the T-s behavior of n-Pentane for each of the configurations. This behavior will vary somewhat depending on the fluid used in each configuration. These cycles have previously

been analyzed in other works, such as that by Wang et al. [101] and Saleh et al. [108], and have been summarized in the review by Saadatfar et al. [123].

Models for the various configurations were designed based on the input/output relationships of the various components. Standard conservation of mass, conservation of energy, isentropic efficiency, and effectiveness equations were formulated for all of the state points and processes of the cycles, and were solved using Engineering Equation Solver (EES) [124], which also supplied the thermofluid properties for the various working fluids. The simplest components in each system were the evaporator and condenser, calibrated to evaporate a fluid at 100^oC and condense it at 30^oC, varying the pressure based on the individual fluid properties. Each configuration was designed to heat the fluid until it reached a saturated vapor state (x=1), and condense it until it reached a saturated liquid state (x=0). The use of saturated vapor proved beneficial for the application of this cycle. In a design that utilizes photovoltaic cells, it is undesirable to have cells in series where some cells are at a higher temperature than others. This would simultaneously reduce the efficiency of the whole series of cells, while also degrading some cells at a faster rate due to the higher temperatures. Since the system is designed for the working fluid to directly cool the cells via convection, the saturated vapor condition maintains a near constant temperature throughout the heating process via evaporation.

Each configuration was designed to operate using a single stage turbine/expander with an isentropic efficiency of 85% and a pump with an isentropic efficiency of 65%. The exit of the turbine was calculated based on a known condensing pressure, as follows:

$$h_{2,s} = f(s_1, P_2) \tag{3.1}$$

$$h_2 = h_1 + \eta_t(h_{2,s} - h_1) \tag{3.2}$$

The pump exit properties are calculated in a similar fashion:

$$h_{4,s} = f(s_3, P_4) \tag{3.3}$$

$$h_4 = h_3 + \frac{1}{\eta_p}(h_{4,s} - h_3) \tag{3.4}$$

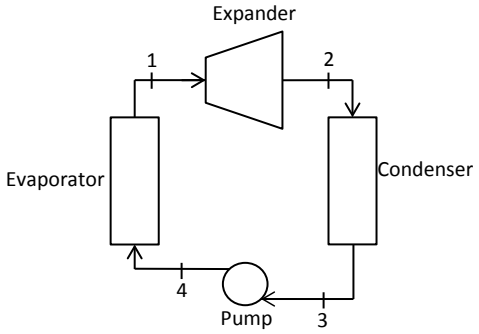

Figure 3.6: Simple ORC diagram.

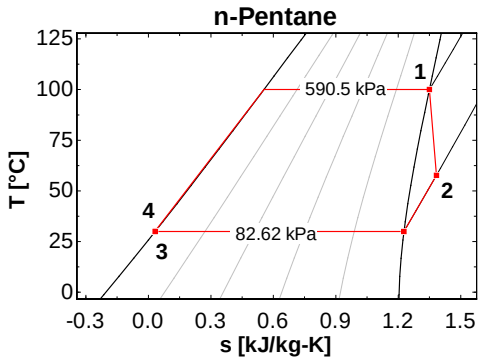

Figure 3.7: Simple ORC T-s diagram.

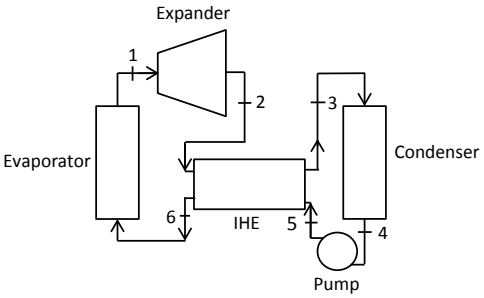

Figure 3.8: IHE ORC diagram.

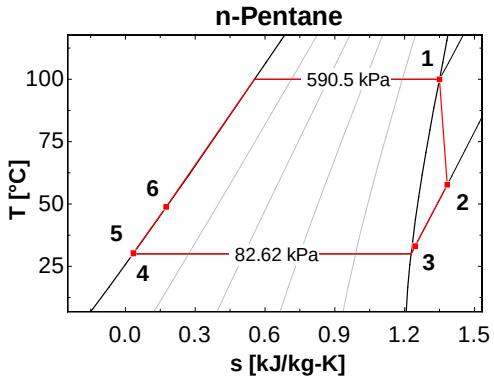

Figure 3.9: IHE ORC T-s diagram.

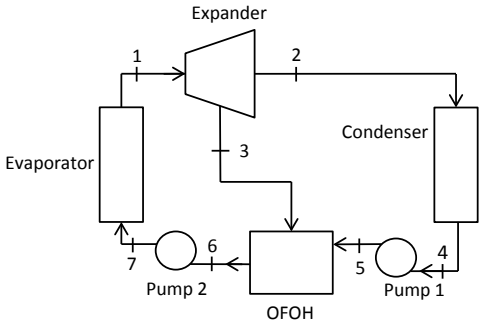

Figure 3.10: OFOH ORC diagram

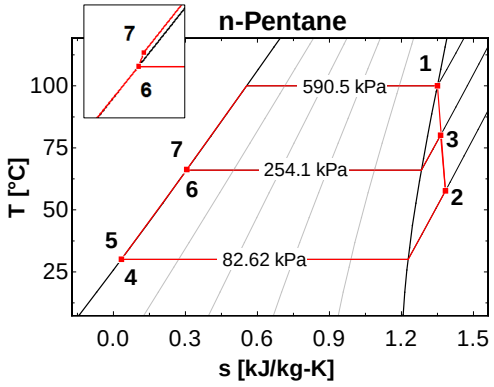

Figure 3.11: OFOH ORC T-s diagram.

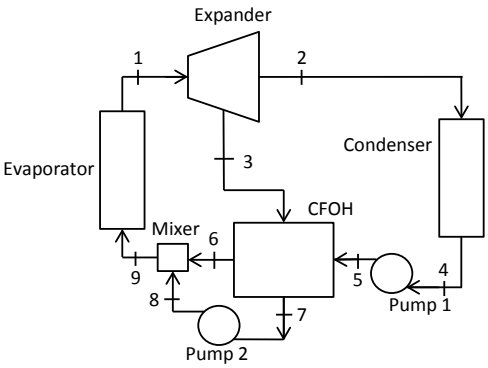

Figure 3.12: CFOH ORC diagram.

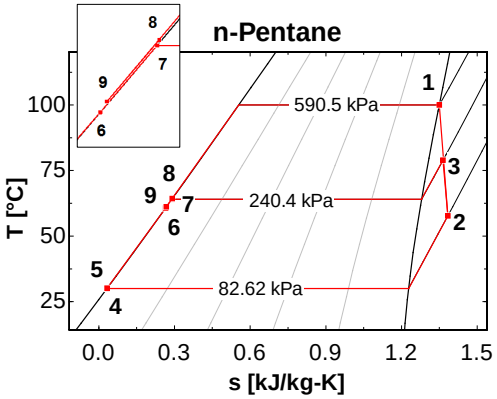

Figure 3.13: CFOH ORC T-s diagram.

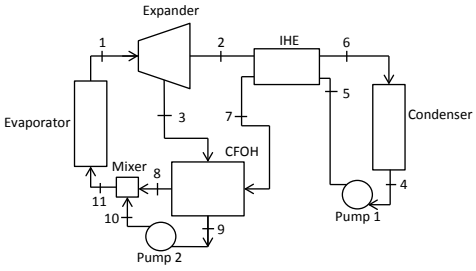

Figure 3.14: CFOH IHE ORC diagram.

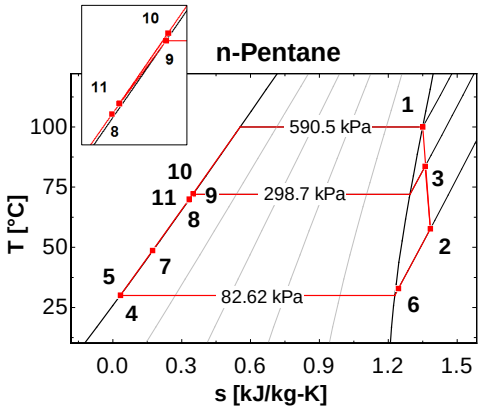

Figure 3.15: CFOH IHE ORC T-s diagram.

The variable subscripts in the above equations are numbered in relation to the states found in the diagram for the simple ORC.

An IHE was implemented in two of the configurations in this investigation. It had the purpose of recovering heat from the exhaust of the turbine to preheat liquid after pumping to a higher pressure. This was treated as a simple counter-flow model with an effectiveness of 0.8. The input and output states can be calculated as follows:

$$\epsilon = \frac{T_2 - T_3}{T_2 - T_5} \tag{3.5}$$

$$h_6 - h_5 = h_2 - h_3 \tag{3.6}$$

The states referenced in the above two equations correspond to the states shown in Figures 3.8 and 3.9, where the properties of states 2 and 5 are known. State 3 can be found using equation 3.5 and a known pressure, and state 6 can be found using equation 3.6 and a known pressure.

The effect of an OFOH on performance was examined in the third configuration. The OFOH was designed so that the exit state (state 6 in Figures 3.10 and 3.11) was a saturated liquid (x=0). This specification allowed a calculation of the bleed fraction, as shown:

$$y = \frac{h_6 - h_5}{h_3 - h_5} \tag{3.7}$$

The CFOH configuration consisted of the heat exchanger and a mixer, as shown in Figures 3.12 and 3.13. The exit condition was specified in state 7 as a saturated liquid. The equation for the heat exchanger in the second configuration was modified for the CFOH to act as a condenser, as shown:

$$\epsilon = \frac{T_6 - T_5}{T_{3,cond} - T_5} \tag{3.8}$$

An additional equation was required based on an energy balance relating the bleed ratio (y) to the enthalpies:

$$y = \frac{h_6 - h_5}{h_3 - h_7 - (h_5 - h_6)} \tag{3.9}$$

The mixer operated in similar fashion to the OFOH, as shown:

$$h_9 = yh_8 + (1 - y)h_6 \tag{3.10}$$

The final configuration utilized a combination of an IHE and a CFOH and was analyzed using the corresponding equations.

An optimization of the condensing temperature ($T_{3,cond}$) for the bleed superheated fluid was required for the last three configurations. This was carried out using a parametric study to the nearest tenth of a degree and is shown in Table 3.3 for the OFOH and CFOH configurations, and in Table 3.4 for the IHE and CFOH configuration (Table 3.2 shows the performance parameters for the simple cycle). The optimized temperature for the bleed dictated the intermediate pressure due to the requirement of the saturated liquid state at the exit of the OFOH and CFOH. Secondary pumps, operating at the efficiency listed above, were used in these configurations to raise the pressure from the intermediate pressure (P_3) to a high pressure (P_1).

3.5 CYCLE PERFORMANCE AND FEASIBILITY

3.5.1 Performance of the Five Configurations

The above configurations were analyzed for twenty-seven fluids, chosen based on the literature survey described above, and available ranges of accurate data on fluid behavior. Of these, there were fairly common refrigerants and alkanes, as well as more atypical fluids, such as R11 and hexane. An analysis of the basic cycle was first performed to obtain performance based on efficiency ($\eta_{th,S}$), the volume ratio between the outlet and inlet of the turbine ($\dot{V}_2/\dot{V}_1$), the volumetric flow rate at the exit of the turbine ($\dot{V}_2$), and the mass flow rate at the exit of the turbine ($\dot{m}$). While an evaluation of efficiency is self-explanatory, it is important to identify the necessity for the remaining metrics. The volume ratio identifies the amount of expansion that a fluid undergoes in the turbine, with a typical maximum value of ten for a single stage (an axial turbine design is assumed). The volumetric flow rate identifies the amount of volume of gas necessary to produce a given amount of power (1 MW for this study, which requires an approximate PV field size of 1 hectare, based on $\sim 1kW/m^2$ of solar insolation). Larger values will require large turbines for the same amount

of power and are therefore undesirable. Some fluids in the study resulted in prohibitively high values, resulting in their exclusion from comparison analyses described later in this section. Mass flow rates depend on volumetric flow rates and fluid density, and are used in sizing the components of a cycle.

Table 3.2 summarizes the key parameters for each fluid for the basic ORC. The performance parameters described above are provided in the columns on the right side of the table. It is immediately apparent that R11 has the best performance with the highest efficiency, an acceptable volume ratio, and a comparably low volumetric flow rate. However, environmental aspects described later, as well as improvements in performance of other fluids in more advanced cycles, prevent it from being a recommended working fluid. Heavy alkanes, from n-Heptane to n-Dodecane, show good potential in efficiency, but as already mentioned, have prohibitively high volume ratios and volumetric flow rates and are also not recommended as working fluids. Several fluids have also shown outlet states that consist of a mixture of liquid and vapor, and are thus unacceptable in the scope of this study due to the nature of the turbine design. While expanders that operate within the vapor dome have previously been examined, they are technologically complex and are outside the scope of this study.

Three configurations were examined after the basic cycle: IHE, OFOH, and CFOH ORCs (Table 3.3). Additional key performance characteristics for the IHE configuration are the outlet temperature of the vapor, T_3, and outlet temperature of the liquid, T_6. These provide a measure of useful heat recycled before entering the condenser, and can be compared to T_2, the temperature at which the vapor would enter the condenser without the IHE. As can be seen in Table 3.3, some fluids were excluded from the IHE configuration. These fluids display wet behavior, causing the output state 2 to be at the saturation temperature. For both the OFOH and the CFOH, the fraction of fluid, y, used in preheating and the condensing temperature of the feed fluid, $T_{3,cond}$, are important in describing the optimal states of performance. All three configurations show increases in performance when compared to the basic cycle. Fluids with a higher turbine exiting temperature, T_2, proved to benefit significantly from the use of the IHE, while those that had lower exiting temperatures showed higher increases from the cycles utilizing feed fluid heaters. The IHE configuration proved to have the best impact on heavy alkanes, with n-Dodecane having the highest efficiency at

Table 3.2: Simple ORC performance parameters

Fluid	$T_c[^oC]$	$x_2[\%]$	$T_2[^oC]$	$P_2[kPa]$	$P_1[kPa]$	$\dot{m}[kg/s]$	$\dot{V}_2[m^3/s]$	$\dot{V}_2/\dot{V}_1$	$\eta_{th,S}$
R11	198	100	35.04	125.3	817.4	35.15	0.8186	6.118	0.1358
R12	112	93.47	30	744.3	3342	68.97	0.2693	5.642	0.103
R114	145.7	100	54.87	249.8	1406	51.08	0.4779	6.415	0.119
R123	183.7	100	47.8	109.7	786.8	35.99	0.7639	7.216	0.1321
R124	122.3	100	37.17	446.1	2377	49.91	0.2845	6.625	0.1181
R134a	101	83.4	30	770.6	3975	61.34	0.1613	8.495	0.1015
R141b	204.2	100	42.04	94.16	677.2	27.5	0.9202	6.889	0.1345
R142b	137.1	100	34.34	390.9	2079	34.36	0.3404	5.933	0.1254
R152a	113.3	89.97	30	690.7	3511	30.69	0.208	6.212	0.1173
R161	102.1	76.46	30	1056	4816	33.57	0.1645	6.402	0.1053
R227ea	102.8	100	35.03	526.5	2827	79.66	0.1934	10.09	0.09995
R236fa	124.9	100	46.5	320.4	1936	47.95	0.3124	7.672	0.1171
R245fa	154	100	47.42	177.2	1269	33.85	0.4627	7.773	0.1264
R1234ze(E)	109.4	99.14	30	579.7	3027	49.81	0.2142	7.425	0.1108
RC318	115.2	100	55.27	365.5	2054	67.64	0.2877	8.053	0.107
Isobutane	134.7	100	45.78	404.5	1984	20.58	0.3627	5.822	0.121
Isobutene	144.9	100	41.57	351.5	1842	18.49	0.3841	5.848	0.1259
n-Butane	152	100	48.33	283.9	1526	17.84	0.4537	5.937	0.1257
Isopentane	187.2	100	57.57	109	721.2	17.51	0.859	6.884	0.1276
n-Pentane	196.5	100	57.68	82.62	590.5	16.46	1.018	7.255	0.1285
Isohexane	224.6	100	62.79	34.58	308.5	16.86	1.761	8.834	0.1285
n-Hexane	234.7	100	61.68	25	240	16.2	2.206	9.366	0.1299
n-Heptane	267	100	63.64	7.776	106.2	15.84	4.362	12.98	0.1304
n-Octane	296.2	100	64.88	2.437	47.02	15.72	8.83	17.93	0.1309
n-Nonane	321.4	100	65.83	0.7968	21.03	15.83	17.86	24.42	0.1302
n-Decane	344.6	100	66.11	0.2556	9.605	15.79	35.42	34.56	0.1307
n-Dodecane	385	100	66.41	0.02682	2.029	15.79	140.3	69.55	0.1305

0.148, an improvement of 8.98% over the highest value for the basic cycle (R11). This was also the highest value out of the three configurations in the table. R11 was found to have the highest values for the OFOH (0.1454) and CFOH (0.1469) configurations. Overall, alkanes with high turbine exit temperatures showed a smaller increase in performance in the OFOH and CFOH configurations, due to the loss of useful heat to condensing, while refrigerants R11, R141b, and R123 maintained the highest performance values, similar to the basic case. Additionally, in most cases, the CFOH configuration proved to perform better than the OFOH.

An advanced configuration, utilizing an IHE and a CFOH, as shown in Figures 3.14 and 3.15, was then examined. In addition to the efficiency and volumetric flow rate, the key performance indicators for this configuration were the feed fluid fraction, y, condensing temperature of the feed, $T_{3,cond}$, heat exchanger gas outlet temperature, T_6, and liquid outlet temperature, T_7, and are shown in Table 3.4. Additionally, the volumetric flow rate at the turbine outlet was again examined to observe the impact of using a feed fluid heater, compared to the basic cycle case. N-Pentane, Isopentane, and other heavier alkanes showed the highest performance, with several resulting in an efficiency greater than 0.15. All of the fluids showed higher performance levels than other configurations. However, all fluids, with the exception of R227ea, additionally showed higher volumetric flow rates for this configuration, compared to the basic case. The use of a bleed was concluded to be the result, requiring a higher mass flow to produce comparable expander work. The highest efficiency was produced by n-Dodecane at 0.1526, an increase of 12.4% over the highest value of the basic case. (It is later shown that other factors exclude R11 from being a usable fluid, as well as n-Dodecane.)

The efficiency performance of acceptable fluids based on the criteria of volumetric flow rate and volume ratio for all of the ORC configurations can be seen in Figure 3.16. The heavy alkanes, such as Isopentane, n-Pentane, Isohexane, and n-Hexane, can be seen to have the highest performance when operated using the cycle that combines IHE and CFOH. Other fluids, such as R11, R123, and R141b, also show high performance. Additionally, R245fa, R114, and n-Butane show comparable, slightly lower values and have the potential to be recommended based on other metrics.

Table 3.3: ORC performance parameters for IHE, OFOH, and CFOH configurations

Fluid	Internal Heat Exchanger (IHE)			Open Feed Organic fluid Heater (OFOH)			Closed Feed Organic fluid Heater (CFOH)		
	$T_3[^oC]$	$T_6[^oC]$	$\eta_{th,IHE}$	y	$T_{3,cond}$ $[^oC]$	$\eta_{th,OFOH}$	y	$T_{3,cond}$ $[^oC]$	$\eta_{th,CFOH}$
R11	31.79	33.21	0.1371	0.1559	65	0.1454	0.1304	61.9	0.1469
R12	–	–	–	0.2377	62	0.1139	0.1257	48.5	0.1369
R114	36.2	44.92	0.1301	0.2406	65.8	0.1321	0.1891	60.5	0.1366
R123	33.95	40.11	0.1387	0.1911	65.6	0.1434	0.1639	63.3	0.1444
R124	32.79	34.88	0.1207	0.2559	65.1	0.1311	0.1911	58.5	0.1382
R134a	–	–	–	0.3015	61.2	0.1138	0.1980	52.4	0.1308
R141b	32.99	36.81	0.1382	0.1693	65.6	0.1447	0.1447	63.3	0.1456
R142b	32.03	33.11	0.1266	0.2171	65	0.1372	0.1651	59	0.1424
R152a	–	–	–	0.2462	64.3	0.1292	0.1693	55.8	0.1397
R161	–	–	–	0.2766	61.4	0.1169	0.1677	50.8	0.1361
R227ea	32.71	33.93	0.1017	0.3246	61.8	0.1134	0.2301	54.5	0.1266
R236fa	34.31	40.06	0.1248	0.2676	65.5	0.1308	0.2098	60.2	0.136
R245fa	34.06	40.36	0.1338	0.2206	65.7	0.1388	0.1846	62.5	0.141
R1234ze(E)	–	–	–	0.2865	64.1	0.1240	0.2023	56.2	0.1348
RC318	36.18	45.68	0.1213	0.311	65.5	0.1216	0.2401	59.7	0.1283
Isobutane	34.35	40.04	0.1278	0.2398	65.6	0.1336	0.1811	59.3	0.1392
Isobutene	32.83	37.12	0.1306	0.2612	72.4	0.1341	0.2037	66.4	0.1378
n-Butane	34.55	41.47	0.1334	0.2151	65.7	0.1376	0.1719	61.1	0.1409
Isopentane	35.88	47.21	0.1398	0.203	66.1	0.1392	0.1736	63.7	0.1401
n-Pentane	35.83	46.85	0.1402	0.1951	66	0.1398	0.1693	64.1	0.1403
Isohexane	36.71	50.39	0.143	0.1947	66.2	0.1398	0.1727	65.1	0.1395
n-Hexane	36.5	49.64	0.1422	0.187	65.6	0.1411	0.1677	64.8	0.1406
n-Heptane	36.78	50.68	0.1446	0.1837	66	0.1413	0.1662	65.6	0.1405
n-Octane	37	51.51	0.1456	0.1816	66	0.1417	0.1651	65.8	0.1407
n-Nonane	37.18	52.25	0.1453	0.1804	66	0.1408	0.1644	65.9	0.1398
n-Decane	37.23	52.52	0.146	0.1797	66	0.1414	0.1638	65.9	0.1403
n-Dodecane	37.28	52.55	0.1459	0.1802	66	0.1412	0.1643	65.9	0.1401

Table 3.4: ORC performance parameters for IHE with CFOH configuration

Fluid	y	$T_{3,cond}$ $[^oC]$	$T_6[^oC]$	$T_7[^oC]$	$\dot{V}_2[m^3/s]$	$\eta_{th,IHE}$ $_{CFOH}$
R11	0.1254	62.6	31.23	32.89	0.858	0.1479
R12	–	–	–	–	–	–
R114	0.1533	66	35.37	44.49	0.5011	0.1447
R123	0.1449	67.7	33.7	39.85	0.8239	0.1488
R124	0.1773	59.7	31.82	34.19	0.2928	0.1402
R134a	–	–	–	–	–	–
R141b	0.1339	65.9	32.59	36.58	0.9812	0.1481
R142b	0.158	59.6	31.2	32.44	0.3515	0.1434
R152a	–	–	–	–	–	–
R161	–	–	–	–	–	–
R227ea	0.2131	55.2	31.39	33.25	0.191	0.1284
R236fa	0.1847	64.1	33.63	39.56	0.3327	0.1415
R245fa	0.1628	66.8	33.69	40.02	0.5002	0.146
R1234ze(E)	–	–	–	–	–	–
RC318	0.1948	65.9	35.46	45.23	0.3072	0.139
Isobutane	0.1574	63	33.56	39.45	0.3767	0.144
Isobutene	0.1923	69.4	32.74	37.03	0.4352	0.1411
n-Butane	0.1481	65.7	34.02	41.01	0.4798	0.1463
Isopentane	0.1407	71.4	35.67	46.99	0.9324	0.1486
n-Pentane	0.1382	71.8	35.66	46.67	1.107	0.1483
Isohexane	0.1354	74.6	36.62	50.3	1.932	0.1497
n-Hexane	0.1323	74.5	36.43	49.56	2.421	0.1486
n-Heptane	0.13	75.5	36.75	50.64	4.788	0.1504
n-Octane	0.1274	76.1	36.98	51.5	9.693	0.151
n-Nonane	0.1257	76.6	37.17	52.24	19.61	0.1504
n-Decane	0.1249	76.8	37.22	52.52	38.89	0.1511
n-Dodecane	0.1249	76.8	37.28	52.55	154.1	0.1509

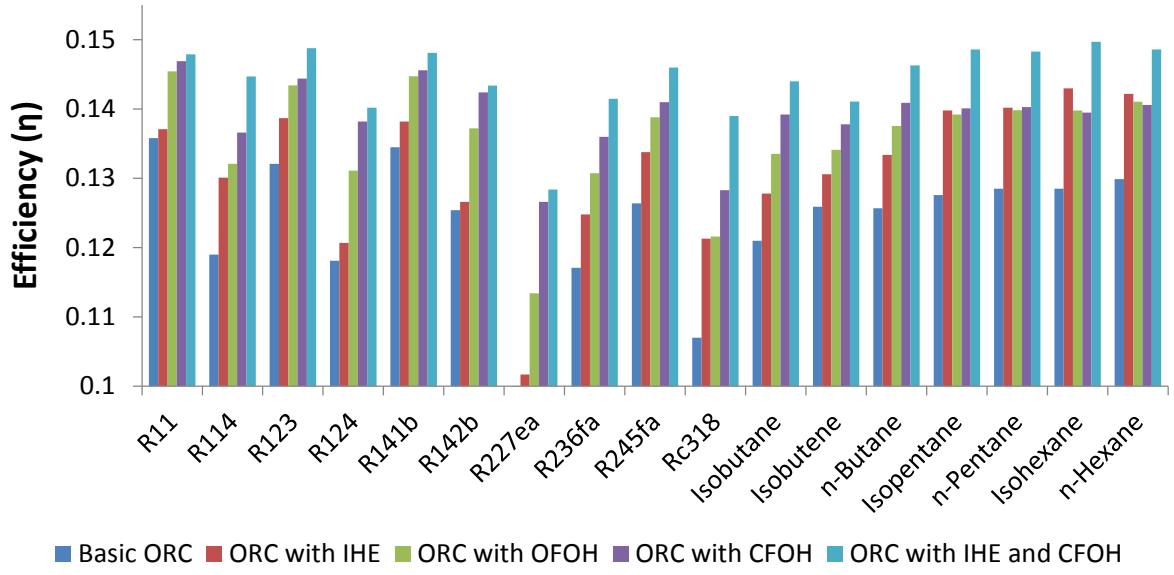

Figure 3.16: Efficiency of acceptable fluids for all configurations

While volumetric flow rate and volume ratio were initially used as a filtering criteria, it is important to further investigate the relationship, if any, between these values and the efficiency. Figure 3.17 shows the relationship between volumetric flow rate and efficiency for the basic ORC cycle and the advanced ORC that utilizes both the IHE and CFOH. Asymptotic behavior can be seen in both cases, with a much stronger presence seen in the advanced cycle. We can conclude that the system being evaluated approaches a maximum possible efficiency where any fluid that produces a higher volumetric flow rate can be expected to have little increase in efficiency. This behavior is expected, since the upper limit that is achievable is the Carnot limit (0.188 for the operating temperatures in this study). The heavy alkanes, not displayed in the figure due to their high volumetric flow rate, further confirm this hypothesis. No such relationship can be found between efficiency and volume ratio, shown in Figure 3.18. A larger range of values can be observed for the basic cycle, while the advanced cycle appears to show a high concentration between values of 0.14 and 0.15 for efficiency.

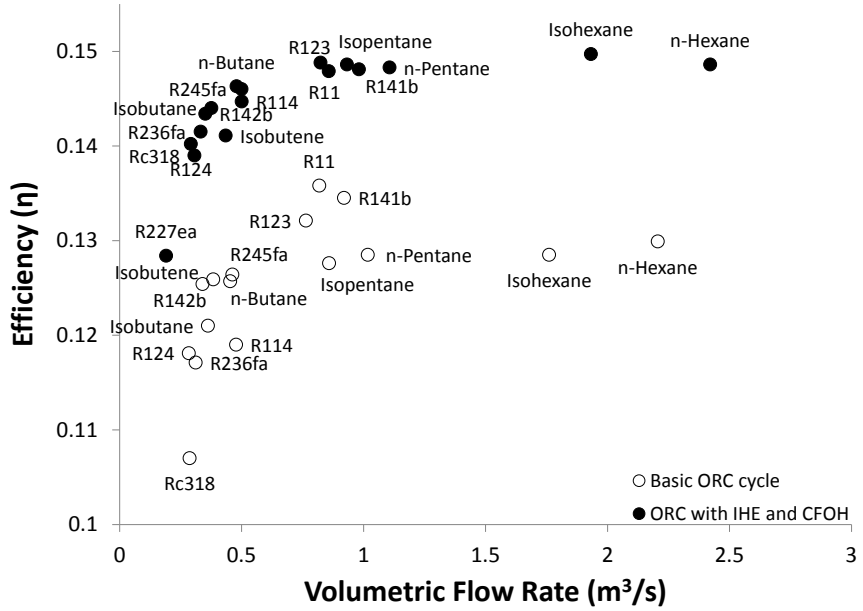

Figure 3.17: Simple and Advanced configurations vs. volumetric flow rate

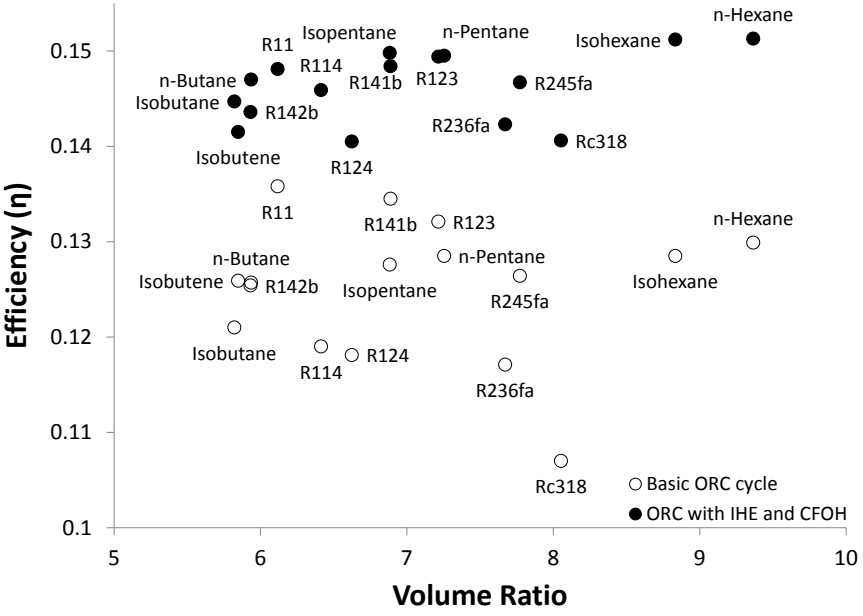

Figure 3.18: Simple and Advanced configurations vs. volume ratio

It is important to evaluate the impact of increased complexity and cost of the system when evaluating the working fluids. The advanced configuration (IHE+CFOH) is the most complex of those evaluated in this study. It would then be expected to have the highest cost associated with it. Several previous studies, mentioned above, have evaluated the simpler IHE configuration. Thus, an evaluation of the relative increase in efficiency was conducted, comparing the advanced configuration to the IHE and simple cycle configurations, shown in Figure 3.19. The range of improvement over the basic ORC varies between 9% and 31%, while the improvement over the IHE configuration is between 4% and 26%. It can be seen that the improvement over the basic configuration is significant. However, for several fluids, the ORC and CFOH configuration is only marginally better than the simpler IHE. Thus, when analyzing system costs, depending on the working fluid, it may be more advantageous to use the IHE configuration. Other factors, discussed below, additionally would influence this decision.

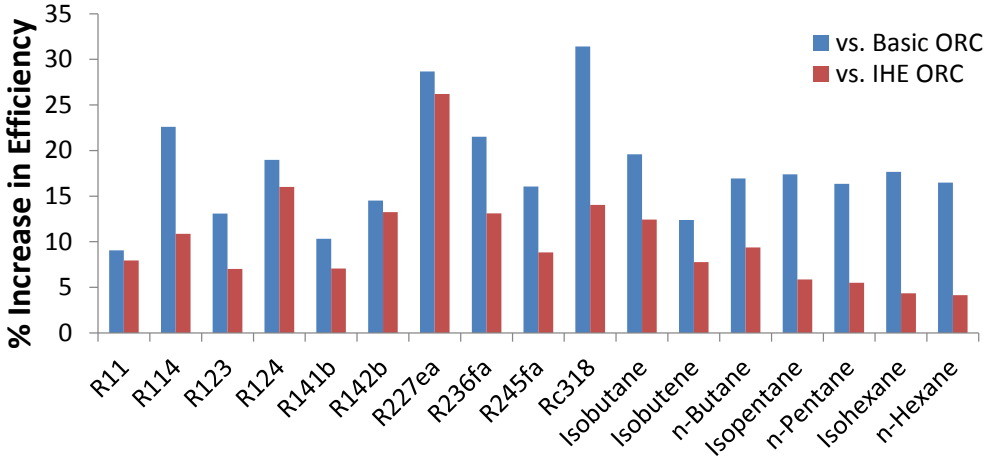

Figure 3.19: Relative increase in performance of advanced ORC vs. simple cycle and IHE configurations

3.5.2 Environmental Impact and Potential Hazards

The concept of sustainable production of solar energy applies to the technologies harvesting this energy. Therefore, if any parts of a design are harmful to the environment in a direct

or indirect way, then the technology itself cannot be deemed truly sustainable. Within the scope of this study, a sustainable design is considered to be one that operates using fluids with low global warming potential (GWP) and ozone depletion potential (ODP). In this way, the ORCs described in the above analysis must be designed using materials with minimal environmental impact. Working fluids in the ORC design that have high ODP and GWP must also be avoided. Direct impact on the environment from the working fluids manifests itself in the toxicity and flammability of the fluids. Fortunately, the refrigerants considered in this study are fairly benign. Additionally, of those examined, only those belonging to the alkane class are flammable [125]. Precautions would be required if operating using alkane refrigerants. While the ORC system is designed to operate at temperatures no higher than 130^oC (further discussed below), varying solar inputs can create potential heat spikes. Safety protocols will need to be implemented to relieve these spikes and prevent high temperatures from occurring locally.

Table 3.5 shows the ODP and GWP metrics for each fluid based on several sources. The alkanes that were examined in this investigation have ODPs of 0 and GWPs below 25, and are thus not included in the table (some other refrigerants, such as R1234ze(E), have similar values and are being used to replace older more environmentally hazardous fluids). It is immediately apparent that R11 and R114 are not feasible due to their ODP of one. Similarly, while R123 and R141b have much lower ODPs, their use is regulated and they would not be recommended. R245fa has an ODP of 0 and a GWP of approximately 1000, which is lower than a significant number of refrigerants. However, it is still nearly two orders of magnitude higher than the alkanes with a comparable or higher efficiency. From these results, it can be seen that alkanes, though flammable, as discussed above, have the highest potential when evaluated on the basis of environmental sustainability and efficiency.

3.5.3 Analysis of Selected Fluids

From the above results, it can be concluded that based on measures of efficiency, volumetric flow rate, volume ratio, and environmental impact, a small group of fluids should be chosen to operate in the ORC in this study: n-Butane, Isopentane, n-Pentane, Isohexane, and n-

Table 3.5: Environmental Properties of Refrigerants

	ODP		GWP (based on 100 year time horizon)						
	40 CFR 82 [126]	Montreal Protocol [127]	FAR IPCC [128]	WMO 2006 [129]	SROC [130]	40 CFR 82 [126]	TAR [131]	WMO 2002 [132]	Other
R11	1	1	4750	4750	4680	4000	4600	4680	
R12	1	1	10900	10890	10720	8500	10600	10720	
R114	1	1	10000	10040		9300	9800	9880	
R123	0.02	0.02	77	77	76	93	120	76	
R124	0.022	0.022	609	609	599	480	620	599	
R134a			1430				1300	1320	
R141b	0.11	0.11	725	725	713	630	700	713	
R142b	0.065	0.065	2310	2310	2270	2000	2400	2270	
R152a			124				120	122	
R161			–	–	–	–	–	–	12 [133]
R227ea			3220				3500	3660	
R236fa			9810				9400	9650	
R245fa			1030				950	1020	
R1234ze(E)			–	–	–	–	–	–	6 [134]
RC318			10300						

Hexane. These can be measured against each other on the basis of efficiency, volume ratio, and volumetric flow rate, since their environmental impact is negligible. Figure 3.20 shows the performance of these working fluids in these categories. It is immediately apparent that there is little variation in performance with respect to efficiency. There is only a 3% range from the lowest value (n-Butane) to the highest (n-Hexane). There is, however, a large increase in volumetric flow rate of 400% from n-Butane to n-Hexane, implying that an expander roughly five times the size would be required for n-Hexane, when compared to n-Butane. Thus, the trade-off between efficiency and cost associated with turbine size is favorable, with little drop in efficiency for a large reduction in size, and therefore cost. Additionally, the volume ratio for n-Hexane is roughly 60% higher than n-Butane. Overall, it can then be concluded that n-Butane is the most suitable working fluid for the application of an ORC utilizing solar energy at a temperature of 100^oC. This analysis compared the performance of the fluids used in the IHE and CFOH configuration. As discussed above, for a certain selected fluid, the simpler IHE configuration is worth considering. In the case of n-Butane, there is approximately a 9.4% increase in performance for the advanced configuration over the IHE configuration. While system costs vary depending on the application, such an increase may be significant enough to justify using the more complex design.

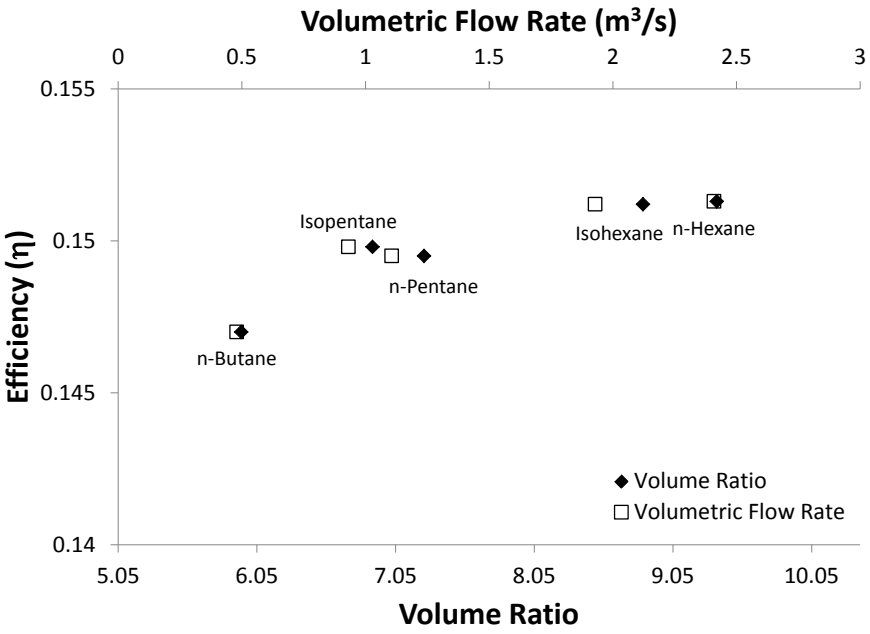

Figure 3.20: Efficiency vs. volume ratio and volumetric flow rate for selected fluids (configuration utilizing IHE and CFOH)

3.6 PERFORMANCE OF OPTIMIZED ORC COMBINED WITH SELECTED PV

3.6.1 Combined Cycle Behavior

The ORCs analyzed in the previous section can operate on heat provided by any heat source. One such source, as discussed above, can be the heat output of concentrated solar PV modules. The values provided by Table 3.1 can be used to calculate the performance of the various cells at a temperature of 110^oC. Assuming a 10^oC temperature drop from the PV module to the operating cycle fluid, the PV module can power the ORC cycle described above. It is then important to evaluate the benefit of such a combined cycle.

It is commonly known that PV cell efficiency decreases with increasing temperature. Thus, there must be a significant increase in performance of the combined PV and ORC system over the basic PV system, particularly one operating at a lower temperature. Figure 3.21 shows the efficiency of the chosen PV cells operating at 25^oC and 110^oC alone and combined with an ORC operating at 110^oC. It can be observed that all cells, with the exception of CdS, show a significant decrease in efficiency from 25^oC to 110^oC. This is offset by the addition of an ORC to the 110^oC case. A solar efficiency of nearly 45% can be achieved through such a combination, when utilizing InGaP/InGaAs/Ge triple-junction cells at 200x concentration.

However, the decrease in performance of the PV cells at a higher temperature is significant enough to offset the increase in performance added by the ORC to a substantial degree for some types of cells. This can be seen more clearly in Figure 3.22, where the benefit of adding the ORC is quantified in terms of efficiency in comparison to the two operating temperature levels of the PV. Evaluating the performance comparison with the 25^oC case, it can be seen that CdS experiences the highest gain ($\sim$12%), with the second highest observed for the triple-junction cells at 200x concentration ($\sim$7%).

This can additionally be evaluated in terms of the increase in performance where the base cases are the PV cells operating alone at the two temperatures. Figure 3.23 shows the percentage increase in performance over the base scenarios. CdS cells clearly show a

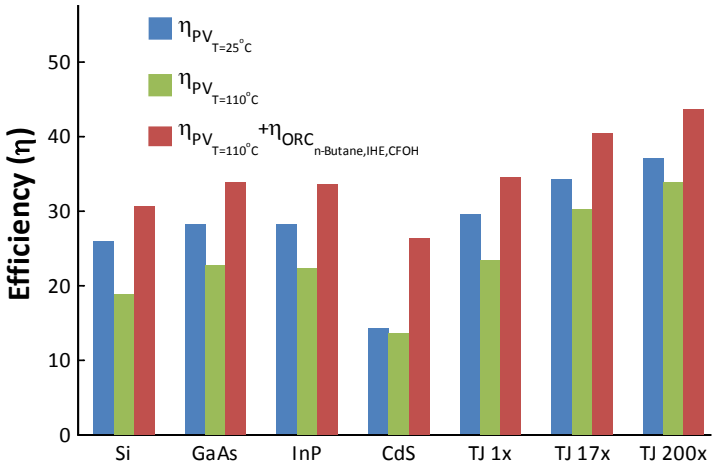

Figure 3.21: Efficiency of various PV cells and combined PV and ORC module. First subscript indicates type of energy conversion (PV or ORC). Second subscript indicates operating temperature for PV and configuration (working fluid, cycle type) for ORC.

substantial benefit from adding an ORC, with a nearly 100% increase over the $25^{o}C$ case, while other types of cells show increases of approximately 20%.

From this analysis, a twofold benefit can be seen from using a combined PV and ORC system. Low efficiency PV cells (CdS) can experience a much larger increase in overall performance, while high efficiency PV cells (TJ 200x) can be a part of very high efficiency systems. Other factors, such as system cost and complexity can impact the choice of the combination used. Concentration using optics can reduce the cost of higher efficiency cells. Additionally, the reduced area exposed to the environment can reduce thermal losses, when the operating temperature is kept constant. Further work in module design and output stabilization due to varying solar inputs is required to determine the optimum combined cycle.

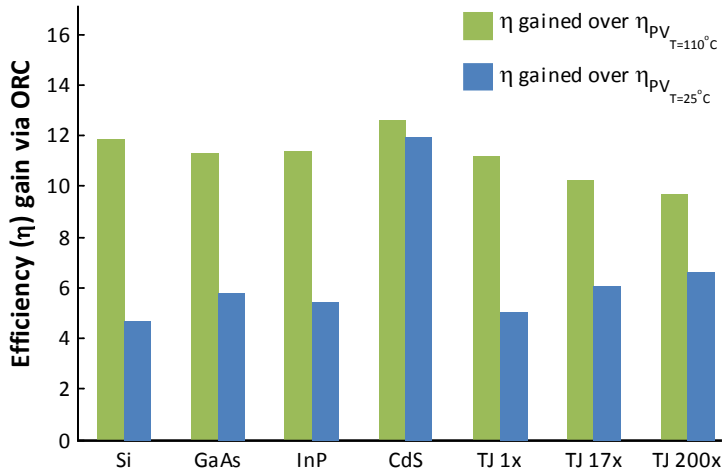

Figure 3.22: Increase in efficiency of combined PV and ORC, compared with efficiency of PV operating alone at the temperature specified in the subscript.

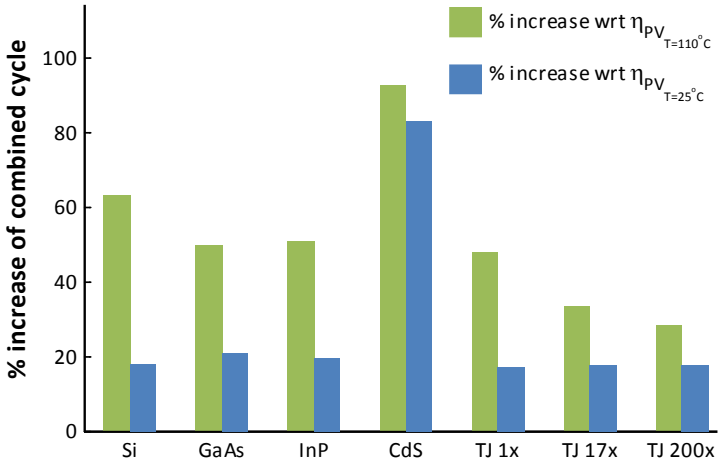

Figure 3.23: Percent increase in performance of combined PV and ORC module over basic PV cases, compared with PV operating alone at the temperature specified in the subscript. (i.e., Percent increase with respect to $\eta_{PV_{T=25^oC}} = [(\eta_{PV_{T=110^oC}} + \eta_{ORC})/\eta_{PV_{T=25^oC}} - 1] \times 100$)

3.6.2 Sensitivity to Temperature

It is important to consider how a system responds to variations in different operating parameters. One such parameter that can be varied is the operating temperature of the PV cells, and therefore the evaporation temperature of the working fluid in the ORC cycle. CdS and TJ 200x PV materials were examined for their variation in performance. The efficiencies of the PV cell, the ORC, and the combination of both were calculated for a temperature range of 80^oC to 130^oC as the ORC heat input temperature (T_1), and are shown in Figures 3.24 and 3.25. Both figures show that there is a marginal increase in overall performance for both cell types, with a somewhat higher increase for CdS cells. As expected, the ORC cycle operates at a higher efficiency for higher temperatures. This is, however, offset by the decreasing performance of the cells at higher temperatures. CdS cells are least affected by increasing temperature and thus show a greater increase in overall performance. It is worth noting that the overall solar efficiency of the triple-junction system crosses 45% at the highest operating temperature.

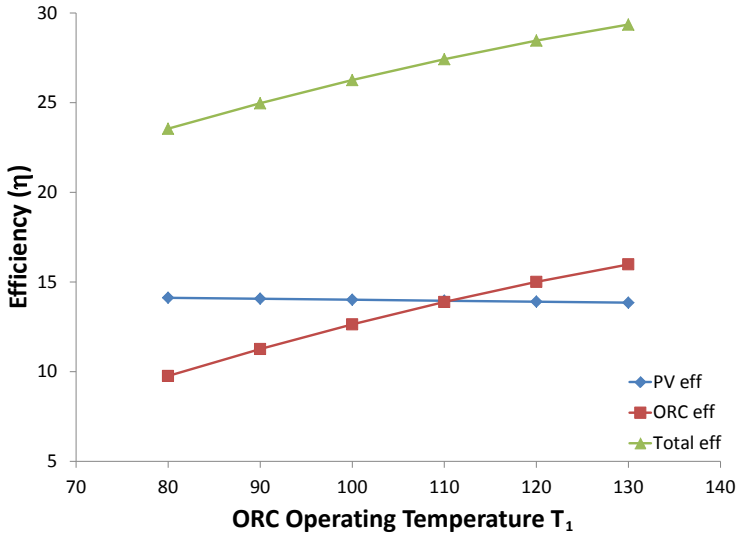

Figure 3.24: Efficiency of the PV cell, ORC, and combination of both for CdS cells at varying T_1.

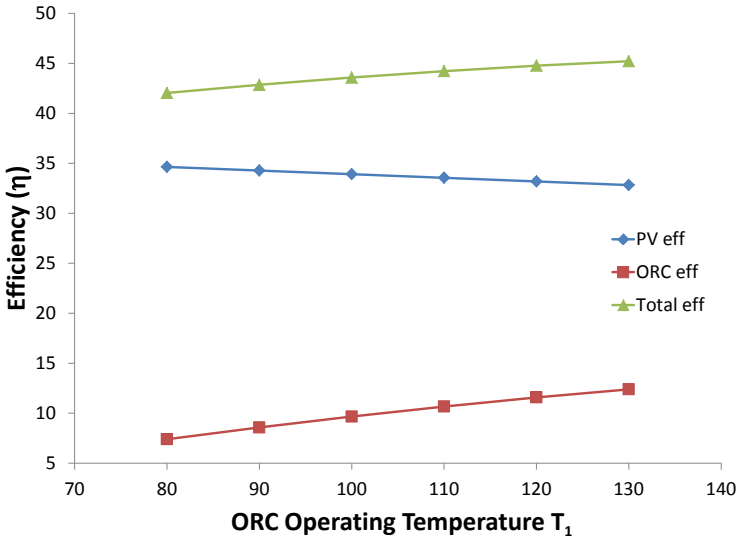

Figure 3.25: Efficiency of the PV cell, ORC, and combination of both for TJ 200x cells at varying T_1.

3.7 CONCLUSION

The feasibility of a combined PVT/ORC system was examined, based on the improvement of the combination in efficiency, compared to the PV cells operating alone. The performance of a variety of fluids as working fluids for the organic Rankine cycle were analyzed for efficiency, volumetric flow rate, volume ratio, and mass flow rate. Five configurations of the ORC were examined: the basic cycle, ORC with an internal heat exchanger (IHE), ORC with an open feed organic fluid heater (OFOH), ORC with a closed feed organic fluid heater (CFOH), and ORC with an internal heat exchanger and a closed feed organic fluid heater (IHE-CFOH). It was found that alkanes (Butane, Pentane, and Hexane), although flammable, performed best in terms of efficiency, while meeting criteria for volumetric flow rate and volume ratio. The advanced configuration using an IHE and a CFOH was found to be the best match for these fluids.

Finally, based on the above parameters, n-Butane was found to have the highest potential for a highly efficient, while economically and environmentally viable, operating fluid. The

optimized ORC was then combined with five types of PV cells to examine the improvement on overall efficiency over operating PV alone. It was found that CdS cells benefit the most from the combination, nearly doubling the overall efficiency. It should be noted that triple-junction cells at high concentration combined with an ORC were able to achieve over 45% solar efficiency.

4.0 NUMERICAL STUDY OF MOLTEN SALT SOLAR BIOMASS GASIFICATION REACTOR

The work above shows that a combination of two renewable energy technologies can produce an overall increase in performance. The overall behavior of the hybrid PV-ORC cycle shows promise for implementation in applications where environmental implications and/or standalone operation is important. Moreover, as our understanding of these hybrid cycles improves, it is possible that they can become more commonly used in a range of applications. However, given the current energy profile in the U.S., and the world, it is also important to examine combinations of renewable energy technologies that can have a more versatile impact, and be integrated with conventional systems. One such combination that has been found to have this potential is a combination of solar thermal energy and biomass gasification.

As previously mentioned, the process of gasification is an endothermic reaction and requires a source of heat. Highly concentrated solar energy at a high temperature is an excellent potential renewable source. This can limit, or entirely eliminate, the need for oxidation to meet the thermal demand, and increase the overall energy density of the product gas. Several solar gasification reactors have been studied and have shown successful operation [49, 50, 135–138]. However, they have drawbacks, one of which is the inconsistency of the incoming solar energy due to cloud cover and the daily solar variation. Thermal storage in the form of molten salt is often used to mitigate this in traditional solar thermal power plants. This is difficult to implement in existing solar gasifiers as they directly expose the biomass to the solar energy in various configurations. An alternative is to use the molten salt itself as the medium that both captures the solar energy and facilitates biomass gasification. Several groups studied the performance of biomass gasification in molten salt, showing that

it is feasible and actually accelerates the process [55, 139, 140]. There are no existing CFD studies, however, of biomass reacting in a liquid salt medium with an external heat source. This work will create an approach and a model that will attempt to predict the results of existing studies of molten salt reactors.

4.1 PREVIOUS CFD STUDIES OF GASIFICATION

Modeling the process of pyrolysis and gasification is incredibly complex. Thus, many CFD studies limit their focus to one or only a few aspects of the process. All gasifiers contain an interaction of two media: the biomass in solid form and the gas that reacts with the biomass to produce gaseous products. The biomass can be mixed with a solid, or in some cases, a liquid, with the reactor operating as a fluidized bed or a bubble column, respectively. In both cases, both phase combinations, gas-solid and gas-liquid, must be modeled using a CFD model. In certain applications, each phase can be treated as continuous, and a Eulerian framework can be utilized. In a series of studies that utilized this framework, Papadikis et al. studied pyrolysis in a fluidized bed reactor in three parts, with the first study examining momentum transport [53], the second study focusing on heat, momentum, and mass [52], and the third on the effect of biomass shrinkage [54]. Their model utilized a continuous model for both the solid and the gas, while using a customized function to describe the Lagrangian behavior of a biomass particle undergoing pyrolysis. Another study by Xue and Fox focused on modeling pyrolysis of biomass in a fluidized bed reactor [141]. Their group used the findings of this study to then create a CFD model for a fluidized bed gasifier using a Eulerian framework and coupling the transport equations with chemical kinetic models to describe the process of biomass pyrolysis and subsequent gasification [142].

While the above studies used a Euler-Euler model to describe the two phases interacting, some groups chose to use a more complex and computationally intensive Euler-Lagrange approach [143, 144]. This approach models individual particles or bubbles and their interaction with a continuous medium, either gas or liquid. Ku et al. used this approach to model a fluidized bed reactor using the Eulerian model for the gas phase and a discrete element

method (DEM) for the biomass and sand particles [144]. A similar methodology may be used to track individual bubble evolution in a bubble column. Darmana et al. utilized this discrete bubble model (DBM) to create a three-dimensional model of a bubble column and study hydrodynamics, mass transfer, and chemical reactions [145].

A somewhat different approach to modeling pyrolysis and gasification was taken by Hathaway et al., where their group modeled a single cellulose tablet that underwent pyrolysis [55]. They used experimental data to calibrate their model to accurately predict reaction rates for both pyrolysis and gasification in a contained reactor.

4.2 SOLAR GASIFIER DESIGNS

There are many varying ideas for optimizing the use of concentrated solar energy to gasify biomass. Several designs that have been proposed are the packed bed [135], fluidized bed [136], entrained flow [137], and drop-tube [138], the diagrams for each shown in Figures 4.1-4.4. The packed bed design consists of solar radiation entering through a window focused on the biomass, heating it to undergo a reaction. Fresh material replaces the old material as it collapses. The fluidized bed design features a column on which sunlight is focused, inside of which jets of steam and inert gas fluidize the flow, facilitating heat transfer and reaction. The entrained flow gasifier operates using circulating jets that create a vortex for biomass particles to travel along. The drop tube design consists of an array of tubes inside of a cavity receiver with feedstock being delivered from the top.

A novel design for a solar gasifier was proposed and examined by Hathaway et al. [49, 50, 146], operating using molten salt as a medium to capture solar energy from a cavity receiver and transfer it to the biomass being gasified directly within the molten salt. As shown in Figure 4.5, the molten salt region was designed to surround the cavity receiver, absorbing heat and driving the gasification reaction, as biomass is injected from the bottom of the of the reactor along with the gas.

There has additionally been interest in modeling the drop-tube design. Several studies have been carried out using CFD modeling of a cavity receiver with vertical absorber tubes

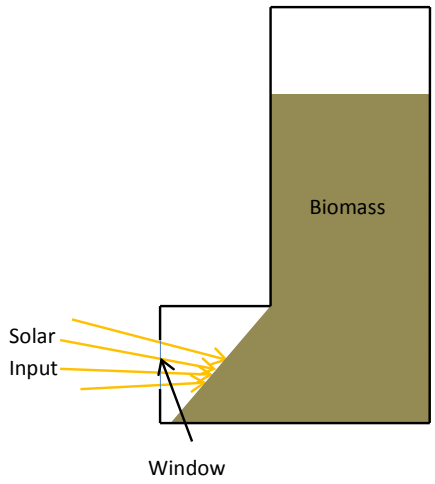

Figure 4.1: Packed bed solar gasifier diagram

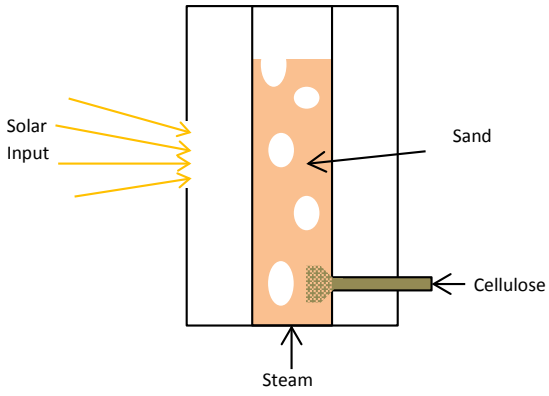

Figure 4.2: Fluidized bed solar gasifier diagram

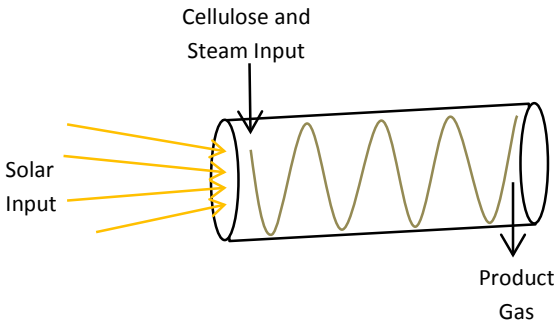

Figure 4.3: Entrained flow gasifier

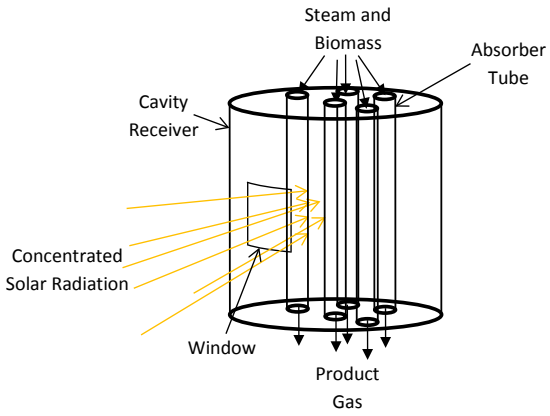

Figure 4.4: Drop-tube solar gasifier diagram

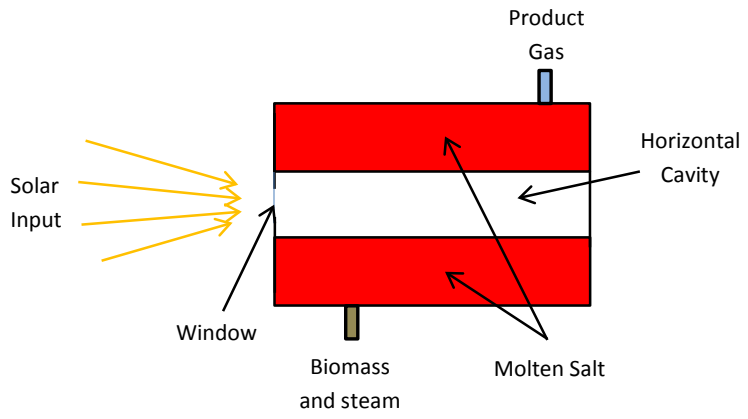

Figure 4.5: Molten salt biomass gasifier diagram

[147–151]. These have focused on improving the original design by studying the various factors that influence performance, including the tube diameter, cavity diameter, performance of a reflective receiver compared to an absorbing receiver, and several others. Several results from these investigations on the heat flux impeding on the absorber tubes are used in this study.

4.3 MATHEMATICAL MODEL

As stated above, there are no existing models for examining pyrolysis and gasification in a molten salt reactor. This work will create a model using ANSYS software, using the findings in the CFD studies described above to attempt to emulate results from experimental pyrolysis and gasification studies in molten salt.

The process of gasification in molten salt involves three phases: solid, liquid, and gas, that are exchanging momentum, temperature, and species. This is a complex problem, which will require several simplifications. The first simplification is based on how the fluid interaction is modeled. A Euler-Euler approach models phases as continuous at various concentrations, while a Euler-Lagrange approach can model boundaries between the phases,

such as individual bubbles and the surrounding liquid. The current work will operate using a Euler-Euler (also known as two-fluid) approach due to the complexity of the reactions being modeled. While the biomass enters the reactor as a solid, it quickly breaks down via the pyrolysis reaction. The remaining char particles are assumed to be small enough to disperse in the liquid and behave as a continuous phase mixed with the molten salt. Thus, the first model will feature two interacting phases, each composed of several species.

Turbulence models vary in their complexity and ability to match results in experimental measurements. The renormalization group theory (RNG) $k - \epsilon$ model has been found to adequately predict turbulent viscosity in bubble plumes and has been used extensively in literature [152–155]. The model was chosen to be three-dimensional. Studies have shown that a three-dimensional model is required for bubble plumes that undergo oscillations [156]. Both pyrolysis and gasification are endothermic reactions that require an external heat source or an additional exothermic reaction. This is modeled using the energy equation, with a simulated heat source present in the cavity receiver model to simulate realistic operation of both the heat source and the heat sink occurring within the reactor. Several complex bubble size models that account for coalescence and breakup have been proposed and examined [152, 157, 158]. While these are of great interest for future work, a single bubble diameter was utilized for this study, as the focus is on the chemical and thermal behavior of the gasifier. Bubble diameter was estimated based on experimental findings of Sada et al. for varying liquids, including some molten salts at raised temperatures [159]. These were later verified in other studies focused on molten salt oxidation reactors [160, 161]. An initial model of a square column was created. There have been several experimental and numerical studies on a cylindrical column design, which can validate the results of the hydrodynamic behavior [153, 162–164]. Gas hold-up, bubble velocity and other factors will be examined in the solution of the numerical model and validated against results found in experimental studies. The physical model consists of several equations describing the individual properties. This behavior is described in the following subsection.

4.3.1 Modeling Hydrodynamics

The governing equation for continuity in multiphase flow is:

$$\frac{\partial}{\partial t}(\alpha_q \rho_q) + \nabla \cdot (\alpha_q \rho_q \vec{v}_q) = \sum_{p=1}^{n} (\dot{m}_{pq} - \dot{m}_{qp}) + S_q \tag{4.1}$$

where for a phase q, α_q denotes the volume fraction, ρ_q denotes the density, $\vec{v}_q$ denotes velocity, and $\dot{m}_{pq}$ denotes the mass transfer from phase p to phase q, while $\dot{m}_{qp}$ characterizes the opposite. Finally, S_q accounts for any source terms present. The continuity is followed by the momentum description, as shown:

$$\begin{aligned}\frac{\partial}{\partial t}(\alpha_q \rho_q \vec{v}_q) + \nabla \cdot (\alpha_q \rho_q \vec{v}_q \vec{v}_q) = -\alpha_q \nabla p + \nabla \cdot \bar{\bar{\tau}}_q + \alpha_q \rho_q \vec{g} \\ + \sum_{p=1}^{n} (\vec{R}_{pq} + \dot{m}_{pq} \vec{v}_{pq} - \dot{m}_{qp} \vec{v}_{qp}) + (\vec{F}_q + \vec{F}_{lift,q} + \vec{F}_{wl,q} + \vec{F}_{vm,q} + \vec{F}_{td,q})\end{aligned} \tag{4.2}$$

where $\vec{v}_{qp}$ is the interphase velocity, $\vec{F}_q$ is an external body force, $\vec{F}_{lift,q}$ is a lift force, $\vec{F}_{vm,q}$ is a virtual mass force, $\vec{F}_{wl,q}$ is a wall lubrication force, $\vec{F}_{td,q}$ is a turbulent dispersion force, and $\vec{R}_{pq}$ is an interaction force between phases. The term $\vec{R}_{pq}$ is described using the interphase momentum exchange coefficient K_{pq}, as follows:

$$\sum_{p=1}^{n} \vec{R}_{pq} = \sum_{p=1}^{n} K_{pq} (\vec{v}_p - \vec{v}_q) \tag{4.3}$$

where K_{pq} is defined by:

$$K_{pq} = \frac{\rho_p f}{6 \tau_p} d_p A_i \tag{4.4}$$

and where A_i is the interfacial area, f is the drag function and is dependent on the drag coefficient C_D, and τ_p is defined as:

$$\tau_p = \frac{\rho_p d_p^2}{18 \mu_q} \tag{4.5}$$

There are numerous expressions for the drag coefficient, C_D. The effect of these has been extensively examined in previous studies. For the current investigation, the Tomiyama et al. model is utilized, expressed as follows [165]:

$$f = \frac{C_D Re}{24} \tag{4.6}$$

$$Re = \frac{\rho_q |\vec{v}_p - \vec{v}_q| d_p}{\mu_q} \tag{4.7}$$

$$C_D = max\left(min\left(\frac{24}{Re}(1 + 0.15Re^{0.687}), \frac{72}{Re}\right), \frac{8}{3}\frac{Eo}{Eo+4}\right) \tag{4.8}$$

$$Eo = \frac{g(\rho_q - \rho_p)d_p^2}{\sigma} \tag{4.9}$$

The lift force is defined as a force exerted on the secondary phase by velocity gradients in the primary phase, and can be found as follows:

$$\vec{F}_{lift} = -C_L \rho_q \alpha_p (\vec{v}_q - \vec{v}_p) \times (\nabla \times \vec{v}_q) \tag{4.10}$$

where C_L is the lift coefficient, and similar to the drag coefficient, has been described using several models[166–168]. For this investigation, it has been defined by a constant value:

$$C_L = 0.5 \tag{4.11}$$

This definition has been thoroughly examined by other authors and shown to produce good results [162, 169, 170]. The virtual mass force is defined as the inertia of the primary phase reacting to an acceleration experienced by the secondary phase in relation to the primary phase. This force is quantified as shown:

$$\vec{F}_{vm} = 0.5\alpha_p \rho_q \left(\frac{d_q \vec{v}_q}{dt} - \frac{d_p \vec{v}_p}{dt}\right) \tag{4.12}$$

While the effect of other forces has been studied elsewhere, they are currently neglected in this model, due to numerical instabilities caused by the interaction with the chemical reaction models. Several physical parameters highly impact the hydrodynamic behavior. The molten salt blend that was simulated in this study is based on that used in the experimental study conducted by Hathaway et al. [55]. The properties of the blend are summarized in Table 4.1.

Table 4.1: Property values of molten salt blend

Property	Value
Density	$1680\frac{kg}{m^3}$
Viscosity	$0.00206\frac{kg}{m-s}$
Surface tension	$0.208\frac{N}{m}$
Thermal conductivity	$0.75\frac{W}{m-K}$
Specific heat capacity	$1842\frac{J}{kg-K}$

Since each phase consists of several species, they must additionally be accounted for as follows:

$$\frac{\partial}{\partial t}(\alpha_q \rho_q Y_q^i) + \nabla \cdot (\alpha_q \rho_q \vec{v}_q Y_q^i) = -\nabla \cdot \alpha_q \vec{J}_q^i + \alpha_q R_q^i + \alpha_q S_q^i + \sum_{p=1}^{n} (\dot{m}_{p^i q^j} - \dot{m}_{q^j p^i}) + R \quad (4.13)$$

where Y_q^i is the local mass fraction of the species of the phase q, R_q^i is the net rate of production of homogeneous species, S_q^i is the rate of creation by addition from the dispersed phase, $\dot{m}_{p^i q^j}$ is the mass transfer source between species i and j from phase q to p, and R accounts for the heterogeneous reaction rate. As mentioned above, a turbulence model is necessary to properly describe the behavior of the bubble plume. Here, the RNG mixture turbulence model describes the behavior:

$$\frac{\partial}{\partial t}(\rho_m k) + \nabla \cdot (\rho_m \vec{v}_m k) = \nabla \cdot \left(\frac{\mu_{t,m}}{\sigma_k} \nabla k \right) + G_{k,m} - \rho_m \epsilon \quad (4.14)$$

$$\frac{\partial}{\partial t}(\rho_m \epsilon) + \nabla \cdot (\rho_m \vec{v}_m \epsilon) = \nabla \cdot \left(\frac{\mu_{t,m}}{\sigma_\epsilon} \nabla \epsilon \right) + \frac{\epsilon}{k}(C_{1\epsilon} G_{k,m} - C_{2\epsilon} \rho_m \epsilon) \quad (4.15)$$

where the turbulent viscosity is:

$$\mu_{t,m} = \rho_m C_\mu \frac{k^2}{\epsilon} \quad (4.16)$$

The term $G_{k,m}$ denotes the production of turbulence kinetic energy, and can be found as shown:

$$G_{k,m} = \mu_{t,m}(\nabla \vec{v}_m + (\nabla \vec{v}_m)^T) : \nabla \vec{v}_m \tag{4.17}$$

Inter-phase drag is an important property to consider when modeling multiphase flows. The inter-phase drag coefficient accounts for this phenomenon.

For models considering a chemical reaction, it is necessary to account for energy transfer. The conservation of energy equation is used for this in the following form:

$$\frac{\partial}{\partial t}(\alpha_q \rho_q h_q) + \nabla \cdot (\alpha_q \rho_q \vec{u}_q h_q) = \alpha_q \frac{\partial p_q}{\partial t} + \overline{\overline{\tau}}_q : \nabla \vec{u}_q - \nabla \cdot \vec{q}_q + S_q + \sum_{p=1}^{n} (Q_{pq} + \dot{m}_{pq} h_{pq} - \dot{m}_{qp} h_{qp}) \tag{4.18}$$

where for phase q, h_q is the specific enthalpy, $\vec{q}_q$ is the heat flux, S_q is a source term that accounts for sources like chemical reaction, Q_{pq} is the intensity of heat exchange between phases p and q, and h_{pq} is the interphase enthalpy.

4.3.2 Modeling Reaction Kinetics

As discussed in the findings of existing literature, the chemical reactions in a gasification reactor are numerous and complex [52, 53, 141, 171]. Several homogeneous and heterogeneous chemical reactions occur at varying kinetic rates. Chen et al. presented a detailed chemical model for the pyrolysis and gasification of wood [172]. Their model consisted of three processes: pyrolysis into gas, char, tar; char gasification via heterogeneous reactions; and homogeneous reactions within the gas phase. The current model implements a similar technique, with a simplification based on the assumption that tar production is assumed to be minimal, based on the findings of the molten salt experiments of Hathaway et al. [139]. Thus, the predicted resulting pyrolysis products are as follows:

$$biomass \begin{cases} \rightarrow & \text{pyrolysis gas products}(CO, CO_2, H_2, H_2O, CH_4) \\ \rightarrow & \text{char}(C_s) \end{cases}$$

The composition of the devolatilization products can be estimated based on the proximate and ultimate analysis of the biomass. The conversion to char is set to the proximate analysis

of fixed carbon, similar to other pyrolysis simulation studies [171, 173–175]. The volatile gas composition can be partially estimated based on a stoichiometic analysis, derived from the ultimate analysis. This provides three equations, leaving two to be determined based on emperical findings. The first equation can be estimated based on a ratio of CO to CO_2 in the pyrolysis products [55] The second equation is based on estimating H_2O composition. This reaction model, shown below, is implemented in the CFD cylindrical column model. The resulting gas composition will be compared against the findings of Hathaway et al. for a molten salt reactor [55, 139].

$$C_s + H_2O \rightarrow CO + H_2 \tag{4.19}$$

$$C_s + CO_2 \rightarrow CO \tag{4.20}$$

$$CH_4 + H_2O \rightarrow CO + 3H_2 \tag{4.21}$$

$$CO + H_2O \leftrightarrow CO_2 + H_2 \tag{4.22}$$

The rates for these reactions are based on previous empirical studies, with devolatilization and steam gasification based on experimental findings of Hathaway et al.[55], while the other reactions are based on previous studies of CFD modelling of gasification [171, 173–175]. Table 4.2 lists the activation energy, pre-exponential factor, and concentration coefficients. These values are used to find the rate constant based on the Arrhenius equation:

$$k_{f,r} = A_r T^{\beta_r} exp(\frac{-E_r}{RT}) \tag{4.23}$$

where A_r is the pre-exponential factor, β_r is a temperature exponent (zero for the reactions being considered), E_r is the activation energy ($\frac{J}{kgmol}$), and R is the universal gas constant ($\frac{J}{kgmol-K}$). It is important to note that the water-gas shift reaction (5.3) is reversible, and can be calculated using either a forward and a backward Arrhenius rate, or using an equilibrium constant, based on Gibbs free energy. The former was chosen for this study, with the subscripts f and b denoting the forward and backward rates, respectively.

Table 4.2: Gasifier sub-system state properties

Reaction	A_r	E_r	Rate of Reaction	Reference
Devolatilization	1.15e9	2.38e8	$R_{devol} = k_{devol}[C_{biomass}]$	[55]
(4.19)	2.5e4	1.58e8	$R_{4.19} = k_{4.19}[C_{c_s}]^{\frac{2}{3}}[C_{H_2O}]^{\frac{2}{3}}$	[55]
(4.20)	4.364	2.48e8	$R_{4.20} = k_{4.20}[C_{CO_2}]$	[174]
(4.21)	3e-3	1.25e8	$R_{4.21} = k_{4.21}[C_{CH_4}][C_{H_2O}]$	[174]
$(5.3)_f$	2.78e3	1.26e7	$R_{5.3_f} = k_{5.3_f}[C_{CO}][C_{H_2O}]$	[171, 173, 174]
$(5.3)_b$	1.02e5	4.55e7	$R_{5.3_b} = k_{5.3_b}[C_{CO_2}][C_{H_2}]$	[171, 173, 174]

4.4 PRELIMINARY STUDY: VERIFICATION OF WATER-AIR AND MOLTEN SALT-STEAM BEHAVIOR

In order to verify the behavior of the model in Fluent, a preliminary study was conducted to examine and compare several closures for interphase forces. A square column was examined with dimensions (height=45cm, width=15cm, depth=15cm) and mesh parameters (46,080 cells) based on a previous study conducted by Masood et al. [169]. The inlet was designated with an 8x8 grid and a constant velocity, determined by the requirement of the superficial gas velocity to be 0.0049m/s. The outlet boundary condition was set to degassing. These parameters correspond to those used by Deen in a PIV experiment on a square bubble column [176].

The goal of this preliminary study is to examine the predicted behavior of a molten salt-steam bubble column and compare the results to the behavior predicted for a water-air column. For ease of comparison, several drag closures were examined for the water-air column: Schiller-Naumann, Grace, and Tomiyama. A constant lift coefficient of $C_L = 0.5$ was used for all models. Since a square water-air column has previously been studied, the results of the current model function as a reference to compare against those for the molten column. It is worth noting that the water-air results showed strong agreement with those of the study carried out by Masood et al. [169]. Axial liquid and gas velocities were examined at various heights in the column with the results averaged over a period 100 seconds of

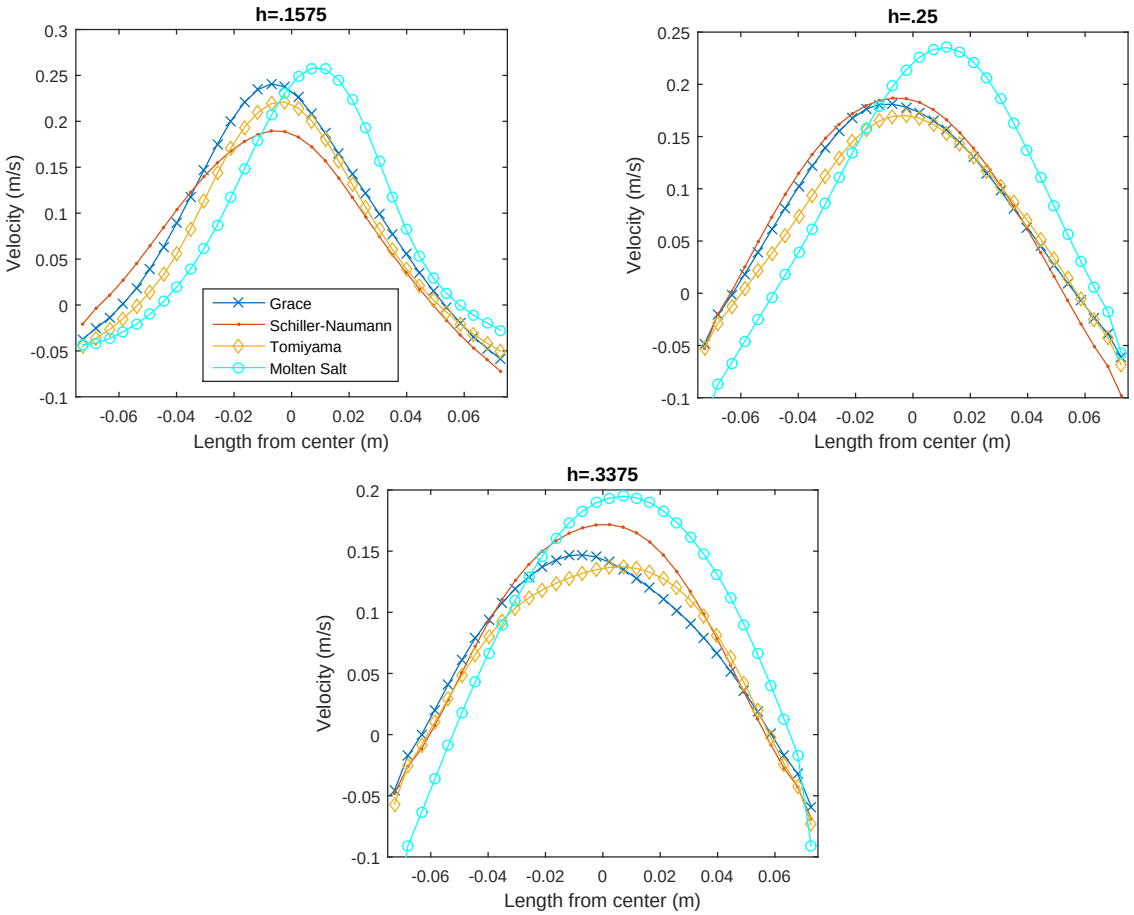

Figure 4.6: Axial liquid velocity profile at each specified height

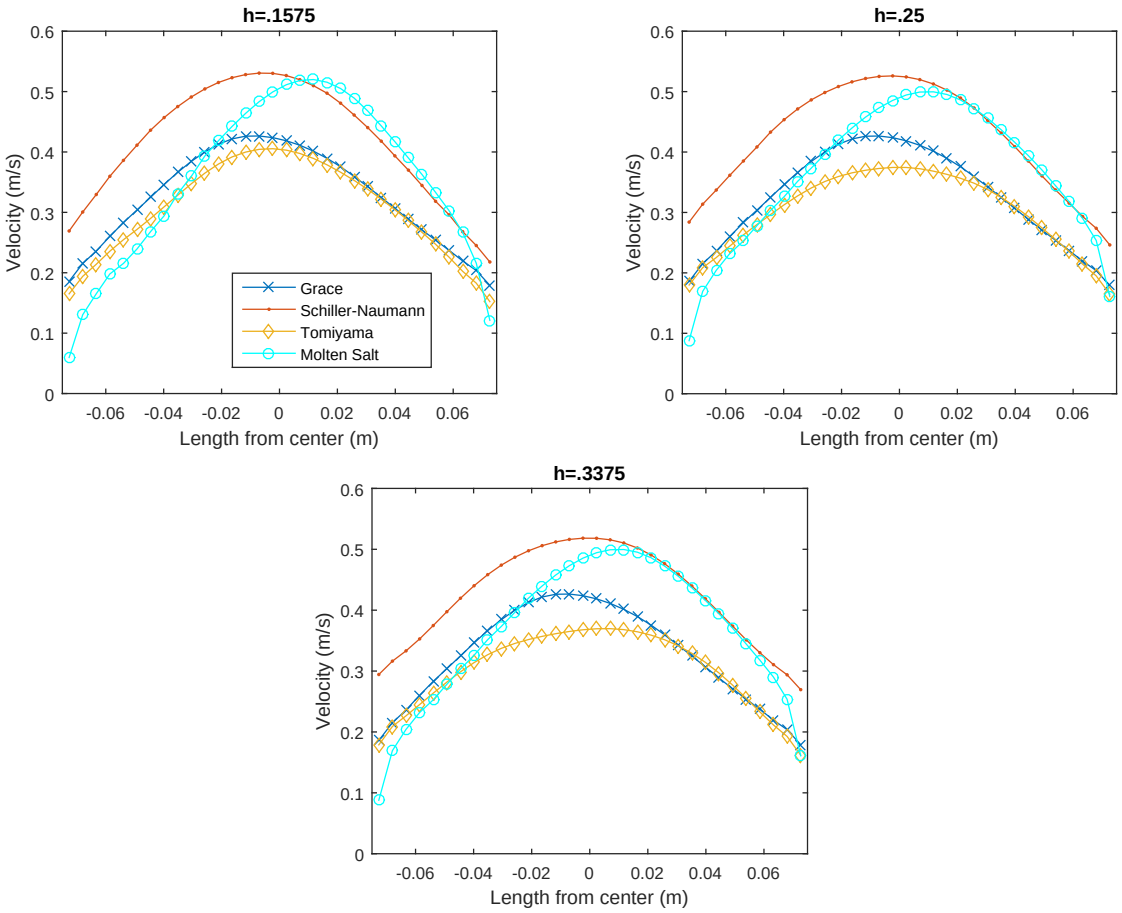

Figure 4.7: Axial gas velocity profile at each specified height

simulation time. Figure 4.6 shows the liquid velocities at each specified height while Figure 4.7 shows the gas velocities. A key observation can be made based on the above results in that the behavior of each type of gas-liquid mixture is similar in magnitude and shape. The liquid velocity for the molten salt maintains a higher peak at each measured height than any of the predicted peaks for the water-air column. This correlates with the relatively high peaks for the gas velocity as well, though not as sharply defined. These results demonstrate that the behavior of the molten salt-steam column is expected to be comparable to that of a water-air column, allowing for further investigations.

4.5 PHYSICAL MODEL

Several important factors influence the design of the computational domain and the conditions for operation. The computational domain is designed to simulate an absorber tube that is present inside a cavity receiver, as shown in the diagram in Figure 4.8. The absorber is modeled as a cylinder with a diameter of $15cm$ and a height of $60cm$, roughly proportional to the tubes used in the study by Martinek et al.[150]. The larger size has been chosen due to a larger body of CFD literature associated with bubble columns of similar size [153, 162–164]. A cavity receiver can be designed with one or several absorber tubes, which dictates the amount of heat that each will receive, compared to the total that will be entering the cavity. For this investigation, a heat input of $5kW$ is assumed, with a non-uniform heat flux, modeled using the results of the investigation of Martinek et al. [147]. The top and bottom of the receiver are assumed to be insulated, and one side of the cylinder is assumed to receive zero flux. The side facing the solar input is assumed to experience a peak in the center of the receiver with respect to height and angle of position, and decrease parabolically with respect to the angle around the horizontal plane of the cylinder and the cylinder height. This profile is shown in the CFD model in Figure 4.9.

There is little data on the behavior of gases in high temperature molten salt bubble columns. As such, an estimate for the bubble diameter was required. A study by Sada et al. provides a general formula for finding bubble diameter based on fluid properties [159].

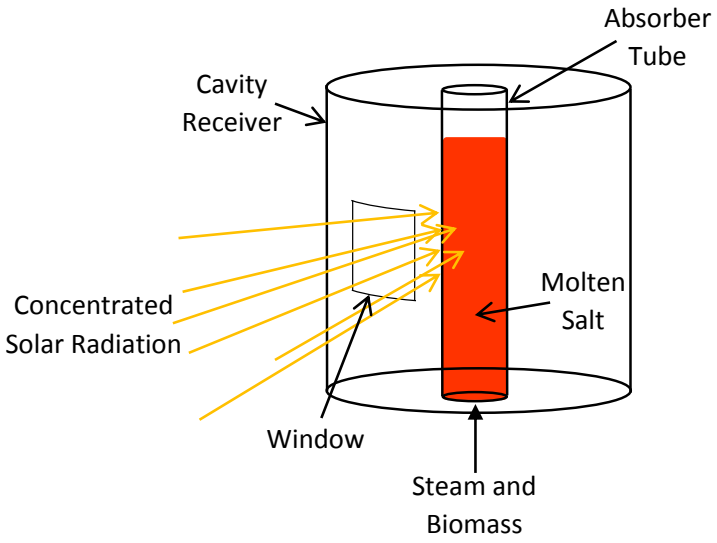

Figure 4.8: Vertical cavity receiver and absorber diagram

A more recent investigation for chloride salts at a lower temperature reported diameters of $0.263cm$ to $0.407cm$. Based on these works, an estimate for a bubble diameter of $0.4cm$ was chosen. A mass flow boundary condition was applied to a region in the bottom of the column, while the outlet boundary was set at the top of the column with a degassing condition. The fluid domain is a non-uniform mesh, displayed in Figure 4.10, consisting of $52,800$ elements. Due to the large computational time requirement for attempting to achieve chemical equilibrium, finer meshes were not attempted. However, the order of magnitude of the number of elements used in this study is similar to that in other similar investigations [153, 162, 169]. The solution was solved using in a transient phase-coupled SIMPLE scheme for the pressure-velocity coupling, with time steps of 0.005 seconds and first order implicit time stepping.

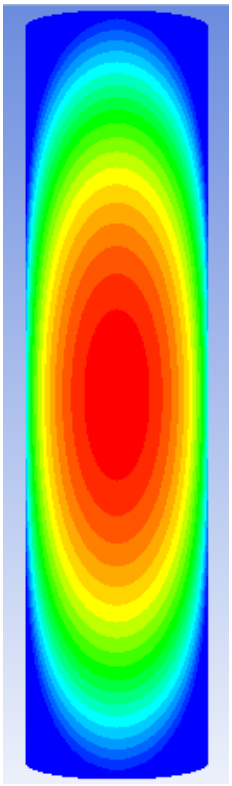

Figure 4.9: Heat flux profile for absorber

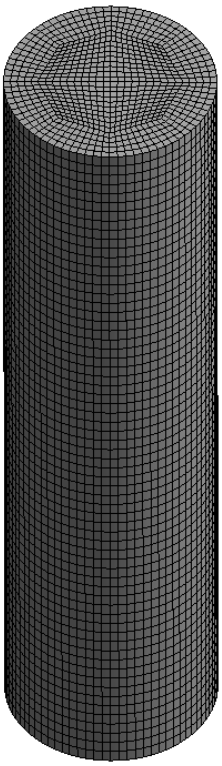

Figure 4.10: Meshed computational domain

4.6 RESULTS OF CFD MODEL

Two investigations were carried out for the computational model: a non-reacting column with molten salt as the primary phase and steam as the secondary phase to obtain an average flow profile. The second investigation utilized the same domain to simulate a reacting column with a heat flux distribution totaling 5kW, and a biomass and steam input corresponding to the required flow rates to achieve steady state.

4.6.1 Non-reacting column

The required steam input can be calculated based on the total heat input and the content of the biomass fuel. It is assumed that the biomass enters the gasifier after having undergone a drying process, where there is a negligible amount of moisture present. The temperature of the dried biomass is set to $400K$, or just above the evaporating point of water. The steam is assumed to be preheated to a temperature of $1050K$ using gases leaving the gasifier. The power plant analysis described in Chapter 5 confirms that these numbers are within the achievable performance of the system. Cellulose has a heat capacity of approximately $1400J/kg-K$, while steam has a heat capacity of $2436J/kg-K$. The pyrolysis reaction described above has a heat of reaction of $146.8kJ/mol$, and produces 1.752 moles carbon char to 1 mole cellulose. The gasification reaction has a heat of reaction of $131kJ/mol$. From this data, an input rate of cellulose and the demand of steam for the gasification reaction can be calculated. Given the above calculations, a stoichiometric amount of steam would require a flow rate of $1.2e^{-4}kg/s$.

To establish hydrodynamic behavior, no reaction was assumed to occur in the first simulation. The simulation was operated over a period of 140 seconds, with the the initial 40 seconds allowing for the column to achieve steady state behavior, as has been done in other studies [153, 162, 169], after which the average velocity, volume fraction, and turbulent kinetic energy were recorded. Figure 4.11 shows a snapshot of an instantaneous velocity profile for a vertical plane through the column, along with several horizontal planes, while Figure 4.12 shows the average liquid velocity. These profiles can be compared to those found in

studies by Akhtar et al.[177], where significant turbulent behavior occurs near the inlet area and acquires a uniform pattern as the gas phase approaches the outlet. Figures 4.13 and 4.14 show the instantaneous and average volume fraction profiles, respectively. The high rate of circulation observed in the velocity profile can be seen as represented in the behavior of the bubble plume. The plume can be seen to disperse with column height, achieving a more uniform pattern when approaching the outlet. The instantaneous turbulent kinetic energy was also recorded, and is shown in Figure 4.15. High velocity gradients near the inlet were expected to produce an increase in the kinetic energy, which can be observed. This decreases as the plume rises, which coincides with lower velocity magnitude and gradient.

4.6.2 Reacting column

With the dynamics for a non-reacting plume in the column established, the behavior of the reacting column now can be identified. The inlet of the column was modified to have a center portion where biomass would be introduced, while a ring surrounding the center would introduce the steam. A longer time is expected for the reacting column to achieve steady state operation, due to the slower reaction rates. To mediate this, the column was initialized with a low amount of carbon char to stabilize the gasification reaction and 100 seconds of simulation time was carried out before averaging data. Several parameters are important in evaluating the performance of the reacting column. The presence of reactions is expected to alter the hydrodynamic behavior, which is shown in Figure 4.16 for the liquid velocity, Figure 4.17 for the gas holdup, and Figure 4.18 for the turbulent kinetic energy. The most apparent change can be seen in the gas holdup, where the presence of the pyrolysis and gasification reactions causes a large amount of gas to be created within the volume and travel up the plume. The parameters of importance associated with chemical reactions in the simulation are the rates of pyrolysis, gasification, and water-gas shift; the temperature; and the composition of the gas leaving the reacting column. Figures 4.19, 4.20, and 4.21 show the respective reaction rates for these reactions. It was found that other reactions used in the model occurred at rates several magnitudes less than the above reactions and thus are not shown. The liquid temperature is shown in Figure 4.22.

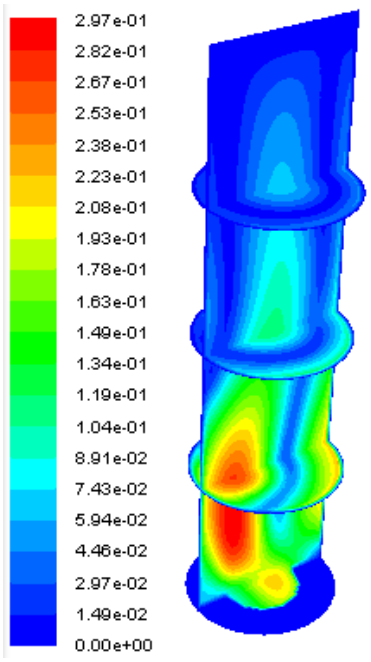

Figure 4.11: Instantaneous liquid velocity $[m/s]$

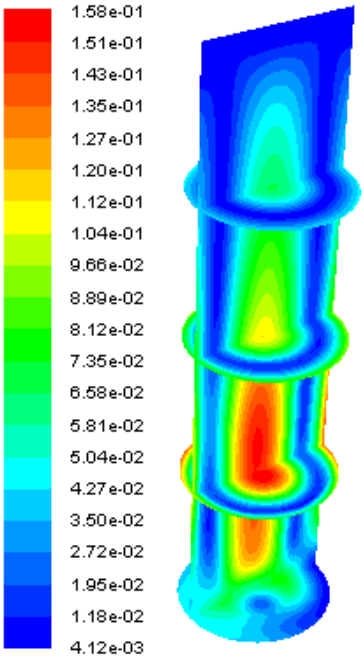

Figure 4.12: Average liquid velocity $[m/s]$

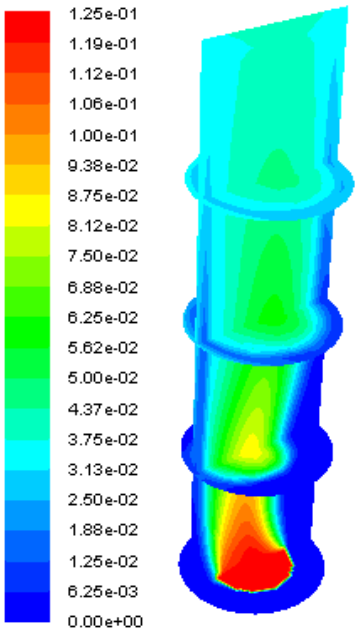

Figure 4.13: Instantaneous volume fraction

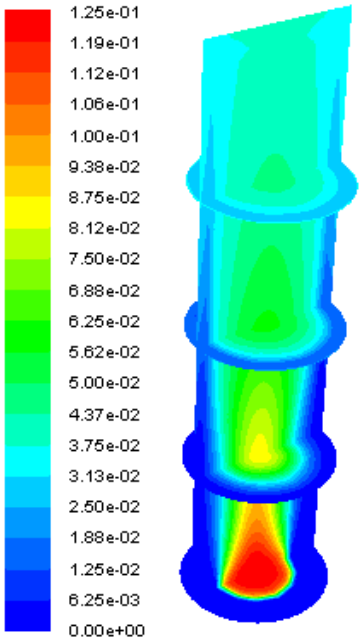

Figure 4.14: Average volume fraction

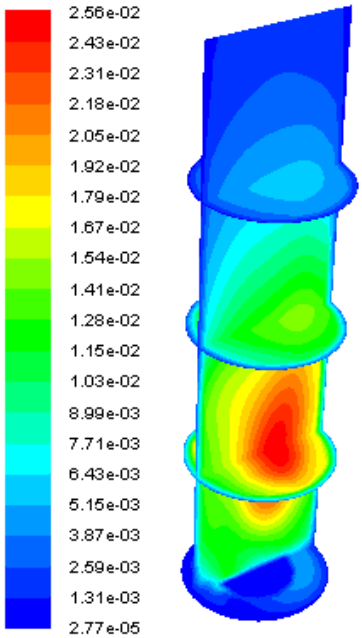

Figure 4.15: Instantaneous turbulent kinetic energy $[m^2/s^2]$

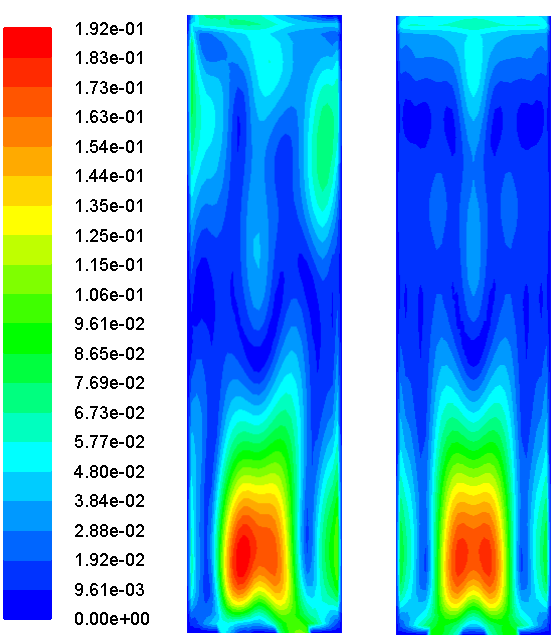

Figure 4.16: Instantaneous liquid velocity for reacting column $[m/s]$

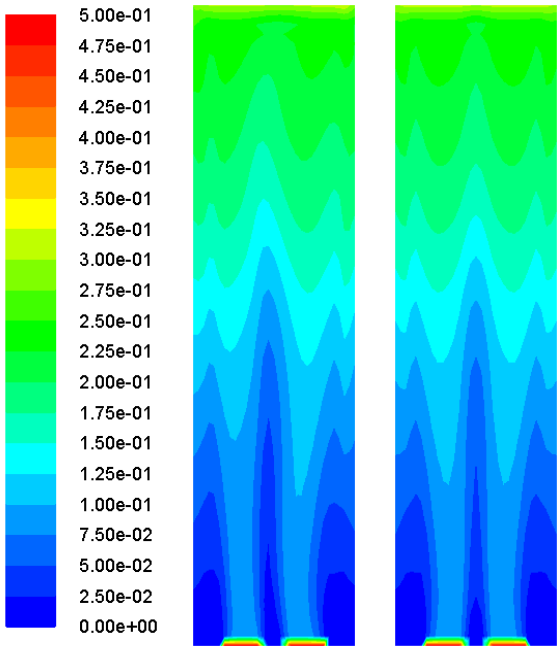

Figure 4.17: Instantaneous gas holdup for reacting column

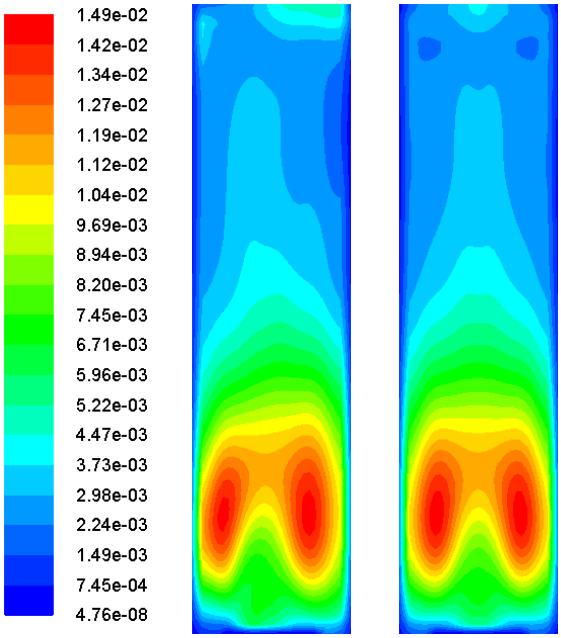

Figure 4.18: Instantaneous turbulent kinetic energy for reacting column $[m^2/s^2]$

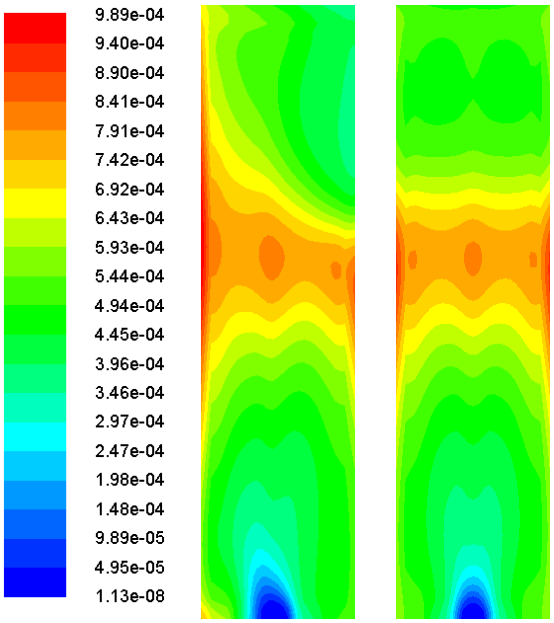

Figure 4.19: Instantaneous pyrolysis reaction rate for reacting column $[kgmol/m^3 - s]$

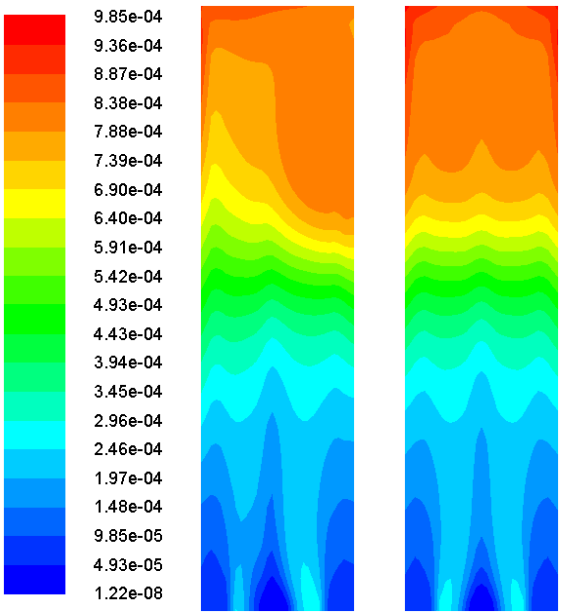

Figure 4.20: Instantaneous steam gasification reaction rate for reacting column $[kgmol/m^3 - s]$

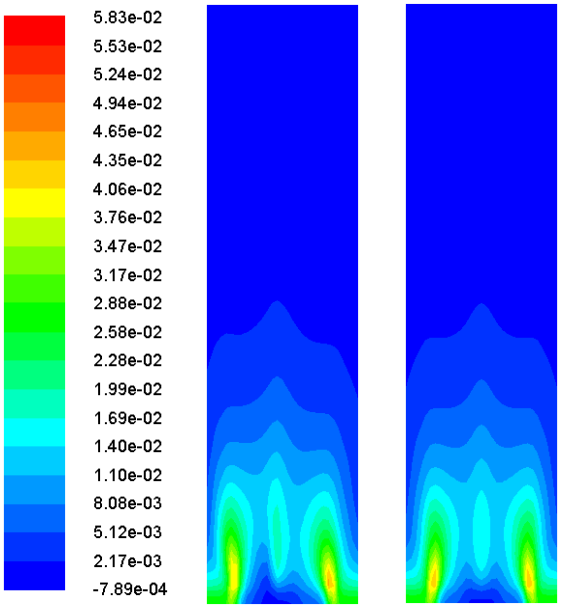

Figure 4.21: Instantaneous water-gas shift reaction rate for reacting column $[kgmol/m^3 - s]$

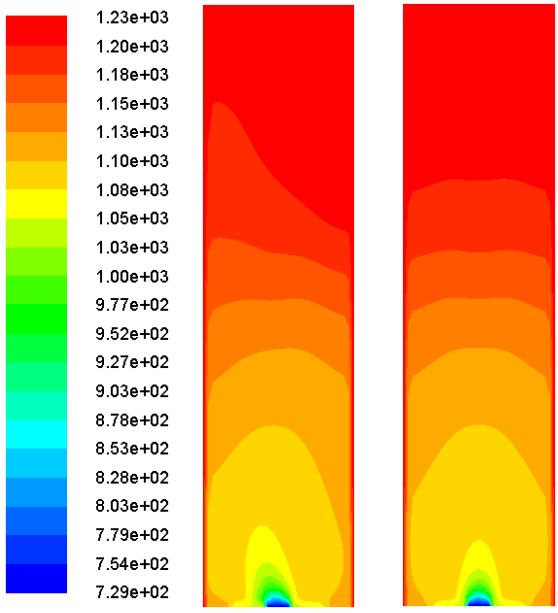

Figure 4.22: Liquid temperature of reacting column $[K]$

From what is known of the individual reaction properties, the behavior seen above is consistent with what is expected. The devolatilization reaction occurs quickly and thus is expected to have the highest rate near the inlet, with that rate being lessened by the low inlet temperature. Gasification occurs where steam is at a higher concentration, which at the lower part of the column, is where the inlet is. At the higher part of the column, this increases due to the steam generation associated with pyrolysis. The exiting gas composition is shown in Figure 4.23, and can be compared to the results of Hathaway et al. [139]. A higher H_2 content and lower CO_2 content can be seen, and is consistent with what is expected because the simulated molten salt does not react with steam. The process steam reacting with molten salt has been experimentally studied [178]. It was found that steam reacts with the melt to form bicarbonate and hydroxide ions, a process that is reversible with reintroduction of CO_2. This process was not modelled in the current investigation. It can be assumed that after a period of time, the CO_2 content with which the salt is charged would be decreased, or an additional model can be implemented to estimate CO_2 release from the salt melt reacting with H_2O. It is important to note that the products lean in favor of the gasification reaction, similar to the results of Hathaway et al. [139]. This behavior partially depends on the catalyzing effect of the molten salt and was accounted for in the gasification reaction model. The catalyzing effects of molten salt have been studied experimentally with a focus on the chemical pathways [179], and were additionally confirmed experimentally [55].

The results of this study demonstrate the viability of a reacting molten salt column reactor heated by an external source. The scale examined here is of several kilowatts, but can be increased to operate at district level power demand. A power plant model utilizing such a gasifier is proposed in the next chapter, demonstrating that hybridization of several energy sources can be of great benefit, and that renewable technologies can be integrated with conventional sources with promising results.

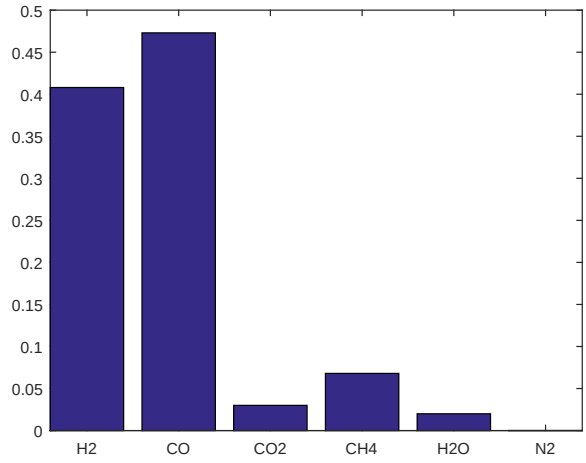

Figure 4.23: Exiting gas composition (mole fraction)

5.0 SOLAR THERMAL/BIOMASS GASIFICATION FUEL CELL POWER PLANT ENERGY ANALYSIS

The combination of solar thermal and biomass gasification technologies were evaluated in the previous chapter for a molten salt reactor. The results of the above study have produced valuable parameters necessary to model a power plant based on that solar gasification reactor. This chapter will then evaluate such a power plant, where the electricity generation will be achieved via a solid oxide fuel cell (SOFC) and turbine hybrid system, a technology that has demonstrated potential for high efficiency electricity production. Of course, the produced syngas could also be used as the feedstock for a more conventional Brayton or Rankine cycle based plant, with a corresponding reduction in overall efficiency.

5.1 PREVIOUS BIOMASS GASIFICATION PLANT DESIGNS

Gasification power plants are a fairly established technology, largely due to the large body of research of coal integrated gasification combined cycles that utilize a high temperature gas turbine Brayton cycle paired with a steam turbine to achieve higher efficiencies than in traditional coal power stations. This has been expanded to research on dedicated biomass gasification power plants. One such plant was studied by Minguez et al. from the perspective of energy, exergy, emissions, and cost [180]. Their group evaluated the performance of various biomass sources and two configurations: one that utilized CO_2 capture and another that didn't. The resulting analysis provided energy efficiency values that ranged between 0.299 and 0.423 for a plant with CO_2 capture and 0.351 to 0.483 for a plant with no CO_2 capture.

Several groups examined solar gasification power plants. Khalid et al. examined a complex system consisting of two gas turbine cycles, two Rankine cycles, an absorption chiller cycle, and an air heater, where a heliostat field focused on a solar tower provided energy for one of the Rankine cycles and the absorption cycle [181]. Kaniyal et al. examined a coal to liquids system where the coal gasifier is directly irradiated by concentrated sunlight [182]. Ozturk and Dincer also examined a solar tower coal gasification system where the energy from the solar tower generated steam that fed into the gasifier [183]. Their system was a complex plant consisting of gas turbine, two Rankine cycles, a hydrogen system, an absorption cycle for cooling, and hot water heater.

There have been several groups that have identified the potential of the use of the syngas in a solid oxide fuel cell (SOFC). Karellas et al. investigated a Biomass Heat pipe Reformer (BioHPR) and its combination with a microturbine or an SOFC [184]. Doherty et al. examined a system that combined a CHP system with an SOFC stack [185]. Bang-Moller et al. looked at a system where the syngas was fed to an SOFC stack directly after gasification [186]. In their examination, the exhausts of the fuel cell stack are combined in a combustion chamber and fed into a gas turbine. A different group examined the use of heat pipes to transport heat from an SOFC stack back to allothermal gasifier [187].

5.2 PROPOSED PLANT DESIGN

As described above, there are many configurations of solar gasification: gasification combined with an SOFC, and a multi-generation system assisted with solar energy and combined with gasification. However, there is a lack of research on combining solar gasification with an SOFC and a microturbine. The work proposed here will examine such a combination and potential improvements that can be made. The work in the previous chapter will be able to provide data on the gasifier performance that will be used in the power plant analysis.

The primary components to be integrated, as shown in Figure 5.1, include a heliostat field for concentrating solar energy (Section 5.3), a biomass gasifier for utilizing that energy to create bio-gas (Chapter 4), an SOFC for converting the gas to electricity (Section 5.5), and

the turbine and remaining balance of plant components (Section 5.6) to boost the overall efficiency. After each of these components are discussed, the various cycle configurations (Section 5.7) will be presented, and the system performance analyzed (Section 5.8). It should be noted that the receiver/gasifier performance will be calculated based on the exergy of the incoming fuel, an exergy evaluation of the solar energy being received, and the temperature and composition of the products leaving the gasifier.

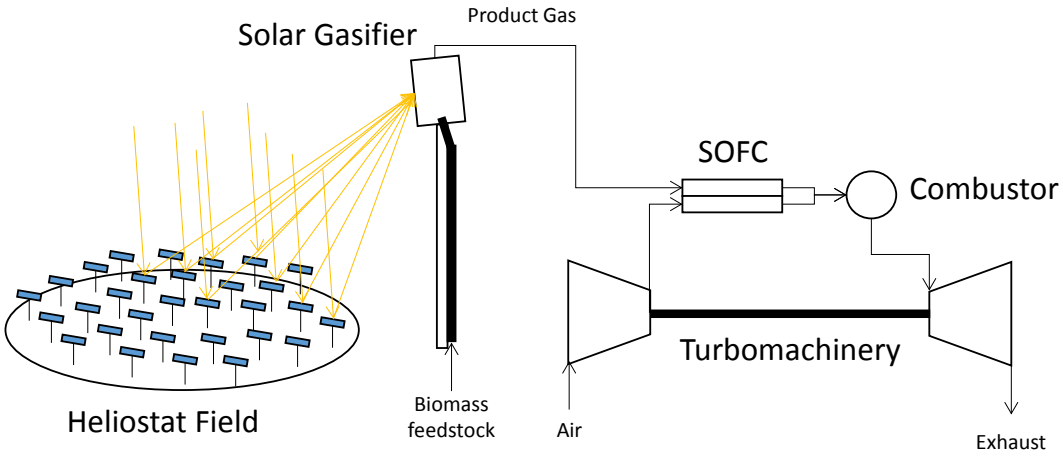

Figure 5.1: Simplified diagram of a solar gasifier with SOFC/micro-turbine power plant.

5.3 HELIOSTAT FIELD AND RECEIVER MODELING

Several previous works have examined optimized heliostat fields. Since the focus of this particular work is a system level analysis, an optimized field from another source will be chosen to be used with a cavity receiver here. However, it is important to understand the context and tools used for developing such a field. Solar tower systems depend on effective reflection of sunlight onto a single focal point. Daily and yearly variations present difficulties in terms of field design, due to shading at earlier and later times in the day, and the changing position of the sun in the sky over the yearly cycle. This has been thoroughly studied, analytically and numerically, and optimized for either existing or potential heliostat fields.

There are two main methods that are used to calculate the performance of heliostat fields. Ray-tracing methods operate on the idea of simulated rays beginning at a surface, and, as the name suggests, being traced to determine which finish on the desired surface. Reflection requires the use of this method one time to calculate which rays impact the mirrors, and a second time to identify how many reflected rays reach the final focal point. A second method called the convolution method exists where reflected rays are evaluated using cones that estimate error by convolution of the normal Gaussian distribution for the sun shape and the heliostat error.

There are a significant number of codes used for predicting and optimizing heliostat field performance, such as TRNSYS developed by Schwarzbozl et al. [188], SOLERGY developed by Stoddard et al. [189], and ECOSTAR developed by Pitz-Paal et al. [190]. Garcia et al. conducted a comparative review of a several codes with the intent of identifying and summarizing the goals, advantages and drawbacks of each [191].

A couple of novel methods also exist that build on previous methods or are entirely new. Sanchez et al. developed a computational method that calculates an optimal position for a single heliostat based on various factors and follows up by predicting the next optimal position for a second one [192]. This process iterates to fill a field, with each heliostat optimally placed. To predict an annual overall energy value for a heliostat field, Collado developed an analytical function for a heliostat that works in conjunction with an optimized mirror density distribution [193–196].

Along with extensive heliostat field studies, there is a large amount of work that has been dedicated towards optimizing receivers. The general focus of analytical studies in receiver design is the goal of optimizing heat transfer from the sun to the working fluid. This often presents unique challenges as there are drastically varying designs being utilized for cavity receivers, some based on simple cyclindrical geometries, others designed using optimization tools that are driven by the method itself.

A study by Hathaway based on previous works examined radiative heat transfer in a cylindrical cavity receiver using Monte Carlo ray tracing and a numerical finite volume method [49, 197]. Gil et al. used a finite difference method in conjunction with a radiosity method to predict radiation exchange in a cavity receiver, which they then used to optimize

the dimensions of the receiver [198]. A different method was presented by Teichel et al. that calculates semi-gray radiation within an enclosure [199]. They used this model to identify optimal emissivities for surfaces inside a cavity receiver.

5.4 CHEMICAL EXERGY OF FUELS AND GASIFICATION

Efficient gasifier design is a complex process that considers reactions, thermal effects, and energy efficiency. Chemical reactions produce or absorb heat, and optimizing these can greatly increase the potential energy that the initial fuel can produce. Exergy is a very effective measurement in this regard, as it accounts for thermal effects, chemical heating value, and even mixing potential. Traditionally thought of as a tool for just calculating the performance of power plants, it can also be used in chemical reactors, fuel cells, and any other components undergoing energy exchange. One use of this tool is in correctly identifying the potential chemical exergy of the incoming fuel. This was the focus of the study by Song et al., the result of which was a detailed method that calculated the exergy of 86 varieties of biomass [200].

An important aspect in optimizing thermodynamic systems that involve chemical reactions is predicting the exergetic performance of the individual components. For gasification, the gasifier is the focus of many studies, due to the complexity of the inputs and outputs that are involved. One such aspect concerns the temperature and composition of the components that are entering, with the water content playing a large role in determining optimum performance. Stoichiometric and non-stoichiometric models can be used to evaluate gasification performance. Non-stoichiometric equilibrium models are based on minimizing Gibbs free energy without specifying the reactions that are occurring, while stoichiometric models focus on the species that occur in the largest quantities. Karamarkovic et al. evaluated air gasification using a complex stoichiometric equilibrium model based on the carbon-boundary temperature which can be found based on specific moisture content [51].

5.5 SOLID OXIDE FUEL CELL TECHNOLOGY

5.5.1 Fuel Cell Performance

The materials out of which a fuel cell is constructed determine its type. These materials also partially determine the way the fuel cell operates, and several properties that are associated with it, such as power density, sensitivity to certain chemicals, and lifetime. As the name suggests, SOFCs are constructed using ceramic materials. Most fuel cells consist of an anode, a cathode, and an electrolyte. The anode in SOFCs is typically a mixture of nickel and yttria stabilized zirconia (YSZ), the latter of which is also used as the electrolyte [201]. The reaction that typically occurs at the anode is the combination of oxygen ions and hydrogen, as shown [201]:

$$H_2 + O^{2-} \rightarrow H_2O + 2e^- \tag{5.1}$$

The cathode is typically made using lanthanum strontium manganite (LSM) and is designed to reduce oxygen, as follows [201]:

$$\frac{1}{2}O_2 + 2e^- \rightarrow O^{2-} \tag{5.2}$$

The standard operation for an SOFC is for the fuel to enter on the anode side, where the oxygen ions that have diffused through the electrolyte react to form water. Air enters on the cathode side, sometimes called the air electrode. The electrolyte is an electrically insulating ceramic that allows ions to pass through for the reaction to continue to occur. However, these materials only become ionically and electrically conductive at high temperatures, between 800^oC and 1000^oC, requiring most SOFCs to operate in this range [201]. Figure 5.2 demonstrates a diagram of a typical fuel cell and the chemical reactions occurring.

While the ideal fuel for SOFCs and most fuel cells in general is H_2, in reality it is very energetically expensive to obtain pure hydrogen, and the fuel will typically be a mixture of H_2, CO, CH_4, and CO_2, with some low amounts of other chemicals. CO has high exothermic potential and some have researched its potential use as a fuel for fuel cell operation. However,

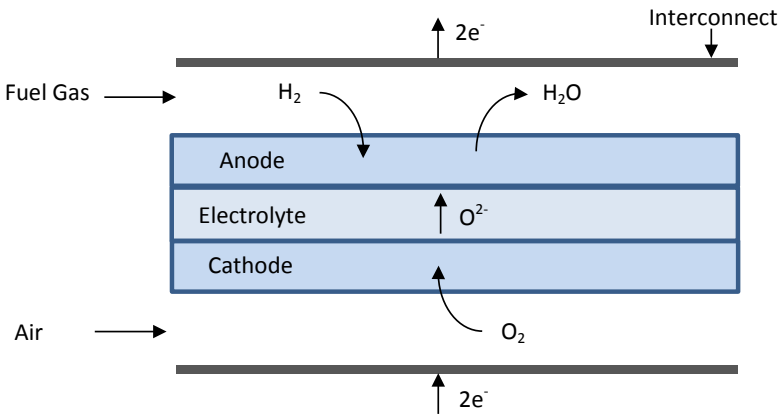

Figure 5.2: Diagram of a fuel cell

it has been shown that it does not perform as well as hydrogen [202]. It is thus more beneficial to use it in an intermediate water-gas shift reaction to produce more hydrogen:

$$CO + H_2O \rightarrow CO_2 + H_2 \tag{5.3}$$

Similar to CO, methane cannot be directly used in the fuel cell reaction, but can easily be reformed with steam to produce hydrogen [202], as shown:

$$CH_4 + H_2O \rightarrow CO + 3H_2 \tag{5.4}$$

It is immediately clear that one of the products of the anode reaction is the reactant for reforming reactions that produce additional hydrogen. Typically, more steam is mixed with the fuel, driving the methane reforming and water-gas shift reactions [201, 202].

There are several advantages that SOFCs and fuel cells in general have over traditional power generation technologies. Most traditional power plants convert chemical energy to thermal energy, after which the thermal energy is used in a thermal cycle to produce mechanical energy. There are several disadvantages to this energy pathway. There is a loss in potential useful energy in the transition of chemical energy to thermal energy, as thermal energy is limited by the Carnot efficiency, as discussed above. There is additional loss in the

conversion of thermal energy to mechanical energy. No cycle exists that can utilize chemical energy at its highest reaction temperature in perfect conversion. Typically, coal power plants operate at an efficiency of 36% [203] and combined cycle gas turbines operate at 44% [204]. Fuel cells can bypass this pathway entirely and have been shown to reach efficiencies of 60% [205].

The high operating temperature of SOFCs allows for them to be combined with other thermal technologies to produce heat, power, and/or some other beneficial application. One favorable combination is the use of the exhaust from the fuel cell anode and cathode to drive a gas turbine, replacing or supplementing the traditional combustion process, and producing additional power. Several studies have evaluated this combination in various configurations. Sucipta et al., for example, used an SOFC-MGT model with internal reforming and recuperation to examine the efficiency behavior based on gas composition simulating product gas from biomass gasification using air, oxygen, or steam [206]. Komatsu et al. examined the behavior of an SOFC-MGT system under part-load operation, finding that reducing SOFC load lowered operating temperatures and reduced efficiency [207]. A study by Park et al. evaluated the potential for retrofitting an existing standard gas turbine to operate with an SOFC [208]. Song et al. developed a more detailed model, predicting the performance of a tubular SOFC using a quasi-two dimensional approach [209]. A component level study of the performance of an SOFC by Janardhanan et al. examined the effect of direct internal reforming, compared to pre-reformed fuel, and how each behaved in the isothermal and adiabatic regimes [210]. Whiston et al. developed a dynamic one-dimensional model capable of modelling the response to varying inputs with respect to time [211].

Typical SOFC models consist of a one-dimensional finite difference approximation along the channel, incorporating the electrochemical behavior, species and mass balance, and energy conservation [209, 212–215]. These models have been shown to fairly accurately predict behavior and have been validated using experimental data. More extensive models have also been proposed, from the quasi-two dimensional one mentioned above, to two- and three-dimensional CFD simulations [216–218].

5.5.2 SOFC stack model

As mentioned above, there are numerous studies that focus on SOFC models. A lumped system model was used in this investigation for the SOFC stack.

The average operating temperature for the model was chosen to be $1173K$. This is estimated as the average between the cathode inlet and cathode outlet, since there is a much higher mass flow rate and heat capacity through the cathode. Additionally, the exiting temperature is limited to $1300K$ to account for the thermal limits of the materials.

A utilization factor of 0.85 was chosen for the model. This factor was applied to the reacting anode gases, assuming that CO and CH_4 undergo reactions in the anode channel, as shown in equations 5.3 and 5.4. The exiting anode gas composition was calculated using Gibbs energy minimization, operating on the assumption that the gases exit at equilibrium. The exiting cathode composition is calculated based on the stoichiometric requirement of O_2 for the anode fuel utilized.

A reversible cell voltage, determined by the Nernst potential, describes the highest potential achievable for a fuel cell [211, 219]:

$$E_N = -\frac{\Delta \bar{g}_f^o(T_{SOFC})}{2F} + \frac{\bar{R}T_{SOFC}}{2F} ln\left(\frac{\bar{p}_{H_2}\bar{p}_{O_2}^{1/2}}{\bar{p}_{H_2O}p^{o\frac{1}{2}}}\right) \tag{5.5}$$

where $\bar{p}_i$ is the average pressure of the species i in the anode or cathode channel, $\Delta \bar{g}_f^o(T_{SOFC})$ is the change in molar Gibbs free energy of the oxidation reaction at standard pressure and the average temperature of the SOFC, $\bar{R}$ is the universal gas constant, and F is Faraday's constant.

There are several irreversibilities that occur in the SOFC. Activation polarization is defined as the energy loss associated with overcoming the activation energy to facilitate reaction, and is typically expressed as shown [219]:

$$j = j_0 \left[exp\left(\frac{\alpha \eta_{act} n_e F}{\bar{R}T_{SOFC}}\right) - exp\left(\frac{-(1-\alpha)\eta_{act} n_e F}{\bar{R}T_{SOFC}}\right)\right] \tag{5.6}$$

where η_{act} is the activation polarization, j is the current density, j_0 is the exchange current density, and n_e is the number of moles of electrons transferred. It is typical to assume that $\alpha = 0.5$, and manipulate the above equation to take the following form:

$$\eta_{act} = \frac{2\bar{R}T_{SOFC}}{n_e F} sinh^{-1}\left(\frac{j}{2j_0}\right) \tag{5.7}$$

The anode and cathode channels are evaluated separately with two different values acquired for the exchange current densities [220]:

$$j_{0,an} = \gamma_{an}\left(\frac{\bar{p}_{H_2}}{p_{SOFC}}\right)\left(\frac{\bar{p}_{H_2O}}{p_{SOFC}}\right) exp\left(-\frac{E_{act,an}}{\bar{R}T_{SOFC}}\right) \tag{5.8}$$

$$j_{0,cat} = \gamma_{cat}\left(\frac{\bar{p}_{O_2}}{p_{SOFC}}\right)^{0.25} exp\left(-\frac{E_{act,cat}}{\bar{R}T_{SOFC}}\right) \tag{5.9}$$

Concentration polarization is defined as the loss in voltage potential associated with lower concentrations at the site of reaction. This is expressed separately for the anode and cathode [221]:

$$\eta_{con,an} = -\frac{\bar{R}T_{SOFC}}{2F} ln\left(\frac{1-(j\bar{R}T_{SOFC}\delta_{an}/2FD_{an,eff}\bar{p}_{H_2})}{1+(j\bar{R}T_{SOFC}\delta_a n/2FD_{an,eff}\bar{p}_{H_2O})}\right) \tag{5.10}$$

$$\eta_{con,cat} = -\frac{\bar{R}T_{SOFC}}{2F} ln\left(\frac{1}{\bar{y}_{O_2}} - \left(\frac{1}{\bar{y}_{O_2}} - 1\right) exp\left(\frac{j\bar{R}T_{SOFC}\delta_{cat}}{4FD_{cat,eff}p_{SOFC}}\right)\right) \tag{5.11}$$

where $\bar{y}_i$ is the average concentration of species i, $D_{i,eff}$ is the effective diffusion coefficient, and $\delta_a n$ and $\delta_c at$ are the thicknesses of the anode and cathode, respectively.

Ohmic polarization is associated with the electrical resistance experienced by the ions and electrons passing through the electrodes and interconnects. Typically, four main components are examined when estimating the ohmic polarization: the anode, cathode, electrolyte, and interconnect. The expressions for the conductivity of each component is as follows [211]:

$$\text{Anode conductivity} \qquad \frac{95\times10^6 KSm^{-1}}{T_{SOFC}} exp\left(-\frac{1150K}{T_{SOFC}}\right) \tag{5.12}$$

$$\text{Cathode conductivity} \qquad \frac{42\times10^6 KSm^{-1}}{T_{SOFC}} exp\left(-\frac{1200K}{T_{SOFC}}\right) \tag{5.13}$$

$$\text{Electrolyte conductivity} \qquad 3.34\times10^4 KSm^{-1} exp\left(-\frac{10300K}{T_{SOFC}}\right) \tag{5.14}$$

$$\text{Interconnect conductivity} \qquad \frac{9.3\times10^6 KSm^{-1}}{T_{SOFC}} exp\left(-\frac{1100K}{T_{SOFC}}\right) \tag{5.15}$$

Table 5.1: Property values chosen for the SOFC model

Property	Value
δ_{an}	$50\mu m$
δ_{cat}	$50\mu m$
δ_{el}	$40\mu m$
δ_{int}	$2500\mu m$
$D_{a,eff}$	$2.1 \times 10^{-5} m^2/s$
$D_{c,eff}$	$5.4 \times 10^{-6} m^2/s$
$E_{act,an}$	$100 \times 10^3 J/mol$
$E_{act,cat}$	$120 \times 10^3 J/mol$
γ_{an}	$5.5 \times 10^8 A/m^2$
γ_{cat}	$7 \times 10^8 A/m^2$

The thicknesses of each component are chosen based on those used in previous studies [211, 220]. Other values for the constants used in the model are additionally based on those found in the literature [211, 221]. Table 5.1 shows the values chosen. The actual cell voltage is calculated based on the reversible cell voltage and the various losses, as shown:

$$V_{cell} = E_n - \eta_{act} - \eta_{conc} - \eta_{ohm} \tag{5.16}$$

The stack power is calculated based on the cell voltage and the current, where the current is calculated based on the amount of fuel that is reacted:

$$I = 2FU_f(\dot{n}_{H_2,IN} + \dot{n}_{CO,IN} + \dot{n}_{CH_4,IN}) \tag{5.17}$$

The subscript IN indicates that the values are taken to be those at the anode entrance. The stack power is then calculated as follows:

$$\dot{W}_{SOFC} = V_{cell} * I \tag{5.18}$$

The energy efficiency of the SOFC is calculated based on the power of the cell related to the lower heating value (LHV) and molar flow rate of the anode gases, as shown:

$$\eta_{SOFC} = \frac{\dot{W}_{SOFC}}{\sum LHV^i \dot{n}^i_{a,IN}} \tag{5.19}$$

The SOFC stack is assumed to be adiabatic. This assumption allows the calculation of the exiting temperature of the anode and cathode gases. It assumed that the exiting anode and cathode temperatures are equal. The following energy balance is used in the calculation:

$$\sum \dot{n}^i_{an,IN} h^i + \sum \dot{n}^i_{cat,IN} h^i = \dot{W}_{SOFC} + \sum \dot{n}^i_{an,OUT} h^i + \sum \dot{n}^i_{cat,OUT} h^i \tag{5.20}$$

A more complete measure of the efficiency for the SOFC is an exergy based evaluation of the inputs and outputs. The exergy efficiency is defined as ratio of the total outputs to the total inputs:

$$\eta_{\phi,SOFC} = \frac{\dot{W}_{SOFC} + \sum \dot{n}^i_{an,OUT} \phi^i + \sum \dot{n}^i_{cat,OUT} \phi^i}{\sum \dot{n}^i_{an,IN} \phi^i + \sum \dot{n}^i_{cat,IN} \phi^i} \tag{5.21}$$

The energy delivered by the SOFC must be converted to alternating current via an inverter. These are typically taken to be 95% efficient, and a grid SOFC power output can be defined as follows:

$$\dot{W}_{SOFC,grid} = \dot{W}_{SOFC} \times \eta_{inv} \tag{5.22}$$

5.6 MODELING POWER PLANT COMPONENTS

Three power plant designs were examined in the study with the goal of identifying a configuration that would have the highest exergetic efficiency. These designs will be described in more details in Section 5.7. Each design consisted of several heat exchangers/evaporators, turbomachinery (compressors and expanders), the gasifier (modeled using the detailed results of the CFD study), the fuel combustor, and the SOFC (model is explained above). The models for the components not yet described are explained below.

5.6.1 Heat Exchangers

While several heat exchangers are used in the model, there are two simple configurations: preheater and evaporator. The general diagram for both of these is shown in Figure 5.3, where the subscript H stands for the hot stream and C for the cold stream.

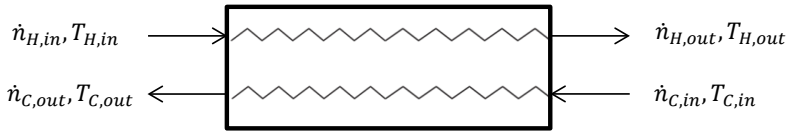

Figure 5.3: Heat Exchanger/Evaporator Diagram

There are two options for the calculating the inputs and outputs of either the heat exchanger or the evaporator: 1)The output temperature is preassigned due to SOFC/gasifier requirements, or 2)The effectiveness is assigned and the output temperature is calculated. Since it is assumed that there are no reactions occurring within the exchanger, the molar flow rates and compositions of the two streams remain unchanged:

$$\begin{aligned} \dot{n}^i_{H,in} &= \dot{n}^i_{H,out} \quad \text{for i=} H_2,\ O_2,\ CH_4,\ H_2O,\ CO,\ CO_2,\ N_2 \\ \dot{n}^i_{C,in} &= \dot{n}^i_{C,out} \quad \text{for i=} H_2,\ O_2,\ CH_4,\ H_2O,\ CO,\ CO_2,\ N_2 \end{aligned} \tag{5.23}$$

Both cases depend on the energy equation and the effectiveness equation, given below, where the effectiveness set to an upper limit of $\epsilon \leq 0.85$, when one output temperature is assigned, while if both outputs remain unknown, the effectiveness is preset to a value of $\epsilon = 0.85$.

$$\sum \dot{n}^i_{H,in} h^i_{H,in} + \sum \dot{n}^i_{C,in} h^i_{C,in} = \sum \dot{n}^i_{H,out} h^i_{H,out} + \sum \dot{n}^i_{C,out} h^i_{C,out} \tag{5.24}$$

$$\epsilon = \begin{cases} \dfrac{T_{H,in} - T_{H,out}}{T_{H,in} - T_{C,in}} & \text{if } C_{p,min} = C_{p,H} \quad (5.25a) \\ \dfrac{T_{C,out} - T_{C,in}}{T_{H,in} - T_{C,in}} & \text{if } C_{p,min} = C_{p,C} \quad (5.25b) \end{cases}$$

It is important to note that in the case of the evaporator, the cold stream composition consists of water and cellulose, where water undergoes evaporation and superheating, while

the cellulose undergoes a temperature increase. Under these conditions, the effectiveness is constrained to the case where $C_{p,min} = C_{p,H}$.

The exergetic performance of the heat exchangers is calculated by evaluating the ratio of the total exergy leaving the system to the total exergy entering the system, as follows:

$$\eta_{\phi,exch} = \frac{\sum \dot{n}^i_{H,out}\phi^i_{H,out} + \sum \dot{n}^i_{C,out}\phi^i_{C,out}}{\sum \dot{n}^i_{H,in}\phi^i_{H,in} + \sum \dot{n}^i_{C,in}\phi^i_{C,in}} \tag{5.26}$$

Exergy destruction is quantified as the difference between input and output exergy streams:

$$\phi_{exch,dest} = \sum \dot{n}^i_{H,in}\phi^i_{H,in} + \sum \dot{n}^i_{C,in}\phi^i_{C,in} - \sum \dot{n}^i_{H,out}\phi^i_{H,out} - \sum \dot{n}^i_{C,out}\phi^i_{C,out} \tag{5.27}$$

5.6.2 Combustor

The anode gases leaving the SOFC retain a portion of useful chemical energy. This remaining portion is utilized in a combustor that mixes the anode and cathode gases, facilitating the following reactions:

$$H_2 + \frac{1}{2}O_2 \rightarrow H_2O \tag{5.28}$$

$$CO + \frac{1}{2}O_2 \rightarrow CO_2 \tag{5.29}$$

$$CH_4 + 2O_2 \rightarrow CO_2 + 2H_2O \tag{5.30}$$

The above equations are assumed to consume the reactant gases to completion, allowing for stoichiometric calculation of the exiting components, as shown:

$$\begin{aligned}
\dot{n}_{H2,out} &= 0 \\
\dot{n}_{CO,out} &= 0 \\
\dot{n}_{CH4,out} &= 0 \\
\dot{n}_{H_2O,out} &= \dot{n}_{H_2O,in} + \dot{n}_{H_2,in} + 2\dot{n}_{CH_4,in} \\
\dot{n}_{CO_2,out} &= \dot{n}_{CO_2,in} + \dot{n}_{CO,in} + \dot{n}_{CH_4,in} \\
\dot{n}_{O_2,out} &= \dot{n}_{O_2,in} - \frac{1}{2}\dot{n}_{H_2,in} - \frac{1}{2}\dot{n}_{CO,in} - 2\dot{n}_{CH_4,in}
\end{aligned} \tag{5.31}$$

The exiting tempeature is calculated based on the energy equation:

$$\sum \dot{n}^i_{an,stream} h^i_{an,stream} + \sum \dot{n}^i_{cat,stream} h^i_{cat,stream} = \sum \dot{n}^i_{out} h^i_{out} \tag{5.32}$$

The mixing of gases and conversion of chemical energy to thermal energy can be a significant source of exergy destruction. The exergy efficiency of the combustor is measured as the ratio of the output stream to the sum of the input streams:

$$\eta_{\phi,exch} = \frac{\sum \dot{n}^i_{out} \phi^i_{out}}{\sum \dot{n}^i_{an,stream} \phi^i_{an,stream} + \sum \dot{n}^i_{cat,stream} \phi^i_{cat,stream}} \tag{5.33}$$

The amount destroyed in the mixing and combustion process can be quantified as shown:

$$\phi_{comb,dest} = \sum \dot{n}^i_{an,stream} \phi^i_{an,stream} + \sum \dot{n}^i_{cat,stream} \phi^i_{cat,stream} - \sum \dot{n}^i_{out} \phi^i_{out} \tag{5.34}$$

5.6.3 Compressor and Expander

Work can be extracted or input into a fluid via expansion and compression, respectively. SOFCs typically operate at above atmospheric pressure to achieve higher performance, requiring compression work for both the anode and cathode streams. This work can be returned with some additional power generation by expanding the gases leaving the combustor. Figures 5.4 and 5.5 display diagrams of a compressor and expander/turbine. For both compressors and turbines, it is assumed that there are no chemical reactions taking place inside the turbomachinery. This is represented as:

$$\dot{n}_{in,comp/turb} = \dot{n}_{out,comp/turb} \tag{5.35}$$

The outlet temperature for the components can be calculated based on the input and output pressures and the isentropic efficiencies assigned for the components, assuming single phase/vapor behavior:

$$T_{out} = T_{in} + \frac{T_{in}}{\eta_{comp}} \left(\left(\frac{p_{out}}{p_{in}} \right)^{\frac{R}{c_p}} - 1 \right) \tag{5.36}$$

$$T_{out} = T_{in} + T_{in} \eta_{turb} \left(\left(\frac{p_{out}}{p_{in}} \right)^{\frac{R}{c_p}} - 1 \right) \tag{5.37}$$

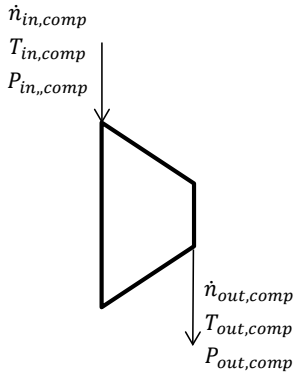

Figure 5.4: Compressor diagram

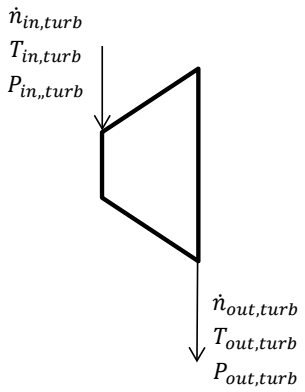

Figure 5.5: Turbine diagram

For this study, $\eta_{comp} = 0.75$ and $\eta_{turb} = 0.84$. These values are similar to those found in the literature for similar investigations [186]. The compressor and turbine work is calculated from the difference in input and output energy:

$$\dot{W}_{comp} = \sum \dot{n}^i_{comp,out} h^i_{comp,out} - \sum \dot{n}^i_{comp,in} h^i_{comp,in} \tag{5.38}$$

$$\dot{W}_{turb} = \sum \dot{n}^i_{turb,in} h^i_{turb,in} - \sum \dot{n}^i_{turb,out} h^i_{turb,out} \tag{5.39}$$

The compressor work is expected to be greater than the difference between the fluid input and output exergy. The ratio of the two values is known as the exergetic efficiency of the compressor:

$$\eta_{\phi,comp} = \frac{\sum \dot{n}^i_{comp,out} \phi^i_{comp,out} - \sum \dot{n}^i_{comp,in} \phi^i_{comp,in}}{\dot{W}_{comp}} \tag{5.40}$$

The exergetic performance of the turbine is evaluated as the work output compared to the difference in exergy between the outlet and inlet:

$$\eta_{\phi,turb} = \frac{\dot{W}_{turb}}{\sum \dot{n}^i_{turb,in} \phi^i_{turb,in} - \sum \dot{n}^i_{turb,out} \phi^i_{turb,out}} \tag{5.41}$$

The above individual components can be configured together in multiple ways. Three configurations are examined in the next section with the goal of identifying a superior configuration and/or optimum operating point.

5.7 DESIGN CONFIGURATIONS

The goal of power plant design is achieving the highest performance while meeting desired constraints. This is dependent on the definition of the constraints and the definition of performance. For the current investigation, power plant performance is defined as the exergetic efficiency of the overall system. Constraints are found in the form of material limitations of the SOFC and gasifier, exchanger effectiveness, and turbomachinery efficiencies. Three configurations are put forth and examined based on these criteria. The overall system is divided into two major components: The gasifier sub-system, shown in Figure 5.6, and the SOFC power plant sub-system.

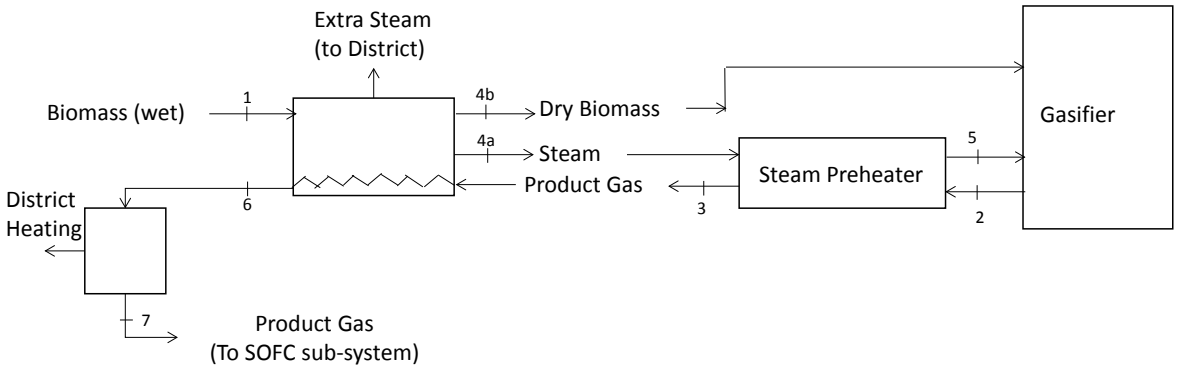

Figure 5.6: Gasifier sub-model with evaporator and preheater

The gasifier subsystem is designed to utilize heat from the product gases leaving the gasifier to preheat the steam that will be used in the gasification reaction and dry and partially preheat the biomass. Since the gasifier is designed to operate at atmospheric pressure, the product gases will require compression before being utilized in the SOFC.

It is then advantageous to lower the gas temperature prior to compression, while utilizing the removed heat to preheat the reactants.

The SOFC power plant sub-system configurations are shown in Figures 5.7, 5.8, and 5.9. It can be seen that the variation between configurations consists of the method of anode and cathode stream preheating. The configuration in Figure 5.7 utilizes a recuperator with an effectiveness of $\epsilon = 0.85$ to preheat the cathode stream, with additional preheat supplemented by the cathode-side SOFC exit stream. The anode side is configured to only utilize the SOFC anode exit stream to preheat the entering anode gas.

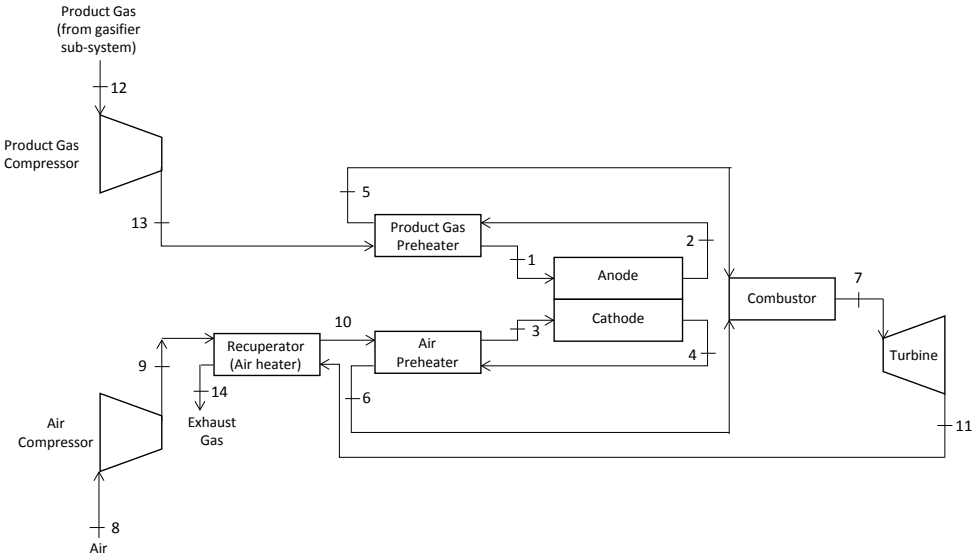

Figure 5.7: Configuration 1: SOFC power plant configuration with two preheaters and one recuperator

The second configuration, shown in Figure 5.8, does not utilize the SOFC exiting streams to preheat the entering gases. The entirety of the preheating is accomplished by the turbine exiting stream. It is later shown that this configuration is limited in operating SOFC pressure, but presents other advantages.

The third configuration, shown in Figure 5.9, is designed to use the SOFC anode and cathode exiting streams to preheat incoming streams to the SOFC operating point, while the exhaust gas is not utilized in the configuration, and may be utilized for a bottoming cycle.

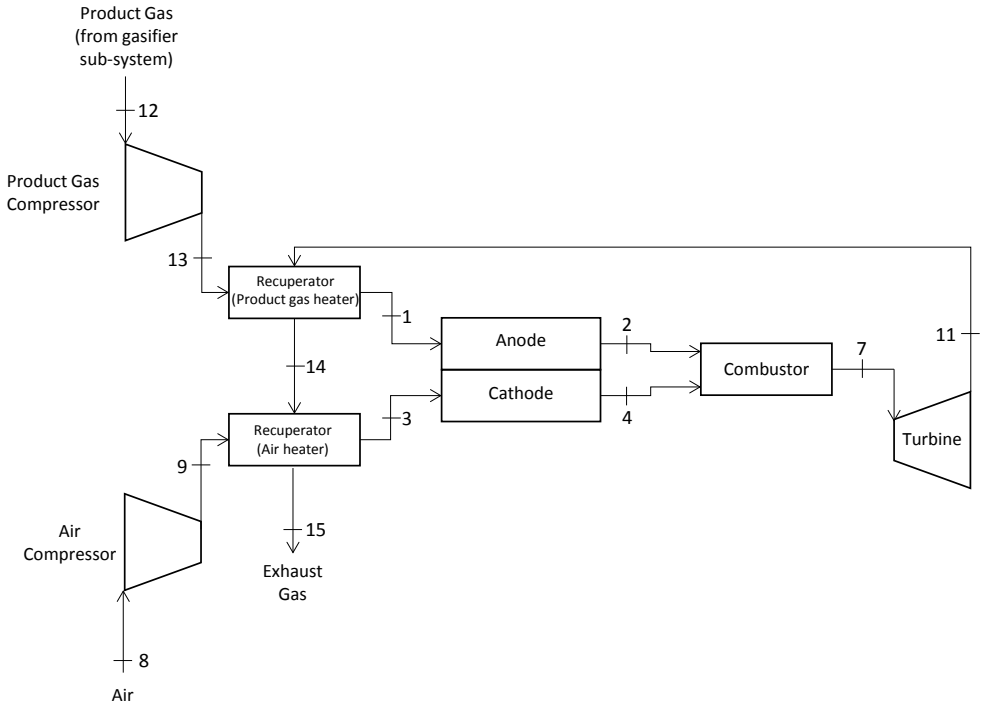

Figure 5.8: Configuration 2: SOFC power plant configuration with no preheaters and two recuperators

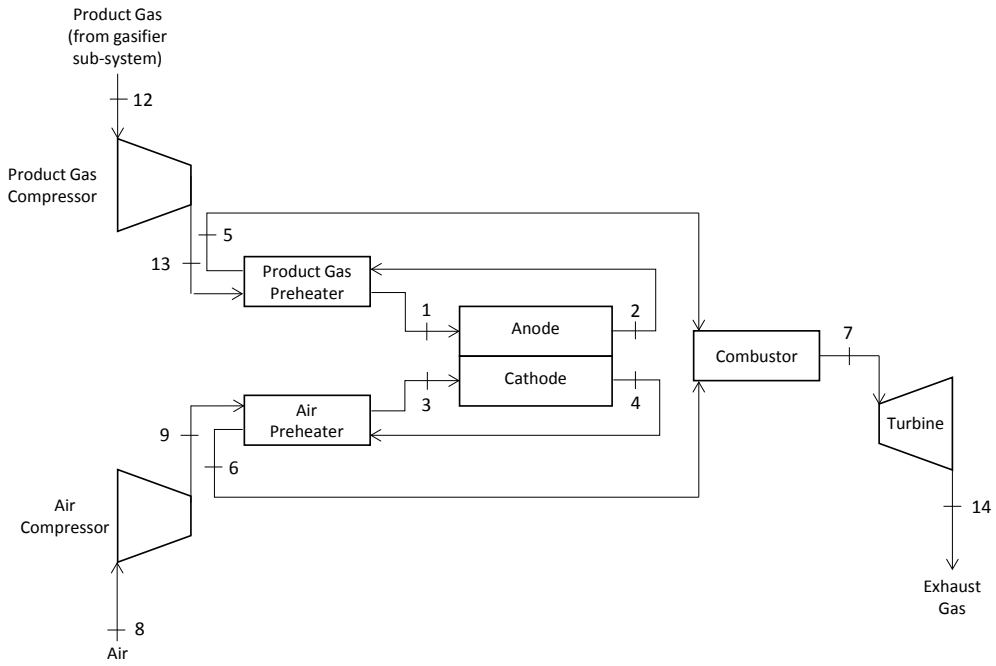

Figure 5.9: Configuration 3: SOFC power plant configuration with two preheaters and no recuperators

The scale of the power plant system can be determined by the desired amount of biomass that is put into the sytem. The gasifier in the previous chapter was designed for a small-scale application, such as a pilot scale plant. The following analysis examines a larger scale model where a biomass input of $100kg/hr$ of wet biomass is assumed. The biomass is assumed to have a moisture content of 15% by mass.

5.8 PERFORMANCE ANALYSIS

Obviously, there are a number of parameters which can be varied to examine the overall system performance. This section will discuss these parameters, and explore their effects.

5.8.1 Gasifier sub-system

First, we must examine the gasifier, since it provides the synthesis gas for all of the cycle configurations. There are several inputs and outputs associated with a solar gasifier and the sub-system surrounding it. The gasifier can be treated as a control volume where the inputs are solar heat, steam, and biomass, while the output is a product gas. The CFD analysis in the previous chapter provides the product gas composition and temperature for a pre-defined heat, steam, and biomass input. These results can be used to examine the energetic and exergetic efficiencies of the gasifier and sub-system, allowing for comparison with other solar and traditional gasifier systems. The efficiency of the gasifier is dependent on the efficiency of the solar receiver. The amount of heat entering the receiver is designated as $\dot{Q}_{solar}$ at a temperature of $5600K$ (black body temperature of the sun)[79]. This thermal energy is transferred to the absorber, with the amount that the absorber receives designated as $\dot{Q}_{abs}$, entering at an average temperature of $1300K$. The amount of exergy carried in $\dot{Q}_{solar}$ can be expressed as:

$$\dot{\Phi}_{solar} = \dot{Q}_{solar}\left(1 - \frac{T_o}{T_s}\right) \tag{5.42}$$

where T_o is the environmental temperature (here taken to be $298K$), and $T_s = 5600K$. The exergy of the heat received by the absorber is expressed using the same method:

$$\dot{\Phi}_{abs} = \dot{Q}_{abs}\left(1 - \frac{T_o}{T_{abs}}\right) \tag{5.43}$$

where $T_{abs} = 1300K$. The thermal efficiency of the receiver can quantified as the ratio of energy entering the receiver to the solar thermal energy entering the cavity:

$$\eta_{receiver} = \frac{\dot{Q}_{abs}}{\dot{Q}_{solar}} \tag{5.44}$$

There have been numerous studies on cavity receivers. For the type of design assumed in this study, an absorbing cavity receiver is able to achieve thermal efficiency values of $\eta_{receiver} = 0.44 - 0.63$, depending on the design. Several other measures of efficiency are additionally used in examining gasifier performance. The cold gas efficiency, often used for standard gasifiers, is a measure of the output gas lower heating value related to the input biomass lower heating value:

$$\eta_{CG} = \frac{\dot{m}_{product\ gas} LHV_{product\ gas}}{\dot{m}_{biomass} LHV_{biomass}} \tag{5.45}$$

The absorber efficiency of the gasifier is defined as the amount of heating value added to the stream in relation to the input heat:

$$\eta_{abs} = \frac{\dot{m}_{product\ gas} LHV_{product\ gas} - \dot{m}_{biomass} LHV_{biomass}}{\dot{Q}_{abs}} \tag{5.46}$$

A solar efficiency can additionally be defined based on the above equation and equation 5.44, as follows:

$$\eta_{solar} = \eta_{receiver} \times \eta_{abs} = \frac{\dot{m}_{product\ gas} LHV_{product\ gas} - \dot{m}_{biomass} LHV_{biomass}}{\dot{Q}_{solar}} \tag{5.47}$$

The exergy efficiency of the gasifier can be defined as the exergy of the exiting stream in relation to the incoming thermal, biomass, and steam streams:

$$\eta_{\phi,gasifier} = \frac{\dot{\Phi}_{product\ gas}}{\dot{\Phi}_{solar} + \dot{\Phi}_{biomass} + \dot{\Phi}_{steam}} \tag{5.48}$$

Table 5.2: Gasifier sub-system state properties

State point	$T[^oC]$	$\dot{m}[g/s]$	$\dot{\Phi}[kW]$
1	15	27.8	469
2	1200	25.6	453
3	1150	25.6	451
4a	400	2.0	1
4b	400	23.6	470
5	1050	2.0	3
6	619.7	25.6	441
7	200	25.6	429

The above definition can then be expanded to the entire gasifier sub-system, as follows:

$$\eta_{\phi,gasifier\ sub-system} = \frac{\dot{\Phi}_{product\ gas\ to\ SOFC} + \dot{\Phi}_{district\ heat}}{\dot{\Phi}_{solar} + \dot{\Phi}_{wet\ biomass}} \tag{5.49}$$

When considering exergy flow that is directed only to the SOFC sub-system, the exergy efficiency of the system takes the following form:

$$\eta_{\phi,gasifier\ sub-system,2} = \frac{\dot{\Phi}_{product\ gas\ to\ SOFC}}{\dot{\Phi}_{solar} + \dot{\Phi}_{wet\ biomass}} \tag{5.50}$$

The above relations are used when calculating the values given in Table 5.2, which shows the properties at each state point in the sub-system. Table 5.3 shows the exergy efficiencies of the components.

There are several losses that occur throughout the gasifier sub-system. The sub-system exergy flows are illustrated in Figure 5.10 to identify the sources of exergy destruction and loss. The most notable losses are seen in the solar receiver and in the gasifier. The process of gasification creates a significant amount of exergy destruction through thermal losses, mixing, and energy conversion, and thus is expected to experience exergy destruction. The high losses in the receiver aperture are due partially to heat loss, but also to the decrease in temperature from solar black body temperature to the aperture operating temperature. While these losses can partially be mitigated by improving design, a certain amount of exergy destruction is inherently expected due to the nature of the design.

Table 5.3: Gasifier sub-system efficiency values

Measure of Efficiency	**Value(%)**
η_{CG}	117
η_{solar}	41.6
$\eta_{\phi,gasifier}$	65.1
$\eta_{\phi,dryer}$	32.2
$\eta_{\phi,pre-heater}$	75.7
$\eta_{\phi,gasifier\ sub-system}$	72.5
$\eta_{\phi,gasifier\ sub-system,2}$	70.6

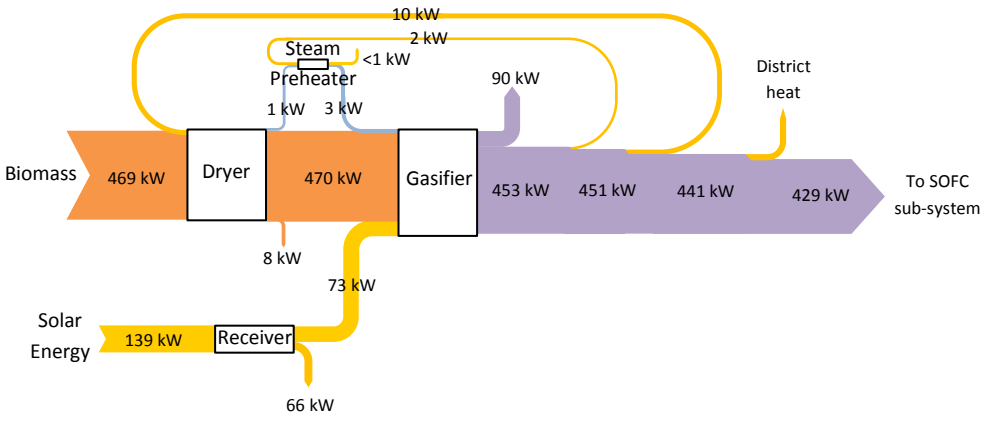

Figure 5.10: Exergy flow diagram for gasifier sub-system

5.8.2 Varying configurations and pressure

The configurations presented in Section 5.7 can be manipulated in several ways to increase performance. The constraints set by the SOFC, mainly the average and maximum temperature, limit some of the available routes of optimization. Since pressure is not directly limited by any of the materials, up to a practical degree, each configuration is examined in its performance with respect to the SOFC operating pressure for a range between $150kPa$ and $750kPa$. The exergetic efficiency of the SOFC sub-system is defined as shown:

$$\eta_{\phi,SOFC,subsystem} = \frac{\dot{W}_{SOFC,grid} + \dot{W}_{turb} - \dot{W}_{air,comp} - \dot{W}_{prod.\ gas,comp}}{\dot{\Phi}_{fuel,in} + \dot{\Phi}_{air,in}} \tag{5.51}$$

The total system exergetic efficiency is a ratio of all exergy outputs to the exergy inputs, here the main inputs being solar heat and chemical exergy in biomass, while the outputs are the net turbine work ($\dot{W}_{turb,net}$), SOFC work, and district heating:

$$\eta_{\phi,system} = \frac{\dot{W}_{SOFC,grid} + \dot{W}_{turb,net} + \dot{\Phi}_{district\ heat}}{\dot{\Phi}_{air,in} + \dot{\Phi}_{solar} + \dot{\Phi}_{wet\ biomass}} \tag{5.52}$$

Table 5.4 shows the performance of each configuration with respect to the pressure variation. It is immediately obvious that some configurations have a narrower operating range than the one originally tested, limited by the performance of the heat exchangers, or the practical necessity of the configuration. For example, there is a high pressure limit set for the configuration in Figure 5.8 due to the increasing demand on the exhaust gas to preheat a high pressure cold stream, increasing the necessary exchanger effectiveness to the limit of $\epsilon = 0.85$. Additionally, for the system in Figure 5.7, there is no need for a cathode side preheater at lower pressure, since the recuperator is capable of achieving the necessary temperature.

Table 5.4: Effect of pressure variation on efficiency for each SOFC sub-system

	$\eta_{\phi,SOFC,subsystem}$ [-]		
$P_{opr}[kPa]$	**Config. 1**	**Config. 2**	**Config. 3**
150	–	0.5394	0.4855
200	–	0.5913	0.5049
250	–	0.6242	0.5172
300	–	0.6465	0.5256
350	–	–	0.5315
400	0.6537	–	0.5358
450	0.6517	–	0.539
500	0.6483	–	0.5414
550	0.644	–	0.5432
600	0.639	–	0.5444
650	0.6337	–	0.5454
700	0.6281	–	0.546
750	0.6223	–	0.5463

5.8.3 Comparison of each design at optimum pressure

As mentioned above, each configuration operates at an optimum pressure. Here, the performance of each SOFC sub-system component is analyzed to identify the sources of exergy destruction that contribute most to decreasing the overall system efficiency. Table 5.5 summarizes the important properties at each state for all three SOFC sub-system configurations operating at optimum pressure, as well as the gasifier sub-system. Table 5.6 shows exergy destruction values and their corresponding ratio compared to the total SOFC sub-system exergy input. The exergy pathways are illustrated for each configuration in Figures 5.11, 5.12, and 5.13.

The results above can help to draw several conclusions about the overall performance of the system and each configuration. It can be noted that while the solar gasifier experiences a large heat loss associated with the receiver and absorber assembly, there is still significant conversion of chemical exergy via gasification. The cold gas efficiency and gasifier exergetic efficiency demonstrate favorable performance for the gasifier itself, and the overall gasifier sub-system.

Table 5.5: Optimum pressure states for each configurations

	Configuration 1				**Configuration 2**				**Configuration 3**			
State point	**Temp** $[^oC]$	**Pres** $[kPa]$	$\dot{m}$ $[g/s]$	$\dot{\Phi}$ $[kW]$	**Temp** $[^oC]$	**Pres** $[kPa]$	$\dot{m}$ $[g/s]$	$\dot{\Phi}$ $[kW]$	**Temp** $[^oC]$	**Pres** $[kPa]$	$\dot{m}$ $[g/s]$	$\dot{\Phi}$ $[kW]$
1	827.4	385	25.6	453	826.3	335	25.6	453	832.3	750	25.6	456
2	1048	385	49.4	134	1049	335	49.4	133	1043	750	49.4	136
3	752.4	385	396.6	207	751.3	335	396.6	202	757.3	750	396.6	230
4	1048	385	372.8	293	1049	335	372.8	289	1043	750	372.8	312
5	824	384	49.4	120					929.2	749	49.4	129
6	1020	384	372.8	283					592.9	749	372.8	169
7	1119	384	422.2	382	1178	335	422.2	402	783.1	749	422.2	271
8	15	101.3	396.6	2	15	101.3	396.6	2	15	101.3	396.6	2
9	194.6	388	396.6	63	172.8	335	396.6	55	312.2	753	396.6	106
10	724.9	388	396.6	198								
11	818.4	103	422.2	215	894.1	101.3	422.2	244	449.9	103	422.2	90
12	200	97.3	25.6	429	200	97.3	25.6	429	200	97.3	25.6	429
13	480.8	385.5	25.6	441	447.5	335.5	25.6	439	658.5	750.5	25.6	449
14	352.7	102.3	422.2	64	855.6	103	422.2	229	449.9	101.3	422.2	90
15					349	102.3	422.2	63				

An additional benefit of a solar gasifier is immediately observed when examining each of the SOFC sub-systems. At optimum pressure, configurations 1 and 2 achieve very high values of efficiency, due in large part to the high quality of energy coming in via the product gas stream. This is an important advantage that solar gasifiers have over the traditional autothermal designs, where traditionally part of the gas stream has to undergo oxidation to generate the thermal energy requirement. The efficiencies of the two subsystems combine together to demonstrate a highly exergetically efficient design.

A comparison of the exergy destructions from Table 5.6 provides insight into the largest sources of exergy loss/destruction. Immediately, it is obvious that the loss via the flue gas leaving the system is the largest source of destruction. However, while in the current model this is an exergy loss, the flue gas has latent heat that can be used for a bottoming cycle, such as an organic Rankine cycle, or a flash cycle, similar to those discussed in Chapter 3. The addition of any of these would further increase the overall exergy efficiency of the system. If the loss of the flue gas exergy is not considered in the total, assuming it is useful exergy leaving the system towards another system, the total exergy destruction within the SOFC sub-system components can be identified.

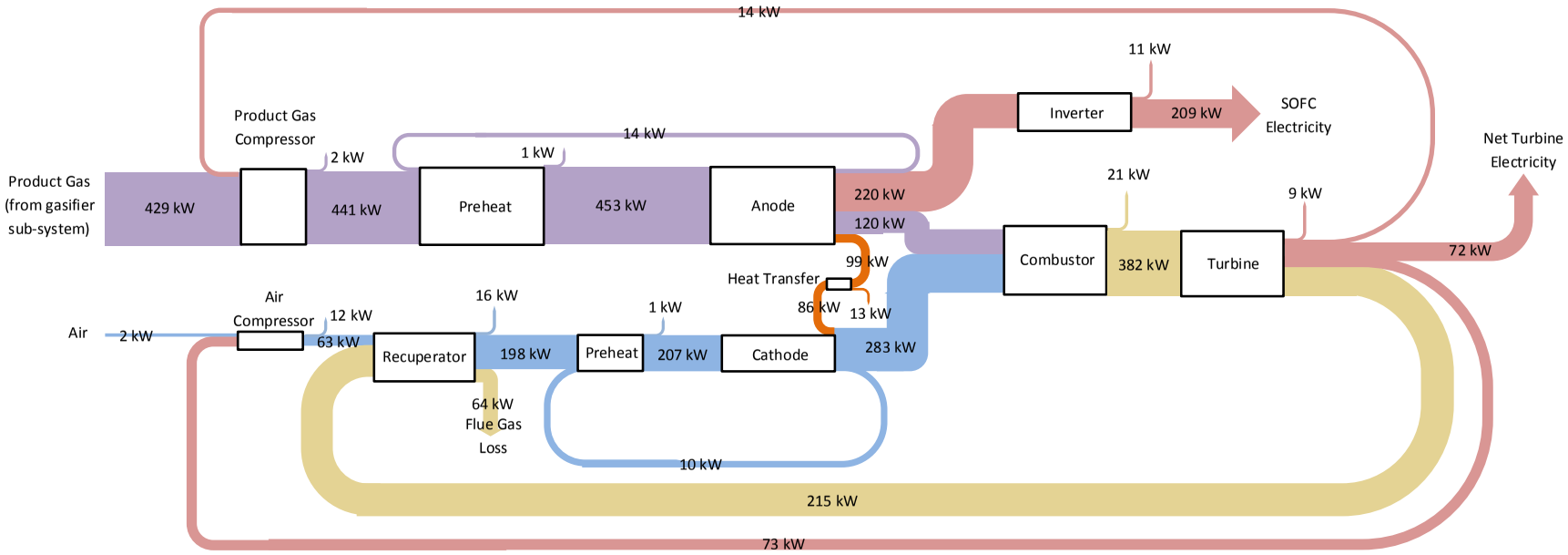

Figure 5.11: Exergy flow diagram for configuration 1 at optimum pressure

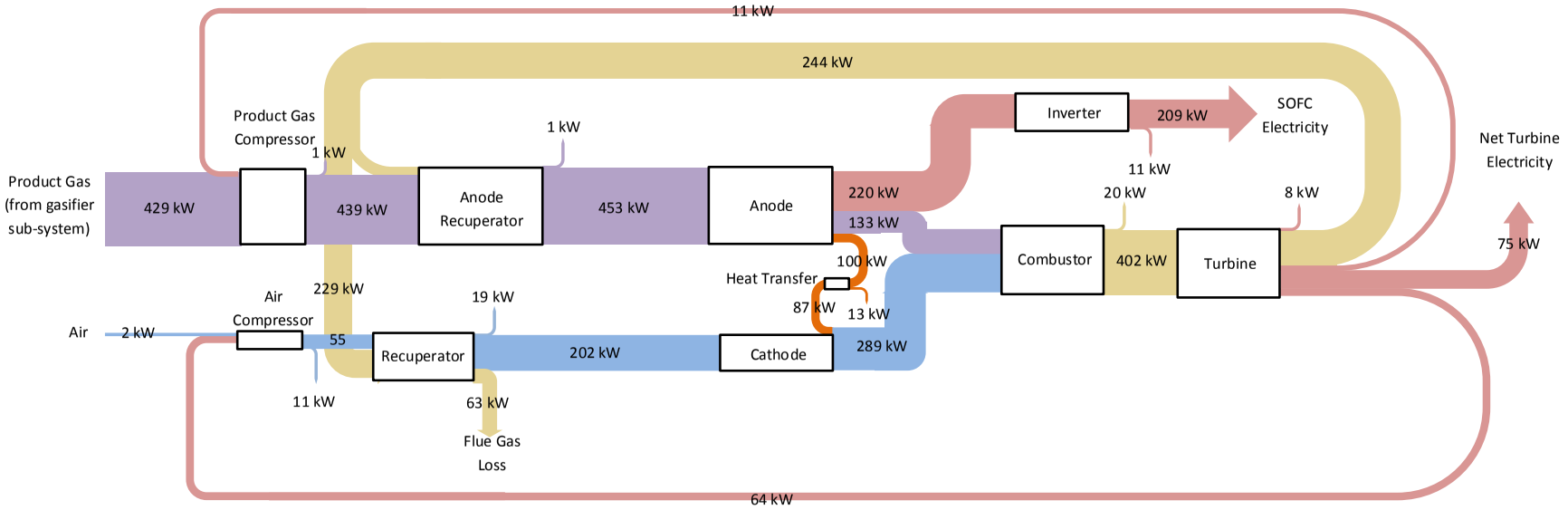

Figure 5.12: Exergy flow diagram for configuration 2 at optimum pressure

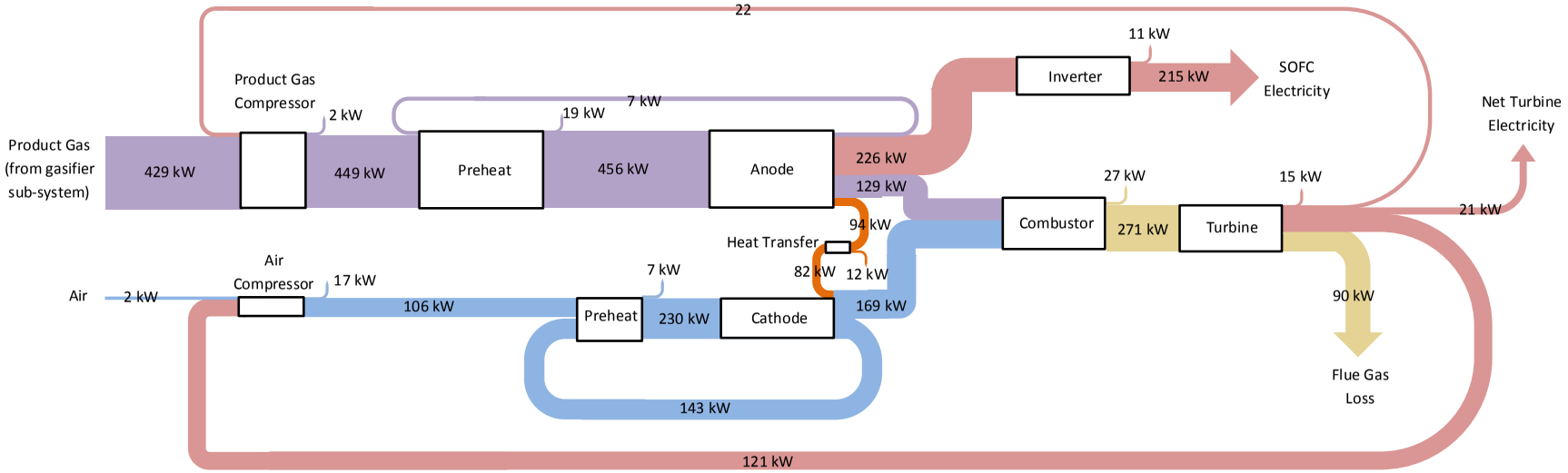

Figure 5.13: Exergy flow diagram for configuration 3 at optimum pressure

Table 5.6: Component exergy loss/destruction values and efficiency values for each configuration

Configuration	**1**	**2**	**3**
Component	**Exergy Loss/ Destruction [kW]**		
Flue gas	63.8	62.9	90.4
Air compressor	12.1	11.1	17.1
Fuel compressor	1.5	1.4	2.3
SOFC	12.8	12.9	12.4
Turbine	9.1	8.0	15.4
Anode heat exchanger (or recuperator)	1.4	1.4	0.5
Cathode heat exchanger	1.1	0.0	19.2
Inverter	11.0	11.0	11.3
Burner	20.6	19.7	26.9
Recuperator	15.5	19.0	0.0
Cathode heat exchanger & recuperator	15.5	19.0	19.2
Total	149.1	147.3	195.3
Total without flue gas	85.3	84.4	105
Efficiency metrics	**Efficiency [-]**		
$\eta_{\phi,SOFC,subsystem}$	0.6538	0.6579	0.5464
$\eta_{\phi,system}$	0.4616	0.4645	0.3857
Electricity Production/Exergy biomass	0.6239	0.6275	0.5017

The third configuration experiences significantly more exergy destruction within the components, most notably in the burner, air compressor, and turbine. The higher rates of destruction in the turbomachinery for configuration 3 are explained by the requirement of a larger pressure ratio, compared to the other two. The source of the higher rate of destruction in the burner can be found by examining the burner temperature in Table 5.5. It is important to note that the function of the burner is to convert chemical energy to thermal energy. While the exergy value of chemical energy is not dependent on temperature, this is not true for the exergy value of heat. Since the burner in configuration 3 operates at a much lower temperature, the chemical exergy is converted into lower thermal exergy, compared to the other configurations, increasing the rate of exergy destruction.

The above described conclusions are reinforced by what can be seen in Figures 5.11, 5.12, and 5.13. The higher compression ratio requires additional exergy to be returned from the turbine work for configuration 3, when compared to the other two. Additionally, the use of pre-heating by utilizing fuel cell exiting streams shows a decrease in exergy flow to the combustor, reducing the turbine output and recuperation exergy. This effect is very prominent in configuration 3, but can also clearly be seen in configuration 1. It is also important to note that heat transfer effects cause the air stream to rise in temperature. This is represented in the exergy flow from the anode to the cathode, where the high mass flow rate of the air maintains an operating temperature below threshold.

It is worth noting that the total system efficiency is somewhat low. This is due to the fact that there are several losses in the gasifier, causing the exergy loss/destruction in the gasifier sub-system to lower the performance of the overall system. However, this value is not readily comparable to other gasifier/SOFC systems, since it accounts for the solar thermal input, which is not a part of conventional systems. If an efficiency value is calculated relating the electricity production of the whole system to the biomass exergy input, a much higher value is attained.

While the performance of the solar gasifier cannot be directly compared in terms of solar efficiency for electricity production, it is important to note that the solar contribution is significant to the overall performance of the system. This is further discussed in Chapter 6.

6.0 CONCLUSIONS AND FUTURE WORK

6.1 CONCLUSIONS

This work examined current and predicted performance of several renewable energy technologies. A life cycle solar efficiency method was used to analyze and compare three very different renewable energy technologies (photovoltaic, solar thermal, biomass) to a typical coal power plant. This metric analyzed the efficiency with which sunlight is transformed to electricity, while accounting for the energy demands over the lifetime of a power plant. This analysis establishes a method to compare the technologies based on a matching type of input and output, identifying an equivalent measure of comparison. The process of photosynthesis for biomass and coal production was identified as a large source of energy loss.

The combination of photovoltaic and solar thermal energy production is then examined in further detail, showing increased performance, compared to the individual technologies operating separately. It is shown that this combination provides the highest benefits when used with photovoltaic cells that are able to maintain performance at high temperatures. While this technology is improving, it is still a more niche application, so it is also important to analyze combinations that are potentially more flexible and feasible to implement in the near-term.

Therefore, the combination of solar thermal and biomass gasification was then examined. For such a combination, the solar gasifier is the point where the two types of energy are combined into a synthesis/product gas. The gasifier examined in this investigation was a molten salt bubble column, which previously has not been examined using CFD analysis. The analysis examined a design of a vertical cylindrical cavity receiver with an absorber modeled as a thinner vertical tube positioned at the center of the receiver. A hydrodynamic and a

reaction kinetics study were carried out to establish behavior and identify the content of the output gases. With the gasifier behavior established, a power plant model was designed and examined based on exergetic performance. An SOFC with a micro-turbine sub-system was examined with three configurations to identify the highest performance. The performance of each configuration at various operating pressures yielded an optimum pressure for each configuration. The exergetic performance of the components was then analyzed and the total plant efficiency was established for each configuration. The benefit of the combination of energy sources is most clearly seen in the performance of the SOFC sub-system, where very high exergy efficiencies are observed due to the quality of the product gas.

The complete work allows us to examine the overall efficiency and impact of a variety of standalone and combined traditional and renewable energy systems. This knowledge can be used to inform policy decisions at a time when choices are being made that will affect our energy production and carbon emissions patterns for many years to come [222–224].

6.2 FUTURE WORK

There are several areas where additional studies would be beneficial. While the initial study of the total life cycle efficiency covered three energy technologies, the method can be expanded and applied to technologies, such as wind energy, hybrid power plants, such as the ones studied here, and other types of energy production. This would help establish a more comprehensive perspective of how energy conversion can be improved.

Further investigation of the combination of solar thermal and photovoltaic technology is required to acquire a more detailed understanding of the overall behavior. An investigation in heat transfer technology used for high concentration PV cells is needed to identify sources of energy and exergy loss as well as reliability and performance under varying solar input conditions.

There have been experimental studies on solar gasifiers, and a horizontal cavity receiver molten salt reactor was previously examined by another group [50]. However, these experiments do not shed light on the behavior of the hydrodynamics of the steam or CO_2

mixing and reacting with molten salt. This is important in validating the results of the CFD investigation above and establishing routes of improvement for newer technologies.

There is significant need for progress in many areas of research associated with renewable energy. While it is possible that a major breakthrough in any one type of renewable energy may lead that type to dominate the energy market, it is important to invest in various types of renewable energy until that occurs. This work has proven that hybridizing energy production from more than one source has many benefits, including efficiency and versatility gains. There are also secondary considerations, such as increased reliability and fuel geographic flexibility. Further investigation into the complex relationships between the various sources may show even more improved performance.

APPENDIX

UDF UTILIZED FOR HEAT FLUX

```
1 /* Wall Heat Generation Rate Profile UDF */
2
3 #include "udf.h"
4
5 DEFINE_PROFILE(wallheatgenerate,t,i)
6 {
7 real x[ND_ND];                    /* this will hold the position vector */
8 real y;
9 real z;
10 real j;
11 real q;
12   face_t f;
13
14   begin_f_loop(f,t)
15     {
16       F_CENTROID(x,f,t);
17       y = x[1];
18   z=x[0];
19   j=x[2];
20 /* Heat flux required to achieve 5kW total heat input */
21       q = 89782 - (y/0.3-1)*(y/0.3-1)*89782-
22     (2*asin(z/.075)/3.14159)*(2*asin(z/.075)/3.14159)*89782;
23   if (q>=0 && j>0)
24   F_PROFILE(f,t,i)=q;
25   else
26   F_PROFILE(f,t,i)=0;
27
28     }
29   end_f_loop(f,t)
30 }
```

BIBLIOGRAPHY

[1] International Energy Statistics, Electricity, Generation. http://www.eia.gov/cfapps/ipdbproject/IEDIndex3.cfm?tid=2&pid=2&aid=12.

[2] International Energy Outlook 2013. Technical report, U.S. Energy Information Administration, 2013.

[3] R. E. Blankenship, D. M. Tiede, J. Barber, G. W. Brudvig, G. Fleming, M. Ghirardi, M. R. Gunner, W. Junge, D. M. Kramer, A. Melis, T. A. Moore, C. C. Moser, D. G. Nocera, A. J. Nozik, D. R. Ort, W. W. Parson, R. C. Prince, and R. T. Sayre. Comparing photosynthetic and photovoltaic efficiencies and recognizing the potential for improvement. *Science*, 332(6031):805–809, may 2011.

[4] *Handbook of Chemistry and Physics; section 14: Geophysics, Astronomy, and Acoustics*. CRC Press., 2014.

[5] NREL (National Renewable Energy Laboratory): Dynamic maps, gis data, & analysis tools, 02 2015. http://www.nrel.gov/gis/solar.html.

[6] NREL: National center for photovoltaics. http://www.nrel.gov/ncpv/.

[7] Masakazu Ito, Kazuhiko Kato, Keiichi Komoto, Tetsuo Kichimi, and Kosuke Kurokawa. A comparative study on cost and life-cycle analysis for 100MW very large-scale PV (VLS-PV) systems in deserts using m-Si, a-Si, CdTe, and CIS modules. *PROGRESS IN PHOTOVOLTAICS: RESEARCH AND APPLICATIONS*, 16:17–30, 2008.

[8] N. J. Mohr, J. J. Schermer, M. A. J. Huijbregts, A. Meijer, and L. Reijnders. Life cycle assessment of thinfilm GaAs and GaInP/GaAs solar modules. *PROGRESS IN PHOTOVOLTAICS: RESEARCH AND APPLICATIONS*, 15:163–179, 2007.

[9] A. Meijer, M. A. J. Huijbregts, J. J. Schermer, and L. Reijnders. Life-cycle assessment of photovoltaic modules: Comparison of mc-Si, InGaP and InGaP/mc-Si solar modules. *PROGRESS IN PHOTOVOLTAICS: RESEARCH AND APPLICATIONS*, 11:275–287, 2003.

[10] K Nishioka, T Takamoto, T Agui, M Kaneiwa, Y Uraoka, and T Fuyuki. Annual output estimation of concentrator photovoltaic systems using high-efficiency InGaP/In-

GaAs/Ge triple-junction solar cells based on experimental solar cell's characteristics and field-test meteorological data. *Solar Energy Materials and Solar Cells*, 90:57–67, 2006.

[11] C. G. Zimmermann, C. Nmayr, M. Kolb, and A. Rucki. A mechanism of solar cell degradation in high intensity, high temperature space missions. *Progress in Photovoltaics: Research and Applications*, 21:420–435, 2011.

[12] Hiroyuki Toyota, Takaaki Iwai, Takanobu Shimada, Mitsuru Imaizumi, Koji Tanaka, and Michio Tajima. Degradation analysis of INGAP/GAAS/GE triple-junction solar cells in high-temperature and high-light-intensity environments by luminescence techniques. In *The twenty-ninth Space Energy Symposium*, 2010.

[13] T. Kerzmann and L. Schaefer. System simulation of a linear concentrating photovoltaic system with an active cooling system. *Renewable Energy*, 41:254–261, 2012.

[14] G. Kosmadakis, D. Manolakos, and G. Papadakis. Simulation and economic analysis of a CPV/thermal system coupled with an organic Rankine cycle for increased power generation. *Solar Energy*, 85:308–324, 2011.

[15] Abraham Kribus and Gur Mittelman. Potential of polygeneration with solar thermal and photovoltaic systems. *Journal of Solar Energy Engineering*, 130:011001, 2008.

[16] Gur Mittelman, Abraham Kribus, and Abraham Dayan. Solar cooling with concentrating photovoltaic/thermal (CPVT) systems. *Energy Conversion and Management*, 48:2481–2490, 2007.

[17] Gur Mittelman, Abraham Kribus, Ornit Mouchtar, and Abraham Dayan. Water desalination with concentrating photovoltaic/thermal (CPVT) systems. *Solar Energy*, 83:1322–1334, 2009.

[18] Concentrating solar power projects by project name. Available at http://www.nrel.gov/csp/solarpaces/by_project.cfm?print.

[19] Richard B. Diver and Timothy A. Moss. Practical field alignment of parabolic trough solar concentrators. *Journal of Solar Energy Engineering*, 129(2):153, 2007.

[20] Eckhard Lupfert, Andreas Neumann, Klaus-J. Riffelmann, and Steffen Ulmer. Comparative flux measurement and raytracing for the characterization of the focal region of solar parabolic trough collectors. In *Solar Energy*. ASME International, 2004.

[21] Eckhard Lupfert, Klaus Pottler, Steffen Ulmer, Klaus-J. Riffelmann, Andreas Neumann, and Bjorn Schiricke. Parabolic trough analysis and enhancement techniques. In *Solar Energy*. ASME International, 2005.

[22] C.E. Kennedy, R.V. Smilgys, D.A. Kirkpatrick, and J.S. Ross. Optical performance and durability of solar reflectors protected by an alumina coating. *Thin Solid Films*, 304(1-2):303–309, jul 1997.

[23] C. E. Kennedy and R. L. Swisher. Cost analysis of solar reflective hard-coat materials deposited by ion-beam-assisted deposition. *Journal of Solar Energy Engineering*, 127(2):270, 2005.

[24] Henry Price, Mary Jane Hale, Rod Mahoney, Carin Gummo, Robert Fimbres, and Robert Cipriani. Developments in high temperature parabolic trough receiver technology. In *Solar Energy*. ASME International, 2004.

[25] Henry Price, Russell Forristall, Timothy Wendelin, Allan Lewandowski, Timothy Moss, and Carin Gummo. Field survey of parabolic trough receiver thermal performance. In *Solar Energy*. ASME International, 2006.

[26] Ulf Herrmann and David W. Kearney. Survey of thermal energy storage for parabolic trough power plants. *Journal of Solar Energy Engineering*, 124(2):145, 2002.

[27] James E. Pacheco, Steven K. Showalter, and William J. Kolb. Development of a molten-salt thermocline thermal storage system for parabolic trough plants. *Journal of Solar Energy Engineering*, 124(2):153, 2002.

[28] Valentina A. Salomoni, Carmelo E. Majorana, Giuseppe M. Giannuzzi, Adio Miliozzi, Rosa Di Maggio, Fabrizio Girardi, Domenico Mele, and Marco Lucentini. Thermal storage of sensible heat using concrete modules in solar power plants. *Solar Energy*, 103:303–315, may 2014.

[29] Kinga Pielichowska and Krzysztof Pielichowski. Phase change materials for thermal energy storage. *Progress in Materials Science*, 65:67–123, aug 2014.

[30] T.E. Boukelia, M.S. Mecibah, B.N. Kumar, and K.S. Reddy. Optimization, selection and feasibility study of solar parabolic trough power plants for algerian conditions. *Energy Conversion and Management*, 101:450–459, sep 2015.

[31] T. Chambers, J. Raush, and B. Russo. Installation and operation of parabolic trough organic rankine cycle solar thermal power plant in south louisiana. *Energy Procedia*, 49:1107–1116, 2014.

[32] Ya-Ling He, Dan-Hua Mei, Wen-Quan Tao, Wei-Wei Yang, and Huai-Liang Liu. Simulation of the parabolic trough solar energy generation system with organic rankine cycle. *Applied Energy*, 97:630–641, sep 2012.

[33] Jurgen Dersch, Michael Geyer, Ulf Hermann, Scott A. Jones, Bruce Kelly, Rainer Kistner, Winfried Ortmanns, Robert Pitz-Paal, and Henry Price. Solar trough integration into combined cycle systems. In *Solar Energy*. ASME International, 2002.

[34] M. Eck and W.-D. Steinmann. Direct steam generation in parabolic troughs: First results of the DISS project. *Journal of Solar Energy Engineering*, 124(2):134, 2002.

[35] Loreto Valenzuela, Eduardo Zarza, Manuel Berenguel, and Eduardo F. Camacho. Control concepts for direct steam generation in parabolic troughs. *Solar Energy*, 78(2):301 – 311, 2005. {ISES} Solar World Congress 2003.

[36] L. Valenzuela, E. Zarza, M. Berenguel, and E.F. Camacho. Control scheme for direct steam generation in parabolic troughs under recirculation operation mode. *Solar Energy*, 80(1):1 – 17, 2006.

[37] Francisco J. Collado and Jesús Guallar. A review of optimized design layouts for solar power tower plants with campo code. *Renewable and Sustainable Energy Reviews*, 20:142–154, apr 2013.

[38] Matthew J. Emes, Maziar Arjomandi, and Graham J. Nathan. Effect of heliostat design wind speed on the levelised cost of electricity from concentrating solar thermal power tower plants. *Solar Energy*, 115:441–451, may 2015.

[39] Clifford K. Ho and Brian D. Iverson. Review of high-temperature central receiver designs for concentrating solar power. *Renewable and Sustainable Energy Reviews*, 29:835–846, jan 2014.

[40] P.J. Turner and C. Sansom. A tubed, volumetric cavity receiver concept for high efficiency, low-cost modular molten salt solar towers. *Energy Procedia*, 69:553–562, may 2015.

[41] Pablo Fernández and Fletcher J. Miller. Performance analysis and preliminary design optimization of a small particle heat exchange receiver for solar tower power plants. *Solar Energy*, 112:458–468, feb 2015.

[42] J. García-Barberena, A. Monreal, A. Mutuberria, and M. Sánchez. Towards cost-competitive solar towers – energy cost reductions based on decoupled solar combined cycles (DSCC). *Energy Procedia*, 49:1350–1360, 2014.

[43] J. Spelling, B. Laumert, and T. Fransson. Advanced hybrid solar tower combined-cycle power plants. *Energy Procedia*, 49:1207–1217, 2014.

[44] Scott M. Flueckiger, Brian D. Iverson, Suresh V. Garimella, and James E. Pacheco. System-level simulation of a solar power tower plant with thermocline thermal energy storage. *Applied Energy*, 113:86–96, jan 2014.

[45] Energy Efficiency Office of Utility Technologies and Renewable Energy. Renewable Energy Technology Characterizations, Report No.: TR-109496. Technical report, U.S. Department of Energy, 1997.

[46] M. Mann and P. Spath. A life cycle assessment of biomass cofiring in a coal-fired power plant. *Clean Products and Processes*, 3(2):81–91, jun 2001.

[47] Ion Iliuta, Arnaud Leclerc, and Façal Larachi. Allothermal steam gasification of biomass in cyclic multi-compartment bubbling fluidized-bed gasifier/combustor – new reactor concept. *Bioresource Technology*, 101(9):3194–3208, may 2010.

[48] Ajay Kumar, David D. Jones, and Milford A. Hanna. Thermochemical biomass gasification: A review of the current status of the technology. *Energies*, 2(3):556–581, jul 2009.

[49] Brandon J. Hathaway, Wojciech Lipiński, and Jane H. Davidson. Heat transfer in a solar cavity receiver: Design considerations. *Numerical Heat Transfer, Part A: Applications*, 62(5):445–461, sep 2012.

[50] B.J. Hathaway, D.B. Kittelson, and J.H. Davidson. Development of a molten salt reactor for solar gasification of biomass. *Energy Procedia*, 49:1950 – 1959, 2014. Proceedings of the SolarPACES 2013 International Conference.

[51] Rade Karamarkovic and Vladan Karamarkovic. Energy and exergy analysis of biomass gasification at different temperatures. *Energy*, 35(2):537 – 549, 2010. {ECOS} 2008 21st International Conference, on Efficiency, Cost, Optimization, Simulation and Environmental Impact of Energy Systems.

[52] K. Papadikis, A.V. Bridgwater, and S. Gu. CFD modelling of the fast pyrolysis of biomass in fluidised bed reactors, part a: Eulerian computation of momentum transport in bubbling fluidised beds. *Chemical Engineering Science*, 63(16):4218 – 4227, 2008.

[53] K. Papadikis, S. Gu, and A.V. Bridgwater. CFD modelling of the fast pyrolysis of biomass in fluidised bed reactors. part b: Heat, momentum and mass transport in bubbling fluidised beds. *Chemical Engineering Science*, 64(5):1036 – 1045, 2009.

[54] K. Papadikis, S. Gu, and A.V. Bridgwater. CFD modelling of the fast pyrolysis of biomass in fluidised bed reactors: Modelling the impact of biomass shrinkage. *Chemical Engineering Journal*, 149(13):417 – 427, 2009.

[55] BJ Hathaway, JH Davidson, and DB Kittelson. Solar gasification of biomass: Kinetics of pyrolysis and steam gasification in molten salt. *ASME. J. Sol. Energy Eng*, 133, 2011.

[56] Chen Hanping, Li Bin, Yang Haiping, Yang Guolai, and Zhang Shihong. Experimental investigation of biomass gasification in a fluidized bed reactor. *Energy & Fuels*, 22(5):3493–3498, sep 2008.

[57] Tao Song, Jiahua Wu, Laihong Shen, and Jun Xiao. Experimental investigation on hydrogen production from biomass gasification in interconnected fluidized beds. *Biomass and Bioenergy*, 36:258–267, jan 2012.

[58] O. Lucon A. Rahman J. Christensen F. Denton J. Fujino G. Heath S. Kadner M. Mirza H.Rudnick A. Schlaepfer A. Shmakin Sathaye, J. *IPCC Special Report on Renewable*

Energy Sources and Climate Change Mitigation, chapter Renewable Energy in the Context of Sustainable Development. Cambridge University Press, 2011.

[59] Yang Hu, Laura Schaefer, and Volker Hartkopt. Life cycle energy and exergy analysis for building cooling systems - a comparison between a solar driven absorption chiller and an electric driven chiller. In *Proceedings of the ASME 2011 5th International Conference on Energy Sustainability*, 2011.

[60] JeffreyS. Dukes. Burning buried sunshine: Human consumption of ancient solar energy. *Climatic Change*, 61(1-2):31–44, 2003.

[61] Xin-Guang Zhu, Stephen P. Long, and Donald R. Ort. Improving photosynthetic efficiency for greater yield. *Annual Review of Plant Biology*, 61(1):235–261, 2010. PMID: 20192734.

[62] Z. Dubinsky, T. Berner, and S. Aaronson. *Potential of large-scale algal culture for biomass and lipid production in arid lands*. Jan 1978.

[63] Ami Ben-Amotz and Mordhay Avron. The biotechnology of cultivating the halotolerant algadunaliella. *Trends in Biotechnology*, 8(0):121 – 126, 1990.

[64] Anastasios Melis. Solar energy conversion efficiencies in photosynthesis: Minimizing the chlorophyll antennae to maximize efficiency. *Plant Science*, 177(4):272 – 280, 2009.

[65] DavidAlan Walker. Biofuels, facts, fantasy, and feasibility. *Journal of Applied Phycology*, 21(5):509–517, 2009.

[66] Richard Petela. An approach to the exergy analysis of photosynthesis. *Solar Energy*, 82:311–328, 2008.

[67] D. Weibach, G. Ruprecht, A. Huke, K. Czerski abd S. Gottlieb, and A. Hussein. Energy intensities, EROIs (energy returned on invested), and energy payback times of electricity generating power plants. *Energy*, 52:210–221, 2013.

[68] Marc A Rosen. Energy- and exergy-based comparison of coal-fired and nuclear steam power plants. *Exergy, An International Journal*, 1(3):180 – 192, 2001.

[69] H.H. Erdem, A.V. Akkaya, B. Cetin, A. Dagdas, S.H. Sevilgen, B. Sahin, I. Teke, C. Gungor, and S. Atas. Comparative energetic and exergetic performance analyses for coal-fired thermal power plants in turkey. *International Journal of Thermal Sciences*, 48:2179–2186, 2009.

[70] Isam H. Aljundi. Energy and exergy analysis of a steam power plant in jordan. *Applied Thermal Engineering*, 29(23):324 – 328, 2009.

[71] Marc A Rosen and Ibrahim Dincer. Thermoeconomic analysis of power plants: an application to a coal fired electrical generating station. *Energy Conversion and Management*, 44(17):2743 – 2761, 2003.

[72] R. Jyothu. Naik, B. L. V. S. Gupta, and G. S. Sharma. Exergy analysis of 4.5mw biomass based steam power plant. *Journal of Humanities and Social Science*, 1:01–04, 2012.

[73] Maria Minguez, Angel Jimenez, Javier Rodriguez, Celina Gonzalez, Ignacio Lopez, and Rafael Nieto. Analysis of energetic and exergetic efficiency, and environmental benefits of biomass integrated gasification combined cycle technology. *Waste Manag Res*, 31:401, 2013.

[74] Abhishek Bhattacharya, Dulal Manna, Bireswar Paul, and Amitava Datta. Biomass integrated gasification combined cycle power generation with supplementary biomass firing: Energy and exergy based performance analysis. *Energy*, 36:2599–2610, 2011.

[75] Krzysztof J. Ptasinski, Mark J. Prins, and Anke Pierik. Exergetic evaluation of biomass gasification. *Energy*, 32(4):568 – 574, 2007. ECOS 05. 18th International Conference on Efficiency, Cost, Optimization, Simulation, and Environmental Impact of Energy Systems ECOS 05.

[76] Mark J. Prins, Krzysztof J. Ptasinski, and Frans J.J.G. Janssen. From coal to biomass gasification: Comparison of thermodynamic efficiency. *Energy*, 32(7):1248 – 1259, 2007.

[77] Narendra Singh, S.C. Kaushik, and R.D. Misra. Exergetic analysis of a solar thermal power system. *Renewable Energy*, 19(12):135 – 143, 2000.

[78] A. Baghernejad and M. Yaghoubi. Exergy analysis of an integrated solar combined cycle system. *Renewable Energy*, 35(10):2157 – 2164, 2010.

[79] V. Siva Reddy, S.C. Kaushik, and S.K. Tyagi. Exergetic analysis and performance evaluation of parabolic trough concentrating solar thermal power plant (PTCSTPP). *Energy*, 39(1):258 – 273, 2012. Sustainable Energy and Environmental Protection 2010.

[80] P.E. Timothy J. Skone. Role of alternative energy sources: Solar thermal technology assessment. Technical report, National Energy Technology Laboratory, 2012.

[81] Yolanda Lechon, Cristina de la Rua, and Rosa Saez. Life cycle environmental impacts of electricity production by solarthermal power plants in spain. *Journal of Solar Energy Engineering*, 130:021012, 2008.

[82] Peter Viebahn. Sokrates-projekt, solarthermische kraftwerkestechnologies fr den schutz des erdkimas, a. p.2.2. Technical report, Deutsches Zentrum fr Luft- und Raumfahrt Stuttgart.

[83] Imad Eddine Meriche, Abdelhadi Baghidja, and Taqiy Eddine Boukelia. Design and performance evaluation of solar gas turbine power plant in south western algeria. *INTERNATIONAL JOURNAL Of RENEWABLE ENERGY RESEARCH*, 4, 2014.

[84] V. Siva Reddy, S. C. Kaushik, and S. K. Tyagi. Exergetic analysis and economic evaluation of central tower receiver solar thermal power plant. *International Journal of Energy Research*, pages n/a–n/a, 2013.

[85] Niels Jungbluth. Life cycle assessment of crystalline photovoltaics in the swiss ecoinvent database. *PROGRESS IN PHOTOVOLTAICS: RESEARCH AND APPLICATIONS*, (in press).

[86] Pamela L. Spath, Margaret K. Mann, and Dawn R. Kerr. Life cycle assessment of coal-fired power production. Technical report, National Renewable Energy Laboratory, 1999.

[87] Marco Raugei, Pere Fullana i Palmer, and Vasilis Fthenakis. The energy return on energy investment (EROI) of photovoltaics: Methodology and comparisons with fossil fuel life cycles. *Energy Policy*, 45:576–582, jun 2012.

[88] Yan Hu, Charles A.S. Hall, Jianliang Wang, Lianyong Feng, and Alexandre Poisson. Energy return on investment (EROI) of china's conventional fossil fuels: Historical and future trends. *Energy*, 54:352–364, jun 2013.

[89] Angelantonio Rafaschieri, Mario Rapaccini, and Giampaolo Manfrida. Life cycle assessment of electricity production from poplar energy crops compared with conventional fossil fuels. *Energy Conversion and Management*, 40(14):1477 – 1493, 1999.

[90] M.K. Mann, P.L. Spath, and National Renewable Energy Laboratory (U.S.). *Life Cycle Assessment of a Biomass Gasification Combined-cycle Power System*. National Renewal Energy Laboratory, 1997.

[91] Martin C Heller, Gregory A Keoleian, Margaret K Mann, and Timothy A Volk. Life cycle energy and environmental benefits of generating electricity from willow biomass. *Renewable Energy*, 29(7):1023 – 1042, 2004.

[92] Martin C Heller, Gregory A Keoleian, and Timothy A Volk. Life cycle assessment of a willow bioenergy cropping system. *Biomass and Bioenergy*, 25(2):147 – 165, 2003.

[93] Inge Vande Walle, Nancy Van Camp, Liesbet Van de Casteele, Kris Verheyen, and Raoul Lemeur. Short-rotation forestry of birch, maple, poplar and willow in flanders (belgium) ii. energy production and CO2 emission reduction potential. *Biomass and Bioenergy*, 31(5):276 – 283, 2007.

[94] David Styles and Michael B. Jones. Energy crops in ireland: Quantifying the potential life-cycle greenhouse gas reductions of energy-crop electricity. *Biomass and Bioenergy*, 31(1112):759 – 772, 2007.

[95] Pietro Goglio and Philip M.O. Owende. A screening LCA of short rotation coppice willow (Salix sp.) feedstock production system for small-scale electricity generation. *Biosystems Engineering*, 103(3):389 – 394, 2009.

[96] Meimei Zhang, Zhifeng Wang, Chao Xu, and Hui Jiang. Embodied energy and emergy analyses of a concentrating solar power (csp) system. *Energy Policy*, 42(0):232 – 238, 2012.

[97] Sylvestre Njakou Djomo, Ouafik El Kasmioui, and Reinhart Ceulemans. Energy and greenhouse gas balance of bioenergy production from poplar and willow: a review. *GCB Bioenergy*, 3(3):181–197, 2011.

[98] H.D. Madhawa Hettiarachchi, Mihajlo Golubovic, William M. Worek, and Yasuyuki Ikegamib. Optimum design criteria for an Organic Rankine cycle using low-temperature geothermal heat sources. *Energy*, 32:1698–1706, 2007.

[99] Dongxiang Wang, Xiang Ling, Hao Peng, Lin Liu, and LanLan Tao. Efficiency and optimal performance evaluation of organic Rankine cycle for low grade waste heat power generation. *Energy*, 50:343–352, 2013.

[100] Kalyan K. Srinivasan, Pedro J. Mago, and Sundar R. Krishnan. Analysis of exhaust waste heat recovery from a dual fuel low temperature combustion engine using an Organic Rankine Cycle. *Energy*, 35:2387–2399, 2010.

[101] Enhua Wang, Hongguang Zhang, Boyuan Fan, and Yuting Wu. Optimized performances comparison of organic Rankine cycles for low grade waste heat recovery. *Journal of Mechanical Science and Technology*, 26:2301–2312, 2012.

[102] Jiangfeng Wang, Zhequan Yan, Man Wang, Shaolin Ma, and Yiping Dai. Thermodynamic analysis and optimization of an (organic Rankine cycle) ORC using low grade heat source. *Energy*, 49:256–265, 2013.

[103] Fredy Velez, Jose J. Segovia, M. Carmen Martn, Gregorio Antolin, Farid Chejne, and Ana Quijano. Comparative study of working fluids for a Rankine cycle operating at low temperature. *Fuel Processing Technology*, 103:71–77, 2012.

[104] Ali Vatani, Ali Khazaeli, Ramin Roshandel, and Mohammad Hassan Panjeshahi. Thermodynamic analysis of application of organic Rankine cycle for heat recovery from an integrated DIR-MCFC with pre-reformer. *Energy Conversion and Management*, 67:197–207, 2013.

[105] Agustin M. Delgado-Torres and Lourdes Garcia-Rodriguez. Analysis and optimization of the low-temperature solar organic Rankine cycle (ORC). *Energy Conversion and Management*, 51:2846–2856, 2010.

[106] Huijuan Chen, D. Yogi Goswami, and Elias K. Stefanakos. A review of thermodynamic cycles and working fluids for the conversion of low-grade heat. *Renewable and Sustainable Energy Reviews*, 14:3059–3067, 2010.

[107] Chiranjeev Kalra, Guillaume Becquin, Jennifer Jackson, Anna Lis Laursen, Huijuan Chen, Kevin Myers, Alicia Hardy, Helge Klockow, and Jalal Zia. High-potential work-

ing fluids and cycle concepts for next generation binary organic rankine cycle for enhanced geothermal systems. In *Thirty-Seventh Workshop on Geothermal Reservoir Engineering*, 2012.

[108] Bahaa Saleh, Gerald Koglbauer, Martin Wendland, and Johann Fischer. Working fluids for low-temperature organic Rankine cycles. *Energy*, 32:1210–1221, 2007.

[109] A. Schuster, S. Karellas, and R. Aumann. Efficiency optimization potential in supercritical Organic Rankine Cycles. *Energy*, 35:1033–1039, 2010.

[110] Tao Guo, HuaiXin Wang, and ShengJun Zhang. Comparative analysis of CO2-based transcritical Rankine cycle and HFC245fa-based subcritical organic Rankine cycle using low-temperature geothermal source. *Sci China Tech Sci*, 53:1638–1646, 2010.

[111] Tao Guo, Huaixin Wang, and Shengjun Zhang. Comparative analysis of natural and conventional working fluids for use in transcritical Rankine cycle using low-temperature geothermal source. *Internation Journal of Energy Research*, 35:530–544, 2011.

[112] Tony Ho, Samuel S. Mao, and Ralph Greif. Increased power production through enhancements to the Organic Flash Cycle (OFC). *Energy*, 45:686–695, 2012.

[113] Tony Ho. *Advanced Organic Vapor Cycles for Improving Thermal Conversion Efficiency in Renewable Energy Systems*. PhD thesis, University of California, Berkeley, 2012.

[114] Xiaojun Shi and Defu Che. A combined power cycle utilizing low-temperature waste heat and LNG cold energy. *Energy Conversion and Management*, 50:567–575, 2009.

[115] James Freeman, Klaus Hellgardt, and Christos N. Markides. An assessment of solar-powered organic rankine cycle systems for combined heating and power in UK domestic applications. *Applied Energy*, 138:605 – 620, 2015.

[116] Van Long Le, Abdelhamid Kheiri, Michel Feidt, and Sandrine Pelloux-Prayer. Thermodynamic and economic optimizations of a waste heat to power plant driven by a subcritical ORC (organic rankine cycle) using pure or zeotropic working fluid. *Energy*, 78:622 – 638, 2014.

[117] Ata D. Akbari and Seyed M.S. Mahmoudi. Thermoeconomic analysis & optimization of the combined supercritical CO2 (carbon dioxide) recompression Brayton/organic Rankine cycle. *Energy*, 78:501 – 512, 2014.

[118] A. Borsukiewicz-Gozdur, S. Winiewski, S. Mocarski, and M. Bakowski. ORC power plant for electricity production from forest and agriculture biomass. *Energy Conversion and Management*, 87:1180 – 1185, 2014.

[119] Annamaria Buonomano, Francesco Calise, Adolfo Palombo, and Maria Vicidomini. Energy and economic analysis of geothermalsolar trigeneration systems: A case study for a hotel building in ischia. *Applied Energy*, 138:224 – 241, 2015.

[120] A. Al-Alili, Y. Hwang, R. Radermacher, and I. Kubo. A high effciency solar air conditioner using concentrating photovoltaic/thermal collectors. *Applied Energy*, 93:138–147, 2012.

[121] Francesco Calise, Massimo Dentice dAccadia, and Laura Vanoli. Design and dynamic simulation of a novel solar trigeneration system based on hybrid photovoltaic/thermal collectors (PVT). *Energy Conversion and Management*, 60:214 – 225, 2012. Special issue of Energy Conversion and Management dedicated to ECOS 2011 - the 24th International Conference on Efficiency, Costs, Optimization, Simulation and Environmental Impact of Energy Systems.

[122] Priyanka Singh and N.M.Ravindra. Temperature dependence of solar cell performancean analysis. *Solar Energy Materials & Solar Cells*, 101:36–45, 2012.

[123] Bahram Saadatfar, Reza Fakhrai, and Torsten Fransson. Thermodynamic vapor cycles for converting low- to medium-grade heat to power: A state-of-the-art review and future research pathways. *The Journal of MacroTrends in Energy and Sustainability*, 2, 2014.

[124] S. A. Klein. Engineering Equation Solver (EES) v9.715-3d (08/09/14).

[125] Wilbur A. Affens. Flammability Properties of Hydrocarbon Fuels. Interrelations of Flammability Properties of n-Alkanes in Air. *Journal of Chemical & Engineering Data*, 11(2):197–202, 1966.

[126] Environmental Protection Agency. Code of Federal Regulations (annual edition), Title 40 - Protection of Environment, Part 82 - Protection of Stratospheric Ozone. Technical report, 1992.

[127] Ozone Secretariat United Nations Environment Programme. The Montreal Protocol on Substances that Deplete the Ozone Layer. Technical report, 2000.

[128] P. Forster, V. Ramaswamy, P. Artaxo, T. Berntsen, R. Betts, D.W. Fahey, J. Haywood, J. Lean, D.C. Lowe, G. Myhre, J. Nganga, R. Prinn, G. Raga, M. Schulz, and R. Van Dorland. *Climate Change 2007: The Physical Science Basis. Contribution of Working Group I to the Fourth Assessment Report of the Intergovernmental Panel on Climate Change*, chapter 2: Changes in Atmospheric Constituents and in Radiative Forcing, pages 131–217. Cambridge University Press, 2007.

[129] J.S. Daniel, G.J.M. Velders (Lead Authors), A.R. Douglass, P.M.D. Forster, D.A. Hauglustaine, I.S.A. Isaksen, L.J.M. Kuijpers, A. McCulloch, and T.J. Wallington. *Scientific Assessment of Ozone Depletion: 2006*, chapter 8: Halocarbon scenarios, ozone depletion potentials, and global warming potentials, page 572. World Meteorological Organization, 2007.

[130] Guus J.M. Velders, Sasha Madronich, Cathy Clerbaux, Richard Derwent, Michel Grutter, Didier Hauglustaine, Selahattin Incecik, Malcolm Ko, Jean-Marie Libre, Ole John

Nielsen, Frode Stordal, and Tong Zhu. *IPCC/TEAP Special Report: Safeguarding the Ozone Layer and the Global Climate System: Issues Related to Hydrofluorocarbons and Perfluorocarbons ("SROC")*, chapter 2: Chemical and Radiative Effects of Halocarbons and Their Replacement Compounds, pages 133–180. World Meteorological Organization, 2005.

[131] D.L. Albritton, L.G. Meira Filho, U. Cubasch, X. Dai, Y. Ding, D.J. Griggs, B. Hewitson, J.T. Houghton, I. Isaksen, T. Karl, M. McFarland, V.P. Meleshko, J.F.B. Mitchell, M. Noguer, M. Oppenheimer B.S. Nyenzi, J.E. Penner, S. Pollonais, T. Stocker, and K.E. Trenberth. *Climate Change 2001: The Scientific Basis. Contribution of Working Group I to the Third Assessment Report of the Intergovernmental Panel on Climate Change*, chapter Technical Summary of the Working Group I Report, pages 21–84. Cambridge University Press, 2001.

[132] S.A. Montzka, J.H. Butler P.J. Fraser (Lead Authors), P.S. Connell, D.M. Cunnold, J.S. Daniel, R.G. Derwent, S. Lal, A. McCulloch, D.E. Oram, C.E. Reeves, E. Sanhueza, L.P. Steele, G.J.M. Velders, R.F. Weiss, and R.J. Zander. *Scientific Assessment of Ozone Depletion: 2002*, chapter 1: Controlled Substances and Other Source Gases,. World Meteorological Organization, 2003.

[133] Yingwen Wu, Xiangfei Liang, Xiaoping Tu, and Rong Zhuang. Study of R161 refrigerant for residential air-conditioning applications. In *International Refrigeration and Air Conditioning Conference at Purdue, July 16-19, 2012*.

[134] Alexandre J. Grebenkov, Ryan Hulse, Hang Pham, and Rajiv Singh. Physical properties and equation of state for trans-1,3,3,3-tetrafluoropropene. In *3rd IIR Conference on Thermophysical Properties and Transfer Processes of Refrigerants*, 2009.

[135] D.W. Gregg, R.W. Taylor, J.H. Campbell, J.R. Taylor, and A. Cotton. Solar gasification of coal, activated carbon, coke and coal and biomass mixtures. *Solar Energy*, 25(4):353 – 364, 1980.

[136] Jean P. Murray and Edward A. Fletcher. Reaction of steam with cellulose in a fluidized bed using concentrated sunlight. *Energy*, 19(10):1083 – 1098, 1994.

[137] A ZGRAGGEN, P HAUETER, D TROMMER, M ROMERO, J DEJESUS, and A STEINFELD. Hydrogen production by steam-gasification of petroleum coke using concentrated solar power—II reactor design, testing, and modeling. *International Journal of Hydrogen Energy*, 31(6):797–811, may 2006.

[138] P Lichty, C Perkins, B Woodruff, C Bingham, and A Weimer. Rapid high temperature solar thermal biomass gasification in a prototype cavity reactor. *ASME. J. Sol. Energy Eng.*, 132, 2010.

[139] Brandon J. Hathaway, Masanori Honda, David B. Kittelson, and Jane H. Davidson. Steam gasification of plant biomass using molten carbonate salts. *Energy*, 49:211 – 217, 2013.

[140] R Adinberg, M Epstein, and J Karni. Solar gasification of biomass: A molten salt pyrolysis study. *ASME. J. Sol. Energy Eng.*, 126:850–857, 2004.

[141] Q. Xue, T.J. Heindel, and R.O. Fox. A CFD model for biomass fast pyrolysis in fluidized-bed reactors. *Chemical Engineering Science*, 66(11):2440 – 2452, 2011.

[142] Q. Xue and R.O. Fox. Multi-fluid CFD modeling of biomass gasification in polydisperse fluidized-bed gasifiers. *Powder Technology*, 254:187 – 198, 2014.

[143] K.D. Kafui, C. Thornton, and M.J. Adams. Discrete particle-continuum fluid modelling of gas–solid fluidised beds. *Chemical Engineering Science*, 57(13):2395–2410, jul 2002.

[144] Xiaoke Ku, Tian Li, and Terese Løvås. CFD–DEM simulation of biomass gasification with steam in a fluidized bed reactor. *Chemical Engineering Science*, 122:270–283, jan 2015.

[145] D. Darmana, N.G. Deen, and J.A.M. Kuipers. Detailed modeling of hydrodynamics, mass transfer and chemical reactions in a bubble column using a discrete bubble model. *Chemical Engineering Science*, 60(12):3383 – 3404, 2005.

[146] Brandon J. Hathaway. *Solar Gasification of Biomass: Design and Characterization of a Molten Salt Gasification Reactor*. PhD thesis, University of Minnesota, 2013.

[147] Janna Martinek, Carl Bingham, and Alan W. Weimer. Computational modeling and on-sun model validation for a multiple tube solar reactor with specularly reflective cavity walls. part 1: Heat transfer model. *Chemical Engineering Science*, 81:298–310, oct 2012.

[148] Janna Martinek, Carl Bingham, and Alan W. Weimer. Computational modeling of a multiple tube solar reactor with specularly reflective cavity walls. part 2: Steam gasification of carbon. *Chemical Engineering Science*, 81:285–297, oct 2012.

[149] Janna Martinek and Alan W. Weimer. Evaluation of finite volume solutions for radiative heat transfer in a closed cavity solar receiver for high temperature solar thermal processes. *International Journal of Heat and Mass Transfer*, 58(1-2):585–596, mar 2013.

[150] Janna Martinek and Alan W. Weimer. Design considerations for a multiple tube solar reactor. *Solar Energy*, 90:68–83, apr 2013.

[151] Janna Martinek, Rachel Viger, and Alan W. Weimer. Transient simulation of a tubular packed bed solar receiver for hydrogen generation via metal oxide thermochemical cycles. *Solar Energy*, 105:613–631, jul 2014.

[152] Andrey A. Troshko and Franz Zdravistch. CFD modeling of slurry bubble column reactors for fisher–tropsch synthesis. *Chemical Engineering Science*, 64(5):892–903, mar 2009.

[153] K. Ekambara and M.T. Dhotre. CFD simulation of bubble column. *Nuclear Engineering and Design*, 240(5):963–969, may 2010.

[154] Cédric Laborde-Boutet, Faiçal Larachi, Nicolas Dromard, Olivier Delsart, and Daniel Schweich. CFD simulation of bubble column flows: Investigations on turbulence models in RANS approach. *Chemical Engineering Science*, 64(21):4399–4413, nov 2009.

[155] Victor Yakhot and Steven A. Orszag. Renormalization group analysis of turbulence. I. Basic theory. *Journal of Scientific Computing*, 1(1):3–51, 1986.

[156] P. Chen, M. P. Dudukovi, and J. Sanyal. Three-dimensional simulation of bubble column flows with bubble coalescence and breakup. *AIChE Journal*, 51(3):696–712, 2005.

[157] P. Chen, J. Sanyal, and M.P. Dudukovic. CFD modeling of bubble columns flows: implementation of population balance. *Chemical Engineering Science*, 59(22-23):5201–5207, nov 2004.

[158] P. Chen, J. Sanyal, and M.P. Duduković. Numerical simulation of bubble columns flows: effect of different breakup and coalescence closures. *Chemical Engineering Science*, 60(4):1085–1101, feb 2005.

[159] Eizo Sada, Shigeo Katoh, Hidehumi Yoshii, Toshihiko Yamanishi, and Akio Nakanishi. Performance of the gas bubble column in molten salt systems. *Industrial & Engineering Chemistry Process Design and Development*, 23(1):151–154, jan 1984.

[160] Yong-Jun Cho, Hee-Chul Yang, Hee-Chul Eun, Jae-Hyung Yoo, and Joon-Hyung Kim. Hydrodynamic and gas phase axial dispersion in an air-molten salt two-phase system (molten salt oxidation reactor). *Chemical Engineering and Processing: Process Intensification*, 44(10):1054–1062, oct 2005.

[161] T.A Nijhuis, S Musch, M Makkee, and J.A Moulijn. The direct epoxidation of propene by molten salts. *Applied Catalysis A: General*, 196(2):217–224, apr 2000.

[162] Mandar V. Tabib, Swarnendu A. Roy, and Jyeshtharaj B. Joshi. CFD simulation of bubble column—an analysis of interphase forces and turbulence models. *Chemical Engineering Journal*, 139(3):589–614, jun 2008.

[163] A. Sokolichin, G. Eigenberger, and A. Lapin. Simulation of buoyancy driven bubbly flow: Established simplifications and open questions. *AIChE Journal*, 50(1):24–45, jan 2004.

[164] K. Ekambara and J.B. Joshi. CFD simulation of mixing and dispersion in bubble columns. *Chemical Engineering Research and Design*, 81(8):987–1002, sep 2003.

[165] T. Takamasa and A. Tomiyama. Three-Dimensional Gas-Liquid Two-Phase Bubbly Flow in a C-Shaped Tube. In *Ninth International Topical Meeting on Nuclear Reactor Thermal Hydraulics (NURETH-9)*, 1999.

[166] F.J. Moraga, F.J. Bonetto, and R.T. Lahey. Lateral forces on spheres in turbulent uniform shear flow. *International Journal of Multiphase Flow*, 25(6-7):1321–1372, sep 1999.

[167] Renwei Mei and J.F. Klausner. Shear lift force on spherical bubbles. *International Journal of Heat and Fluid Flow*, 15(1):62–65, feb 1994.

[168] STRUGGLE WITH COMPUTATIONAL BUBBLE DYNAMICS. *Multiphase Science and Technology*, 10(4):369–405, 1998.

[169] R.M.A. Masood and A. Delgado. Numerical investigation of the interphase forces and turbulence closure in 3d square bubble columns. *Chemical Engineering Science*, 108:154–168, apr 2014.

[170] R.M.A. Masood, C. Rauh, and A. Delgado. CFD simulation of bubble column flows: An explicit algebraic reynolds stress model approach. *International Journal of Multiphase Flow*, 66:11–25, nov 2014.

[171] Liang Yu, Jing Lu, Xiangping Zhang, and Suojiang Zhang. Numerical simulation of the bubbling fluidized bed coal gasification by the kinetic theory of granular flow (KTGF). *Fuel*, 86(5-6):722–734, mar 2007.

[172] Juhui Chen, Guangbin Yu, Bing Dai, Di Liu, and Lei Zhao. CFD simulation of a bubbling fluidized bed gasifier using a bubble-based drag model. *Energy & Fuels*, 28(10):6351–6360, oct 2014.

[173] Wang Shuai, Lu Huang, Hao Zhenhua, Lu Huilin, Liu Guodong, Li Dan, and Zhao Feixiang. Numerical modeling of a bubbling fluidized bed coal gasifier by kinetic theory of rough spheres. *Fuel*, 130:197–202, aug 2014.

[174] Qi Miao, Jesse Zhu, Shahzad Barghi, Chuangzhi Wu, Xiuli Yin, and Zhaoqiu Zhou. Modeling biomass gasification in circulating fluidized beds. *Renewable Energy*, 50:655–661, feb 2013.

[175] Zhongyi Deng, Rui Xiao, Baosheng Jin, He Huang, Laihong Shen, Qilei Song, and Qianjun Li. Computational fluid dynamics modeling of coal gasification in a pressurized spout-fluid bed. *Energy & Fuels*, 22(3):1560–1569, may 2008.

[176] Niels Gerbrand Deen. *An Experimental and Computational Study of Fluid Dynamics in Gas-Liquid Chemical Reactors*. PhD thesis, Esbjerg Institute of Technology, 2001.

[177] Muhammad Abid Akhtar, Moses Oludayo Tadé, and Vishnu Kumar Pareek. Two-fluid eulerian simulation of bubble column reactors with distributors. *J. Chem. Eng. Japan / JCEJ*, 39(8):831–841, 2006.

[178] S. H. White. The behavior of water in molten salts. *Journal of The Electrochemical Society*, 134(5):1080, 1987.

[179] Bernard J. Wood and Kenneth M. Sancier. The mechanism of the catalytic gasification of coal char: A critical review. *Catalysis Reviews*, 26(2):233–279, jun 1984.

[180] M Mnguez, A Jimnez, J Rodrguez, C Gonzlez, I Lpez, and R Nieto. Analysis of energetic and exergetic efficiency, and environmental benefits of biomass integrated gasification combined cycle technology. *Waste Manag Res*, 4:101–412, 2013.

[181] Farrukh Khalid, Ibrahim Dincer, and Marc A. Rosen. Energy and exergy analyses of a solar-biomass integrated cycle for multigeneration. *Solar Energy*, 112:290 – 299, 2015.

[182] Ashok A. Kaniyal, Philip J. van Eyk, and Graham J. Nathan. Dynamic modeling of the coproduction of liquid fuels and electricity from a hybrid solar gasifier with various fuel blends. *Energy & Fuels*, 27(6):3556–3569, 2013.

[183] Murat Ozturk and Ibrahim Dincer. Thermodynamic assessment of an integrated solar power tower and coal gasification system for multi-generation purposes. *Energy Conversion and Management*, 76:1061 – 1072, 2013.

[184] S. Karellas, J. Karl, and E. Kakaras. An innovative biomass gasification process and its coupling with microturbine and fuel cell systems. *Energy*, 33(2):284 – 291, 2008. 19th International Conference on Efficiency, Cost, Optimization, Simulation and Environmental Impactof Energy SystemsECOS 2006.

[185] Wayne Doherty, Anthony Reynolds, and David Kennedy. Computer simulation of a biomass gasification-solid oxide fuel cell power system using aspen plus. *Energy*, 35(12):4545 – 4555, 2010. The 3rd International Conference on Sustainable Energy and Environmental Protection, SEEP 2009.

[186] C. Bang-Møller, M. Rokni, and B. Elmegaard. Exergy analysis and optimization of a biomass gasification, solid oxide fuel cell and micro gas turbine hybrid system. *Energy*, 36(8):4740–4752, aug 2011.

[187] L. Fryda, K.D. Panopoulos, and E. Kakaras. Integrated CHP with autothermal biomass gasification and SOFC–MGT. *Energy Conversion and Management*, 49(2):281–290, feb 2008.

[188] P. Schwarzboezl. *A TRNSYS Model Library for Solar Thermal Electric Components (STEC). Reference Manual. Release 3.0*, November 2006.

[189] M. C. Stoddard, S. E. Faas, C. J. Chiang, and J. A. Dirks. Solergy - a computer code for calculating the annual energy from central receiver power plants. Technical report, Sandia National Laboratories, 1987.

[190] R. Pitz-Paal, J. Dersch, A. Ferriere and M. Romero , B. Milow and, A. Steinfeld and U. Langnickel and E. Shpilrain and O. Popel and M. Epstein F. Tellez, and, and J. Karni. European concentrated solar thermal road-mapping ECOSTAR road map document. Technical report, Deutsches Zentrum fur Luft- und Raumfahrt e.V., 2005.

[191] Pierre Garcia, Alain Ferriere, and Jean-Jacques Bezian. Codes for solar flux calculation dedicated to central receiver system applications: A comparative review. *Solar Energy*, 82(3):189–197, mar 2008.

[192] Marcelino Sánchez and Manuel Romero. Methodology for generation of heliostat field layout in central receiver systems based on yearly normalized energy surfaces. *Solar Energy*, 80(7):861–874, jul 2006.

[193] Francisco J. Collado. Quick evaluation of the annual heliostat field efficiency. *Solar Energy*, 82(4):379–384, apr 2008.

[194] F.J. Collado, A. Gómez, and J.A. Turégano. An analytic function for the flux density due to sunlight reflected from a heliostat. *Solar Energy*, 37(3):215–234, 1986.

[195] F.W. Lipps and L.L. Vant-Hull. A cellwise method for the optimization of large central receiver systems. *Solar Energy*, 20(6):505–516, 1978.

[196] F. W. Lipps. Theory of cellwise optimization for solar central receiver systems. Technical report, Houston Univ., TX (USA). Energy Lab., 1985.

[197] J. R. Howell. The monte carlo method in radiative heat transfer. *ASME. J. Heat Transfer*, 120:547–560, 1998.

[198] Rubén Gil, Carlos Monné, Nuria Bernal, Mariano Muñoz, and Francisco Moreno. Thermal model of a dish stirling cavity-receiver. *Energies*, 8(2):1042–1057, jan 2015.

[199] Sönke H. Teichel, Lukas Feierabend, Sanford A. Klein, and Douglas T. Reindl. An alternative method for calculation of semi-gray radiation heat transfer in solar central cavity receivers. *Solar Energy*, 86(6):1899–1909, jun 2012.

[200] Guohui Song, Laihong Shen, and Jun Xiao. Estimating specific chemical exergy of biomass from basic analysis data. *Industrial & Engineering Chemistry Research*, 50(16):9758–9766, aug 2011.

[201] Ryan P O'Hayre, Suk-Won Cha, Whitney Colella, and Fritz B Prinz. *Fuel cell fundamentals*. John Wiley & Sons New York, 2006.

[202] M. Poppinger and H. Landes. Aspects of the internal reforming of methane in solid oxide fuel cells. *Ionics*, 7(1-2):7–15, 2001.

[203] R. Mahamud, M.M.K. Khan, M.G. Rasul, and M.G. Leinster. Exergy analysis and efficiency improvement of a coal fired thermal power plant in queensland. In *Thermal Power Plants - Advanced Applications*. InTech, apr 2013.

[204] M. Ameri, P. Ahmadi, and S. Khanmohammadi. Exergy analysis of a 420 MW combined cycle power plant. *International Journal of Energy Research*, 32(2):175–183, 2008.

[205] U.S. Department of Energy: Energy Efficiency & Renewable Energy. Comparison of fuel cell technologies. http://www.hydrogenandfuelcells.energy.gov, April 2015.

[206] Made Sucipta, Shinji Kimijima, and Kenjiro Suzuki. Performance analysis of the SOFC–MGT hybrid system with gasified biomass fuel. *Journal of Power Sources*, 174(1):124–135, nov 2007.

[207] Y. Komatsu, S. Kimijima, and J.S. Szmyd. Performance analysis for the part-load operation of a solid oxide fuel cell–micro gas turbine hybrid system. *Energy*, 35(2):982–988, feb 2010.

[208] S.K. Park, K.S. Oh, and T.S. Kim. Analysis of the design of a pressurized SOFC hybrid system using a fixed gas turbine design. *Journal of Power Sources*, 170(1):130–139, jun 2007.

[209] Tae Won Song, Jeong Lak Sohn, Jae Hwan Kim, Tong Seop Kim, Sung Tack Ro, and Kenjiro Suzuki. Performance analysis of a tubular solid oxide fuel cell/micro gas turbine hybrid power system based on a quasi-two dimensional model. *Journal of Power Sources*, 142(1-2):30–42, mar 2005.

[210] Vinod M. Janardhanan, Vincent Heuveline, and Olaf Deutschmann. Performance analysis of a SOFC under direct internal reforming conditions. *Journal of Power Sources*, 172(1):296–307, oct 2007.

[211] Michael M. Whiston, Melissa M. Bilec, and Laura A. Schaefer. SOFC stack model for integration into a hybrid system: Stack response to control variables. *J. Fuel Cell Sci. Technol*, 12(3):031006, mar 2015.

[212] P. Aguiar, C.S. Adjiman, and N.P. Brandon. Anode-supported intermediate temperature direct internal reforming solid oxide fuel cell. I: model-based steady-state performance. *Journal of Power Sources*, 138(1-2):120–136, nov 2004.

[213] Andrea Di Carlo, Enrico Bocci, and Vincenzo Naso. Process simulation of a SOFC and double bubbling fluidized bed gasifier power plant. *International Journal of Hydrogen Energy*, 38(1):532–542, jan 2013.

[214] Suranat Wongchanapai, Hiroshi Iwai, Motohiro Saito, and Hideo Yoshida. Selection of suitable operating conditions for planar anode-supported direct-internal-reforming solid-oxide fuel cell. *Journal of Power Sources*, 204:14–24, apr 2012.

[215] Suranat Wongchanapai, Hiroshi Iwai, Motohiro Saito, and Hideo Yoshida. Performance evaluation of a direct-biogas solid oxide fuel cell-micro gas turbine (SOFC-MGT) hybrid combined heat and power (CHP) system. *Journal of Power Sources*, 223:9–17, feb 2013.

[216] Bariza Zitouni, G.M. Andreadis, Ben Moussa Hocine, Abdenebi Hafsia, Haddad Djamel, and Zeroual Mostefa. Two-dimensional numerical study of temperature field

in an anode supported planar SOFC: Effect of the chemical reaction. *International Journal of Hydrogen Energy*, 36(6):4228–4235, mar 2011.

[217] Thinh X. Ho, Pawel Kosinski, Alex C. Hoffmann, and Arild Vik. Numerical analysis of a planar anode-supported SOFC with composite electrodes. *International Journal of Hydrogen Energy*, 34(8):3488–3499, may 2009.

[218] Zhonggang Zhang, Danting Yue, Guogang Yang, Jingfeng Chen, Yifeng Zheng, He Miao, Weiguo Wang, Jinliang Yuan, and Naibao Huang. Three-dimensional CFD modeling of transport phenomena in multi-channel anode-supported planar SOFCs. *International Journal of Heat and Mass Transfer*, 84:942–954, may 2015.

[219] R. Bove and S. Ulbertini, editors. *Modeling Solid Oxide Fuel Cells: Methods, Procedures and Techniques*. Springer Science+Business Media, 2008.

[220] C. Bang-Møller and M. Rokni. Thermodynamic performance study of biomass gasification, solid oxide fuel cell and micro gas turbine hybrid systems. *Energy Conversion and Management*, 51(11):2330–2339, nov 2010.

[221] Paola Costamagna, Azra Selimovic, Marco Del Borghi, and Gerry Agnew. Electrochemical model of the integrated planar solid oxide fuel cell (IP-SOFC). *Chemical Engineering Journal*, 102(1):61–69, aug 2004.

[222] Energy, Climate Change, and Our Environment | The White House. https://www.whitehouse.gov/energy. Accessed: 2015-08-22.

[223] California Drought Is Made Worse by Global Warming, Scientists Say. http://www.nytimes.com/2015/08/21/science/climate-change-intensifies-california-drought-scientists-say.html?_r=1. Published: 2015-08-20.

[224] The Energy Policy That America Needs - FT.com. http://www.ft.com/cms/s/0/fc195ae8-473c-11e5-af2f-4d6e0e5eda22.html. Accessed: 2015-08-22.